Coherent Nonlinear Phenomena in Subwavelength-Grating Based Microcavities

by
Seonghoon Kim

A dissertation submitted in partial fulfillment
of the requirements for the degree of
Doctor of Philosophy
(Electrical Engineering)
in The University of Michigan
2019

Doctoral Committee:

Associate Professor Hui Deng, Co-Chair
Professor Duncan G. Steel, Co-Chair
Professor Steven T. Cundiff
Professor Mackillo Kira

Seonghoon Kim
shoon@umich.edu
ORCID iD: 0000-0001-9876-6570

ACKNOWLEDGEMENTS

First, I would like to thank my advisor, Professor Hui Deng, for the support and guidance for the last six years. She has given me freedom to grow as an independent researcher and critical advices on the work I've done.

I thank all of the group members for good times in the lab and helpful discussions about research. For the first few years, I thank Bo Zhang and Zhaorong Wang for their help in learning experiments in the lab. Bo also taught me detailed fabrication process on subwavelength gratings in the clean room. I would also like to Lei Zhang for taking mentorship during my first days in clean room. I'm very grateful to Paul and Arina Bierdz for their amazing Thanksgiving dinners and all the help they've given me and my family. I thank other members, Tyler Hill, Glenn Leung, and Adam Katcher. I wish best of luck to remaining postdocs and students in the group, Long Zhang, Jason Horng, Jiaqi Hu, Eunice Paik, and Rahul Gogna.

I would like to thank my committee members, Professors Duncan Steel, Steven Cundiff, and Mackillo Kira for their advice and help.

I also would like to thank collaborators, Professor Sven Höfling for providing the high quality samples and advices on research. I thank Professor Timothy Liew and Yuri Rubo for their helpful discussion on theory of polariton frequency comb.

Lastly, I am grateful to my parents and sister for their support and love. My wife, Jiah Song, is an inspiring person. We have supported each other through good and bad times for all our life. There's no word to describe how much I love my daughter, Leah. I can't wait for a new chapter in my life with my family.

TABLE OF CONTENTS

ACKNOWLEDGEMENTS ii

LIST OF FIGURES v

ABSTRACT xiii

CHAPTER

I. Introduction 1

II. Subwavelength High-Contrast Grating based Microcavity . . 6

2.1 Air-suspended HCG-based microcavities 7
2.1.1 RCWA Simulation of HCG Microcavities 8
2.1.2 Fabrication Process of HCG Microcavities 10
2.1.3 Optical Characterization of HCG Microcavities . . . 15
2.2 Monolithic HCG-based microcavities 16
2.2.1 RCWA Simulation of MHCG Microcavities 18
2.2.2 Fabrication Process of MHCG Microcavities 20
2.2.3 Optical Characterization of MHCG Microcavities . . 23

III. Coherent Polariton Lasing 29

3.1 Theory of Quantum Coherence 30
3.2 Optical coherence of 0D microcavity 32
3.2.1 Experimental Details and Setup 33
3.2.2 Single-mode Polariton Lasing 34
3.2.3 Multi-mode Polariton Lasing 45
3.3 Optimizing Coherence of Polariton Laser 47

IV. Optical Frequency Comb Generation in Coupled Microcavities 56

4.1 Driven-Dissipative Coupled Polariton Equation 57

4.2 Realization of two-coupled condensates in HCG microcavities 59
4.2.1 Experimental Measurements of HCG Bending . . . 60
4.2.2 HCG Bending Simulation 64
4.2.3 Realization of two-coupled HCG microcavities . . . 66
4.3 Excitation power-dependent spectrum 66
4.4 Beating measurement of multi-frequency components 69
4.5 Nontrivial phase coupling between two sites 72
4.6 Conclusion 76

V. SWG-Microcavity Optomechanics 77

5.1 Mechanical mode of HCG mirrors 78
5.2 Experimental observation of polariton optomechanics 78

VI. Orbital Angular Momentum and Vector Beam Generation . 83

6.1 Detection of quantized vortices in polariton condensates . . . 84
6.2 Experimental observation of quantized vortices 85
6.3 OAM-carrying radially polarized vector beam generation . . . 87

VII. Conclusions and Outlook 93

BIBLIOGRAPHY 95

LIST OF FIGURES

Figure

2.1 Schematic of air-suspended HCG. period Λ is grating peiriod, η is duty cycle, d is thickness and n_l is refractive index of the grating layer. TE and TM denotes the direction of polarization of incident light. 8

2.2 RCWA simulation of HCG. (a) is reflectance map of $d - \lambda$ parameter space. (b) is the reflectance spectrum at $d = 90\ nm$ from (a). 9

2.3 Schematic of HCG microcavity and simulated reflectance of the cavity. (a) Schematic view of HCG microcavity. (b) Simulated reflectance spectrum of the wafer before HCG fabrication. (c), (d) Simulated reflectance spectrum of the fabricated cavity in TE and TM, respectively. 11

2.4 HCG fabrication flow. 12

2.5 Proximity effect correction. (a) Three device examples of electron dose distribution after PEC. (b), (c) SEM top view of the fabricated device without PEC and with PEC, respectively. 13

2.6 SEM side view and top view of HCG. (a) SEM side view of the fabricated HCG. The grating layer is approximately 80 nm and the sacrificial layer of about 600 nm is completely etched. (b) SEM top view of the HCG. 14

2.7 K-space spectrum (a) in TE and (b) TM polarizations. TE polarization shows discrete LP states while TM polarization shows uncoupled exciton states. 16

2.8 Power dependent spectrum, integrated intensity, linewidth, and blueshift of the polariton ground state. Spectrum (a) below, (b) at, (c) above the lasing threshold. (d) Integrated intensity, (e) linewdith, and (f) energy blueshift of the ground state as a function of pump power. . 17

2.9 Schematic of monolithic HCG. period Λ is grating peiriod, η is duty cycle, d is thickness and n_l is refractive index of the grating layer, and n_2 is refractive index of the second layer. TE and TM denotes the direction of polarization of incident light. Red arrows indicate high-order diffraction orders that may be possible when refractive index difference between n_l and n_2 is small. 18

2.10 RCWA simulation of MHCG. (a) is reflectance map of $d-\lambda$ parameter space. (b) is the reflectance spectrum at $d = 200\ nm$ from (a). . . . 19

2.11 Schematic of MHCG microcavity and simulated reflectance of the cavity. (a) Schematic view of MHCG microcavity. (b) Simulated reflectance spectrum of the wafer before MHCG fabrication. (c), (d) Simulated reflectance spectrum of the fabricated cavity in TE and TM, respectively. 20

2.12 MHCG microcavity resonance tuning. (a) Spectrum near resonance for (a) three different periods and (b) three different duty cycle. . . 21

2.13 MHCG fabrication flow 22

2.14 Selective dry etching development. (a) SEM side view after selective dry etching. The etching profile is slanted because of the passivation effect. (b) SEM side view after nonselective etching followed by selective etching. The results show vertical side wall profile and clean etched surface. 24

2.15 K-space spectrum (a) in TM and (b) TE polarizations. TM polarization shows dispersion of LP states while TE polarization shows uncoupled exciton states. 25

2.16 Power dependent spectrum, integrated intensity, linewidth, and blueshift of the polariton ground state. Spectrum (a) below, (b) at, (c) above the lasing threshold. (d) Integrated intensity, (e) linewdith, and (f) energy blueshift of the ground state as a function of pump power. . 26

2.17 Tuning of the emission wavelength by the grating period. (a) Measured LP and UP resonances (open diamonds and squares, respectively) at low pump powers and the corresponding cavity resonances as a function of the grating period. The cavity resonances obtained from the measured LP, UP, and exciton resonances are marked by the open circles, while the cavity resonances calculated by the RCWA are marked by the red crosses. The solid line is a linear fit to the experimental cavity resonance vs period, showing tuning of the cavity resonance with the grating period at 1 nm/10.12 nm. (b) Emission spectrum at low pump powers as the grating period of the MHCG is varied from 328 to 344 nm with 4 nm increment. The LP resonance shifts toward longer wavelengths as the period increases. The exciton resonance remains the same in all the spectra. (c) Emission spectra of the lasing state at high pump powers for the corresponding MHCGs as in (b). 28

3.1 Schematic of the experimental setup. OL: Objective lens, BS: Beam splitter, P: Polarizer, M: Mirror, MC: Monochromator, and APD: Avalanche photodetector. For the $g^{(2)}$ measurements, a monochromator followed by two mechanical slits was used to spectrally filter the discrete polariton states. Examples are shown for the spectrally-resolved real space images of the lowest two LP states right after the monochromator (bottom), the spectrally filtered ground state (top left) and the spectrally filtered first excited state (top right). The resolution of the spectral filter was about 0.08 nm, determined by the monochrometer resolution. 34

3.2 Pump position for single-mode lasing. (a) Pump spot is focused at the center of the device. (b) Spectrum above the lasing threshold. . 35

3.3 Intensity and spectral properties of the single-mode polariton laser. (a) The occupation number vs. P/P_{th} for pulsed excitation. P_{th} indicates the threshold for polariton lasing and $P_{th,2}$ indicates the threshold for photon lasing. $\bar{n}$ is estimated from the independently measured PL intensity from the ground state, collection and detection efficiencies of the setup, and the polariton lifetime [1, 2]. (b) Energy and blueshift of the polariton ground state (dots) and lasing photon mode (squares) vs. the normalized pump powers P/P_{th} for pulsed excitation. Here P_{th} is the pump power at the polariton lasing threshold. The solid vertical line marks the polariton lasing threshold and the dashed vertical line marks the photon lasing threshold. (c) The linewidth (full-width at half-maximum) of the polariton ground state vs. P/P_{th} for pulsed excitation. (d), (e), (f) The occupation number, blueshift, and linewidth of the polariton ground state vs. P/P_{th} for CW excitation. The dashed line in (F) represents the spectral resolution of the monochromator of about 0.08 nm. 36

3.4 (a) The pulse duration of the ground state polariton emission ΔT vs. the normalized pump power P/P_{th}. ΔT are obtained by fitting $g^{(2)}(\tau)$ measured for two uncorrelated pulses, taking into account the measured IRFs of the photon counters. ΔT was well fitted at $P/P_{th} < 1.5$ (dots) and unresolvable at $P/P_{th} > 1.5$ (circles). The solid line is the intensity correlation time of 3.1 ps estimated from $g^{(2)}(0)$ below the threshold. (b), (c) Two examples of the least square fitting of $g^{(2)}(\tau)$ vs. τ of two uncorrelated pulses, at $P/P_{th} = 0.67$ and 1, respectively. The dots are data; the solid lines are the fits using the measured IRF; the dashed lines are the convolution of two IRFs of the photon counter. 37

3.5 Second-order coherence properties of the single-mode polariton laser. (a) $\overline{g^{(2)}}(\tau)$ vs. τ below and above the threshold for pulsed excitation. (b) $\overline{g^{(2)}}(\tau)$ vs. τ below and above the threshold for CW excitation. (c) $\overline{g^{(2)}}(0)$ vs. P/P_{th} for pulsed (dots) and CW (rectangles) excitations. The error bars indicate statistical error of one standard deviation. The grey-shaded area shows where the polariton and photon lasing coexist. Inset: $g^{(2)}(0)$ vs. $\bar{n}$ of pulsed excitation corrected for the relaxation time of the ground state. The solid line shows a theoretical fit by Eq. (3.8), yielding $n_s = 37.3 \pm 0.9$. 40

3.6 First-order coherence properties of the single-mode polariton laser. (a) A spatial interference image of the polariton laser at zero time delay. (b) The interference fringe along x-axis obtained from (a) by integration along the y-axis. The dots are data and the solid line is a fit by equation (3.11) with $g^{(1)}(0) = 0.94$. (c), (d) The measured $g^{(1)}(\tau)$ vs. τ (dots), exponential fits (red solid lines), and Gaussian fits (black dashed lines), for $\bar{n} = 2.66$ and 968, respectively. (e) The phase coherence time τ_c of the polariton laser vs. $\bar{n}$. The dots are taken from the measured $g^{(1)}(\tau)$ for each value of $\bar{n}$. The line is calculated from Eq. (3.12) using the fitted parameters. Inset: Comparison between the interaction energy U (dots) and decay rate γ (yellow shaded region) of the condensate vs. $\bar{n}$. The error bars and thickness of the shaded area are determined by fitting errors with a 95% confidence interval. The rectangle and diamond marks respresent $\bar{n} = 2.66$ and $\bar{n} = 968$, respectively. 50

3.7 Pump position for multi-mode lasing. (a) Pump spot is focused at the side of the device. (b) Spectrum above the lasing threshold. . . 51

3.8 Second-order correlations of the two-mode polariton laser. (a) The occupation numbers of the ground state (dots) the excited state (squares) vs. P/P_{th}. GS: Ground state, ES: First excited state. (b) $\overline{g^{(2)}}(0)$ vs. P/P_{th}. $\overline{g_{00}^{(2)}}(0)$: auto-correlation of GS, $\overline{g_{11}^{(2)}}(0)$: auto-correlation of ES, and $\overline{g_{01}^{(2)}}(0)$: cross-correlation between GS and ES. 52

3.9 Numerical simulation of second-order correlations of the two-mode polariton laser. Dashed line is simulated second-order correlation of the single-mode laser which shows much faster decrease of $g^{(2)}(0)$. . 53

3.10 SEM top view of fabricated devices with different size 53

3.11 PL spectrum of fabricated devices near the lasing threshold. (a), (d) 6 μm. (b), (e) 10 μm. (c), (f) 40 μm 54

3.12 Size dependent coherence time and $g^{(2)}(0)$. (a) Measured maximum coherence time for different size of devices. (b) Measured $g^{(2)}(0)$ for different size of devices. The value for each device is taken at the highest laser intensity. 55

4.1 Two-coupled polariton condensates. (a) Two condensates with the same energy (ω) and decay rate (γ) coupled through coherent (J) and dissipative couplings (Γ). (b) Coupled states with energies splitted by coherent coupling strength and decay rates of $\Gamma - \gamma/2$ and $\Gamma + \gamma/2$. 57

4.2 Bifurcation diagram for coupled polariton equation. (a), (b) Bifurcation diagram in $P - \gamma$ parameter space for $J/\Gamma = 0.07$, 2.5, respectively. Other parameters are $\alpha/\Gamma = 0.25$, $\mu/\Gamma = 0.05$ for both diagrams. A standard lasing threshold is when $P = \Gamma$ in the absence of dissipative coupling. For certain values of $\gamma > 0$, thresholds for stable and unstable fixed-point solutions emerge as P increases, indicated by arrows for $\gamma/\Gamma = 0.1$. 58

4.3 AFM images of square HCG. (a), (b) Side views of AFM images of the HCG showing upward bends of the suspended structure. (c) Top view of the HCG bending image. Line cut indicates that a grating bar bends more than 100 nm. 61

4.4 Discontinuity of LCSM measurements for sub-wavelength gratings. . 62

4.5 LCSM measurement results. (a) Test grating designs. (b) Test designs and results for the grating with and without strain release patterns on both sides. (c) Test design and result for the grating with strain release pattern on one side. (d) Bending measurements for one dimensional grating structure. 63

4.6 Drawing of HCG devices by AutoCAD. (a) Gratings with a single-side release pattern. (b) Square grating. (c) Two-coupled grating. . 64

4.7 Comparison between COMSOL simulation and LCSM measurements. (a), (b) Simulated and measured results for single-side release pattern. (c), (d) Simulated and measured results for square grating structure. 65

4.8 Sample properties at low excitation powers. (a) A schematic of the sample structure with a bent SWG mirror. Bending of the SWG is simulated by COMSOL and shown both by the color map in the schematic view and in the side view. The bending is less where there are open slots in the tethering pattern and vice versa. (b) The real-space photoluminescence (PL) spectrum of the coupled polariton system showing the discrete polariton states at low excitation powers. The ground state is formed by the bonding state (B state), while the first excited state is the anti-bonding state (A state). The white dashed line illustrates the potential due to the bending of the SWG shown in (a). (c) The corresponding Fourier space spectrum showing the B state at $k = 0$ and the A state at $k = \pm\pi/a$, where a is the distance between the two coupled sites. 67

4.9 Excitation power dependence of the intensity and real-space spectra of the polariton PL near the A and B states. (a) Bottom: Mean polariton number of the A and B states vs. the excitation power for the L site (blue square), R site (red circle) and the sum of the L and R sites (black diamond). It shows clearly a threshold behavior and degenerate occupation at each site. Top: Relative fraction of the B state (blue plus) and A state (red cross) population vs. the excitation power, showing switching of the dominant state upon transitions to the A-state weak lasing and stable B-state lasing. (b)-(e), The real-space spectra at four different excitation powers, showing the transition from A state weak lasing, to limited cycles, toward B state lasing. The white dashed line marks the E state – the lowest energy state after B and A states. f-i, Spectrum of each site obtained from b-e respectively. The solid lines are fits by equidistant Lorentzians. More than two frequency components are apparent in (c), (d), (g) & (h). 70

4.10 Excitation power dependent K-space spectrum. Power increases from (a) to (g). Three powers used in real-space spectra correspond to (e)-(g). White dashed line indicates $k = 0$. B and A state shift in K-space whereas the first exited states remain symmetric around $k = 0$ from a-d. 71

4.11 Experimental (a)-(c) and theoretical (d)-(f) $g^{(1)}(\tau)$ for three different excitation powers, corresponding to Fig. 4.9(c)-(e), respectively. Red dots are shifted vertically by 0.1 for better visibility. The inset shows a zoom in of the beating peaks in a (The lines are guides to the eye). The site with more frequency lines has more beating peaks and narrower $g^{(1)}(\tau)$ linewidths at t=0. The simulated $g^{(1)}(\tau)$ is multiplied by an exponential decay with decay times of 20, 25, 30 ps respectively. 73

4.12 Magnified Mach-Zehnder interferometer. Magnified image provides phase reference for relative phase measurements between two sites. . 74

4.13 Relative phase measurement between L and R sites at excitation powers of 2 mW (a,d), 2.3 mW (b,e) and 2.5 mW (c,f). a-c, Interference images from interfering both sites to a magnified single site. d-f, Interference fringes for each site obtained from a-c along $x = \pm 3\ \mu m$ (dots). The solid lines are fits as described in Methods. From the fit, we obtain the relative phase difference of 0.51 π, 0.21 π, and 0.15 π respectively. 75

5.1 Simulated mechanical modes of HCG. (a) A drawing of HCG membrane. (b) Simulated fundamental mechanical mode of 2.8 MHz. . . 78

5.2 (a) Discrete spectral peaks above the mirror oscillation threshold. (b) Simple harmonic motion of the HCG mirror with a growing amplitude. 79

5.3 Time-domain measurements. (a) Time-resolved intensity showing a periodic oscillation at 2.86 MHz. (b) Spectrum- and time-resolved measurements. Different spectral components appear at different time. (c) Pulsing with much shorter width than the mechanical oscillation. (d) Relative amplitude of pulsing compared to other oscillating intensities with different spectral components. 81

5.4 Simulation results. Below lasing threshold (a) without mirror oscillations and (b) with mirror oscillations. Above lasing threshold (c) without mirror oscillations and (d) with mirror oscillations 82

6.1 Simulated fork patterns from interfering OAM with flat phase reference with a finite angle. (a) 2π phase winding, $l = 1$ (b) 4π phase winding, $l = 2$. 84

6.2 Fourier transform-based phase extraction technique. (a) Raw interference data. (b) Fourier transform image. Two side peaks are due to fringe pattern. (c) Filtering one of two side peaks. (d) Phase map after inverse Fourier transform of (c) showing a vortex-antivortex pair. 86

6.3 SEM images of single defect devices. (a) Rectangular devices with different shape and size of defects. (b) Circular device with circular defect. (c) Device without circular symmetry. (d) Photonic benzene. 87

6.4 Retrieved phase of single-defect devices. (a), (d), (e) Device structures. (b), (e), (h) phase maps of (a), (d), (e). (c), (f), (i) interference fringe of (a), (d), (e). 88

6.5 SEM images of multiple defect devices. (a) Devices with two defects. (b) Three defects. (c) Four defects. 89

6.6 Retrieved phase of multiple defect devices. (a), (d), (e) Device structures. (b), (e), (h) phase maps of (a), (d), (e). 90

6.7 SEM image of circular gratings for a vector beam device. 91

6.8 Experimental results of a vector beam generation. (a) Polarization dependent spatial emission pattern. (b) OAM detection (c), (d) r- and k-space spectrum of the polariton laser 92

ABSTRACT

Bose-Einstein condensation of microcavity polaritons has shown remarkable phenomena such as coherent lasing below population inversion, quantized vortices, and Josephson effects in a semiconductor platform. With nonlinear interaction between exciton-polaritons, it has also drawn great interests for nonlinear photonic devices. To control nonlinear interaction strength, many efforts to confine polariton condensates have been made. In this work, we use a subwavelength-grating (SWG) mirror to confine exciton-polaritons in a lithographically defined area. Being a one-dimensional photonic crystal, it is possible to control emission polarization depending on the grating parameters. Moreover, SWG mirrors require only two layers which reduce the fabrication complexity compared to distributed Bragg reflectors (DBRs). In this thesis, we present two approaches to realize exciton-polariton systems with SWG. One is air-suspended and the other is fully monolithic.

With SWG-DBR microcavities, we first achieve single-mode lasing in both energy and polarization. In a conventional DBR-DBR microcavity where single-mode lasing in both energy and polarization is nearly impossible, excess intensity fluctuations from polariton lasers were observed. The SWG microcavity removes any mode-competition which has adverse effects on intensity coherence and in turn phase coherence. As a result, we show shot-noise limited intensity fluctuations and phase coherence that is well explained by atom laser theory with two-body interactions. Further optimization of the phase coherence is shown by varying device sizes with different interaction strengths.

We then realize coupling between single-mode condensates by spatial control of

exciton-photon detuning. New frequency comb mechanism was recently proposed from two coupled polariton condensates with complex couplings. We experimentally observe multifrequency components, which are generated from limit-cycle oscillations. Numerical simulation of the coupled polariton equation shows good agreement with the experimental results. This polariton comb allows non-resonant excitation with a power input below the conventional semiconductor laser. The comb line spacing, determined by the interaction and coupling strengths, is adjustable up to multi-terahertz frequency for a chip-scale low power terahertz source.

We also investigate polariton optomechanics for potential q-switched polariton lasers. Since the SWG is a thin single slab that is suspended in the air, it is a good candidate for optomechanics as shown in VCSEL. Unique to polariton system, the mechanical motion of the mirror not only changes resonance frequency but also the dissipation rate, important to realize q-switching. Here, we show bright emission of short pulses, which resembles q-switched lasers, when the mirror oscillates.

Finally, we present the orbital angular momentum (OAM) and vector beam generation in SWG-based microcavities. The OAM and polarization states provide additional degrees of freedom for information transmission. Direct generation of the OAM source from micro or nanostructure has been desired but challenging. In polariton systems, a potential for the OAM laser has been shown as the quantized vortices have been observed around naturally occurring defects on the sample. The remaining challenge was to create deterministic defects that form vortices or OAM. For SWG microcavities, it is very easy to create defects because we can remove the entire top mirror by etching only a single layer. We created many different defects and show formations of quantized vortices. By breaking the symmetry of the defects, we create polariton lasers which possess nonzero OAM. Using polarization selectivity, we also create circular gratings which have radially polarized emission.

CHAPTER I

Introduction

When a dilute Bose gas is sufficiently cooled down, it shows a striking phenomenon called Bose-Einstein condensation (BEC) where a gas forms a macroscopic ground state. BEC was first observed in Rubidium gas at 170 nK [3] and Sodium gas at 2 μK [4]. Many efforts have been focused toward understanding fundamental physics of this new phenomenon such as interference between condensates [5], quantized vortices [6, 7, 8], Josephson physics [9, 10], and soliton physics [11] to name a few. Importantly, controllable interaction between atoms through Feshbach resonances [12, 13] leads to another research area regarding atom-lattice systems and Bose-Hubbard physics [14, 15]. Another possibility for this new exciting physics exists in solid-state systems. Combining with mature semiconductor fabrication technique, this opportunity has a great potential not only for fundamental physics research but also for practical device applications. There are many quasiparticles in solid which are bosons such as excitons and exciton-polaritons. Excitons have shown some evidences toward BEC [16, 17] with indirect excitons and possible device applications [18]. However, to cool down excitons enough, the temperature needs to be less than liquid Helium and there is less room to improve, where the critical temperature is determined by excitons' mass.

Exciton-polaritons, however, are quasiparticles that are half-exciton (half-matter), half-light [19, 20]. Through their light components, the critical temperature can in-

crease up to room temperature in wide band-gap GaN [21] and organic materials [22], making it a great candidate for practical device applications using properties of BEC. The structure to achieve strong exciton-photon coupling is a microcavity on resonance with the quantum well (QW) excitons embedded inside a cavity layer [23]. The normal-mode splitting is observable when the exciton-photon exchange interaction strength, or the Rabi frequency, is faster than the decay rate of excitons and cavity photons. The dominant decay channel in this system is normally the cavity decay rate. In recent years, the advancement of growth process allows the cavity decay rate to approach closer to the exciton decay rate [24]. Also, one can increase the Rabi frequency by increasing the number of QWs and cavity's quality factor or mode volume. The increase of decay rate is also important for realizing exciton-polariton BEC since the decay time should be long enough to allow polariton population to accumulate in the ground state of the polariton modes. The first evidence of polariton BEC was reported in 2002 by measuring the spontaneous coherence and macroscopic occupation [25]. Later, further studies on long-range order parameter and distribution function confirmed the existence of this macroscopic coherent state formed in semiconductor microcavities [26, 27]. The question of the polariton BEC naturally arises due to the driven-dissipative nature of the system. To maintain BEC, the system requires constant pumping of the exciton reservoir because the polariton leaks through the cavity mirrors. Despite the driven-dissipative nature, many features observed from atomic BECs has also been reproduced in the polariton system such as superfluidity [28, 29], quantized vortices [30, 31], Josephson oscillations [32, 33], soliton physics [34]. Similar efforts to control polaritonic interaction strength through Feshbach resonances was also attempted with limited success [35]. However, more successful approach to control its interaction strength has been reported through confinement of a polariton gas by means of photonic modes [36, 37, 38]. Confinement of a polariton condensate through semiconductor nanofabrication and optically induced potential also opens a

door to realize polaritonic lattices [39, 40], topological physics [41, 42], and quantum simulators [43].

I'd like to discuss some of the most successful methods for making confined and coupled polariton systems and explain advantages and differences between our approach utilizing subwavelength grating and other methods. One method is to use pump-induced potentials [44, 45, 46]. Polaritons are repulsive and therefore the energy of the polariton modes blueshifts when the population increases and the polaritons tend to flow away from the pump spot where the exciton density is high. To create lattice with controllable parameters, pump configuration can be chosen using spatial light modulators or digital micromirror devices. Although it is very flexible and easy to manipulate, this method has an inherent limitation that is gain, height of the potential, coupling strength between lattice sites are not easily separable since they all rely on a pump laser. For example, it will be very difficult to pump the potential minima of lattice sites without significantly changing the potential landscape. Also increasing or decreasing pump strength changes many of the lattice parameters (as listed above) at the same time and difficult to systematically study the effect of a single lattice parameter. It is possible to make a system with predetermined potential by engineering either exciton modes or photon modes. The most successful method is to deep etch microcavities, therefore trap polaritons in given etched area [2]. Coupling strengths between adjacent sites can be adjusted by narrowing a tunneling path between sites [47, 33]. Although this method is very robust and current state-of-the-art, it is difficult to control intrinsic photonic properties of the microcavities such as emission polarization and dispersion. Subwavelength high-contrast grating (HCG), on the other hand, is a designable mirror. High reflectance of the HCG mirror has been proven in vertical cavity surface emitting lasers (VCSELs) [48, 49, 50] which the structure is almost identical to the polariton microcavities. The first polariton laser based on HCG microcavities was realized in 2014 [51]. The emission polarization and

dispersion of the cavity modes is controllable by grating parameters [50, 52]. Moreover, the epitaxial structure is easier to grow compared to the conventional distributed Bragg reflector (DBR) based microcavities since the HCG mirror only requires one or two layers in stark contrast with tens of layers for DBRs. This dissertation focus on the series of steady developments toward making flexible polariton systems incorporating HCG mirrors.

First, I'll discuss details of sample design, HCG simulation, HCG fabrication, and optical properties of HCG microcavities. I'll present two different approaches to realize HCG, one is air-suspended HCG and the other is fully monolithic HCG. Air-suspended HCGs are used for most VCSEL and polariton applications as they show high reflectance both theoretically and experimentally. Also, there's opportunity to use its mechanical properties as the mass of the HCG mirror is very light [53, 54]. However, the major drawback is that the fabrication process to undercut the sacrificial layer is rather complex and delicate, thus making large devices for polariton lattaces are nearly impossible. A fully monolithic HCG offers a nice solution to these issues. Since it is fully monolithic, fabrication process is very simple and robust. One critical issue in the sample presented in this thesis is that the sample is not optimized for the monolithic HCG and the quality factor is just enough to show polariton lasing.

Second, I'll present the fully coherent polariton lasing from a single-mode polariton state unique to HCG microcavities. Through polarization selectivity of the HCG mirror, we realize a single-mode both in energy and polarization. This study solves issues with previous coherence studies on polariton condensation as to why it shows poor coherence properties and paves the way to optimize coherent properties of polariton laser for practical low threshold coherent light sources. We also observed the signature of interacting polaritons through phase coherence very different from photon lasers where Schawlow-Townes linewidth is expected. To this end, I'll present the effort to optimize coherence of polariton lasers by engineering polariton-polariton

interaction strength.

Using a coherent single-mode condensate, we investigate a way to couple condensate sites and realize coupled polariton [55]. Individual sites and coupling strength are made by spatial detuning change taking advantage of the bending of HCGs. Coupled condensates have shown interesting physics such as Josephson oscillations [33] and periodic squeezing [56]. Recently, frequency comb generations from limit-cycle oscillations in coupled condensates are theoretically investigated [57]. We experimentally observed appearance of multi-frequency components from coupled condensates due to the existence of on-site interaction and complex coupling coefficients. I'll present experimental and theoretical analysis of this new type of frequency comb sources.

In the last part, I'll present experimental evidence for polariton optomechanics as well as orbital angular momentum (OAM) and vector beam generation. For optomechanics, we observed intensity oscillation which the frequency is well matched to the simulated mechanical mode of the HCG mirror. We also observed short pulse emission, much shorter than period of mechanical mode. This pulse shows high peak intensity which could have similar origin to Q-switching and could be useful since the polariton lasing is quite weak since it only happens below Mott density. OAM polariton laser is realized through defect engineering on monolithic HCG mirrors. It is well known that quantized vortices can be formed around defects on microcavities [30, 58]. With HCG mirrors, it is easy to implant defects and form vortices around those defects. Finally, a vector beam having spatially dependent polarization state is realized by making circular grating structures.

CHAPTER II

Subwavelength High-Contrast Grating based Microcavity

Vertical microcavity lasers consist of a vertical cavity formed by two highly reflective mirrors and a gain medium inside the cavity structure. The most well known and used method is distributed Bragg reflectors (DBRs), which is made of alternating layers of high and low refractive indices with $\lambda/4$ optical path length. The optical path length results in constructive interference between reflected light and destructive interference between transmitted light. Theoretically, by stacking a number of layers, it is possible to make DBRs with almost 100 % reflectivity. In reality, however, it is very challenging to grow multiple layers of different refractive indices without any structural defects, which requires very careful and slow growth process through molecular beam epitaxy.

High-contrast gratings (HCGs) are recent addition to the methods of realizing highly reflective mirrors. Remarkably, this method only requires a single layer or two layers to achieve near perfect reflectivity [59, 60]. The main challenge was that HCGs have to be subwavelength. This means the grating parameters such as period and thickness need to be less than the wavelength of a target wavelength we want to achieve high reflectance for, typically in a few nanometers range. Recent advances in semiconductor nanofabrication process now enable us to fabricate these

subwavelength structure in a very robust way. The first demonstration of this new type of mirror incorporated in vertical cavity surface emitting lasers (VCSELs) was published in 2007 [48]. Now, HCGs are successfully employed in strongly coupled exciton polaritons [51].

In this chapter, I will discuss two main approaches that are used to create high-reflectance HCGs for exciton-polariton microcavities. The first one is air-suspended gratings, used in almost all of vertical cavity applications since the invention in 2007. The other approach is fully monolithic HCGs (MHCGs), often called zero-contrast gratings, which was theoretically proposed but never realized in vertical cavity lasers.

2.1 Air-suspended HCG-based microcavities

In this section, I will discuss optical properties of microcavities incorporating air-suspended HCGs by Rigorous coupled wave analysis (RCWA) simulation and experimental measurements. I'll refer air-suspended HCGs to HCGs as they are more commonly used. Figure 2.1 shows the schematic view of the HCGs. There are mainly four grating parameters: period (Λ), duty cycle (η), thickness (d) and refractive index (n_l) of the grating layer. General steps to realize HCGs are following. First, we need to determine materials which in turn determine refractive index of the grating layer. The materials for the grating and the sacrificial layer should be chosen so that the etching selectivity between two layers is large enough to make air-suspended structure. Then, we can fix one parameter, for example a duty cycle of 0.5, and sweep a two-dimensional parameter space ($d/\Lambda, \lambda/\Lambda$) to find wide parameter region that supports high reflectance, where λ is the wavelength of an incident light. This three-dimensional reflectance map gives insight on how thick the grating layer should be. Once the material and thickness are set, wafer for this HCG can be grown. For cavity applications, the thickness for the sacrificial layer should be determined to ensure the cavity round trip of 2π at the target resonance wavelength of the cavity.

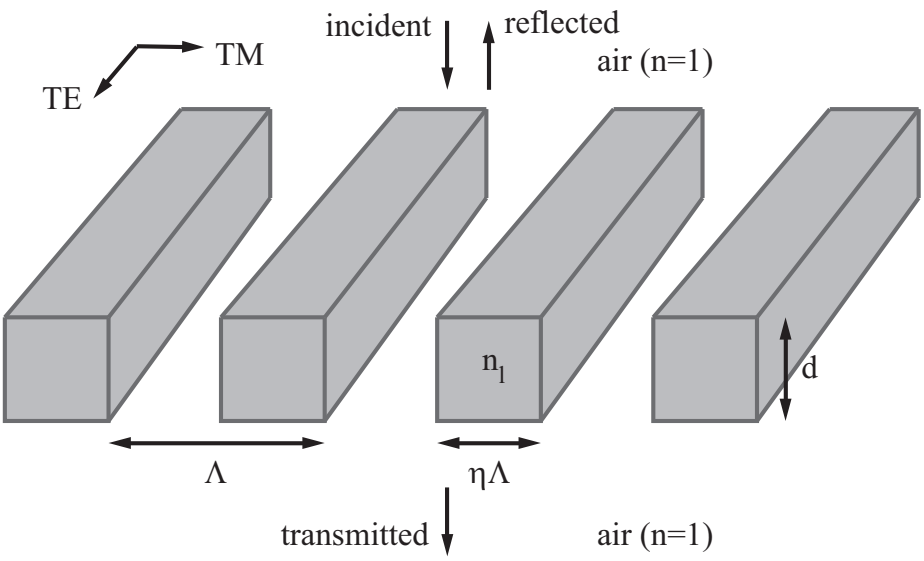

Figure 2.1: Schematic of air-suspended HCG. period Λ is grating peiriod, η is duty cycle, d is thickness and n_l is refractive index of the grating layer. TE and TM denotes the direction of polarization of incident light.

2.1.1 RCWA Simulation of HCG Microcavities

Different from DBRs, HCGs are one-dimensional photonic crystal, which have design parameters to control properties such as polarization and energy-momentum dispersion relation [52], though it is desirable to replace both DBRs with HCGs for dispersion engineering. Here, we realized HCGs that work only in transverse-electric (TE) polarization and not in transverse-magnetic (TM) polarization. The directions of two polarizations are denoted in Fig. 2.1. The simulated reflectance for TE-polarized light in $d/\Lambda - \lambda/\Lambda$ parameter space is shown in Fig. 2.2(a) for $n_l = 3.58$ ($Al_{0.15}Ga_{0.85}As$). Figure 2.2(b) shows an example of broadband high-reflectance of the HCG mirror with parameters for $\Gamma = 500\ nm$, $d = 90\ nm$, and $\eta = 0.4$. These values are very close to actual device parameters and show high reflectance centered around the target wavelength of about 800 nm.

The working principle of HCG can be explained by the two-mode canceling theory [50]. In the near sub-wavelength regime, the field in the grating layer can be decomposed into two waveguide-array (WGA) modes, the 0th and 2nd order modes for

normal incidence, as odd modes are forbidden by symmetry and higher-order modes are cut off. We write $\mathcal{E}_m(x)$, the lateral profile of the WGA mode as:

$$E(x,z) = \sum_{m=0,2} \mathcal{E}_m(x)[a_m e^{-j\beta_m(z-t_g)} + b_m e^{+j\beta_m(z-t_g)}]. \tag{2.1}$$

Here the exponential parts represent the forward and backward propagations in the z-direction with coefficients of a_m and b_m, respectively. β_m is the propagation constant for mth mode and t_g is the thickness of grating. The two modes are mutually orthogonal in the grating layer, but can couple at the grating boundaries, $\boldsymbol{b} = \boldsymbol{Ra}$, where $\boldsymbol{R}$ is a 2×2 reflection matrix. It has large off-diagonal elements due to the abrupt change of refractive index profile at the grating-air boundary. The coupling of the two modes helps equalize their amplitudes. The relative phase between the two modes can be controlled precisely by tuning the thickness of grating. Hence destructive interfere between the two modes can be achieved at the output plane where the zeroth order diffraction mode is coupled out of the grating, leading to zero transmission and therefore 100% reflection.

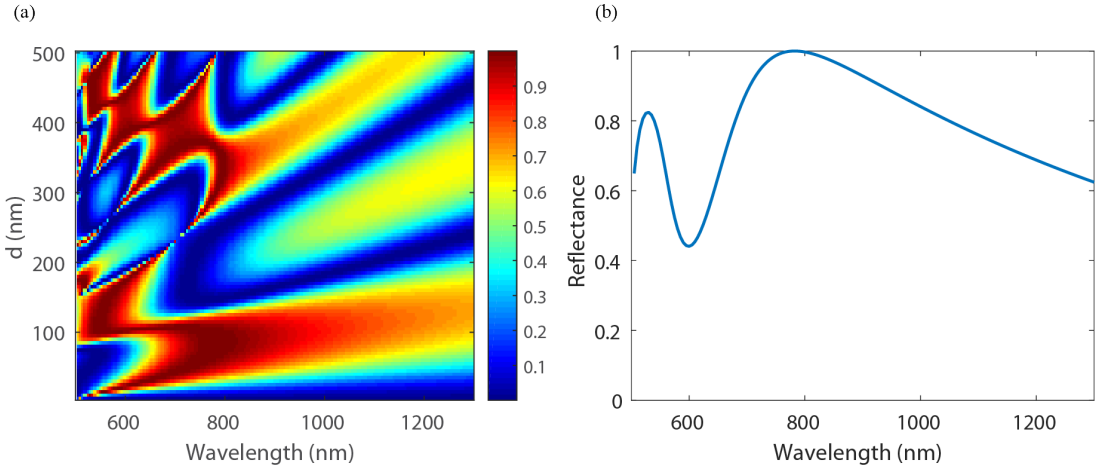

Figure 2.2: RCWA simulation of HCG. (a) is reflectance map of $d - \lambda$ parameter space. (b) is the reflectance spectrum at $d = 90\ nm$ from (a).

The entire microcavity structure is shown in Fig. 2.3(a). The wafer is epitaxially

grown on GaAs substrate with 30 pairs of bottom DBRs, 12 GaAs quantum wells in an AlAs $\lambda/2$ cavity layer, 2.5 pairs of top DBRs, an $Al_{0.85}Ga_{0.15}As$ sacrificial layer, and an $Al_{0.15}Ga_{0.85}As$ grating layer. The grating layer is chosen to be about 80 nm thick for high-reflectance and the sacrificial layer (to be an air gap after undercut through selective wet etching process) is about 500 nm thick for cavity resonance wavelength at around 800 nm. Note that the 2.5 pairs of top DBRs are not necessary for high-reflectance but rather acting as protection layers for the cavity layer from wet etching process. To confirm whether the layer thicknesses of the epitaxial sample is consistent with the design values, we measured reflectance spectrum of the wafer at room temperature. Comparing the measurement with the transfer-matrix simulation (Fig. 2.3(b), actual thicknesses of layers can be accurately identified. This is an important step as the layer thicknesses play an important role in cavity resonance wavelength. The simulated reflectance of the microcavity, without considering absorption of quantum wells, clearly shows high quality factor shown by a narrow cavity dip around the target wavelength (Fig. 2.3(c) with the HCG parameters used in Fig. 2.2(b)). However, TM-polarized light does not show any significant cavity dip (Fig. 2.3(d)) since the HCG is designed to work in TE polarization. For this specific HCG, the cavity resonance is sensitive to the thickness of the first two layers (grating and sacrificial/air gap) and less to the period and duty cycle.

2.1.2 Fabrication Process of HCG Microcavities

The fabrication process involves electron beam lithography (EBL), plasma etching, wet etching, and critical point drying. The schematic flow is shown in Fig. 2.4. Details on each process will be discussed in the following.

For EBL process, we used ZEP520a from ZEON as a e-beam resist mainly because it has very good dry etch resistance compared to widely used PMMA. One another important consideration in EBL is proximity effect. The proximity effect is caused by

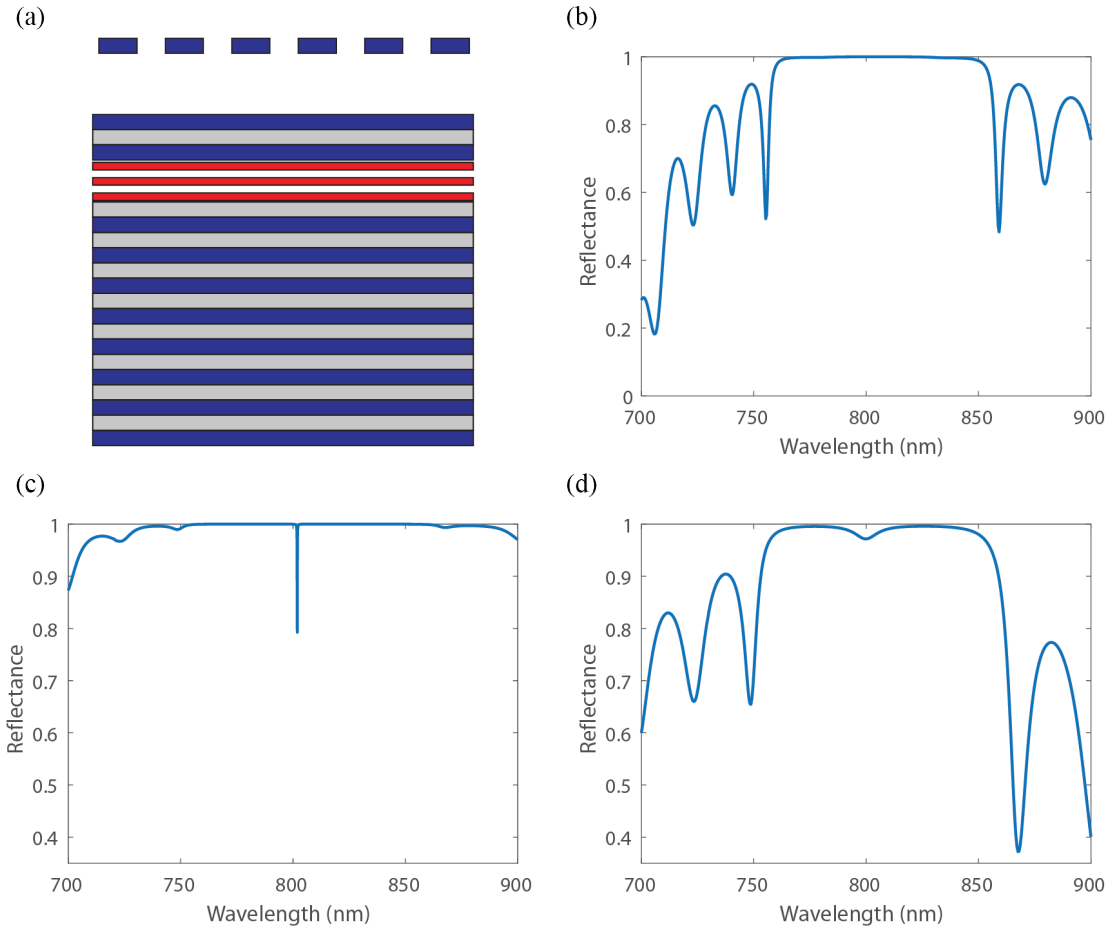

Figure 2.3: Schematic of HCG microcavity and simulated reflectance of the cavity. (a) Schematic view of HCG microcavity. (b) Simulated reflectance spectrum of the wafer before HCG fabrication. (c), (d) Simulated reflectance spectrum of the fabricated cavity in TE and TM, respectively.

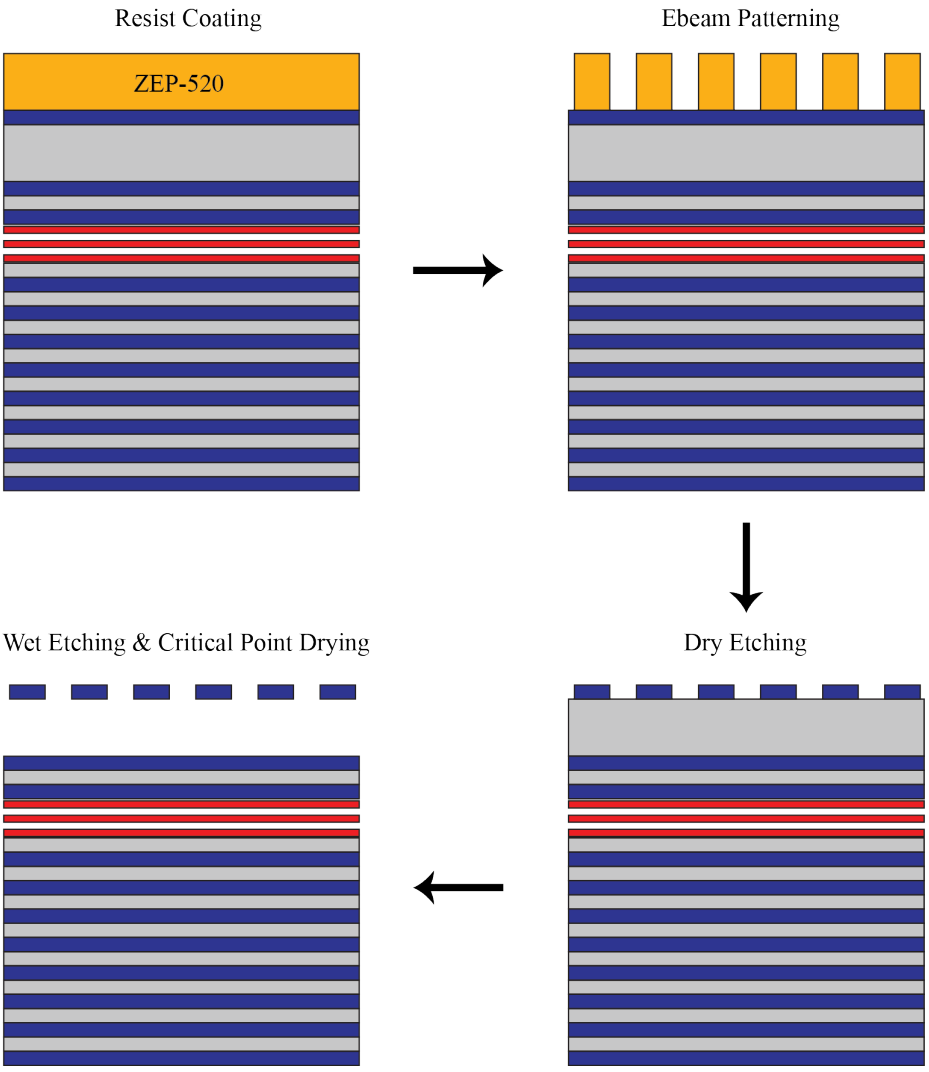

Figure 2.4: HCG fabrication flow.

a scattering of electrons when they interact with the resist and substrate. One can model this effect considering a point spread function (PSF) of electrons [61]. This effect can be minimized by proximity effect correction (PEC) in commercial software BEAMER when preparing exposure files for EBL. Figure 2.5(a) shows an example electron dose distribution as a result of PEC by taking into account a type of resist, substrate, and acceleration voltage. It is clear that the central region requires less electrons because of scattering from adjacent structures. The apparent improvement can be seen by comparing two SEM images of HCGs after development process as shown in Fig. 2.5(b), (c). It is clearly shown that without PEC the center of the grating is overexposed and collapsed resulting in buckling.

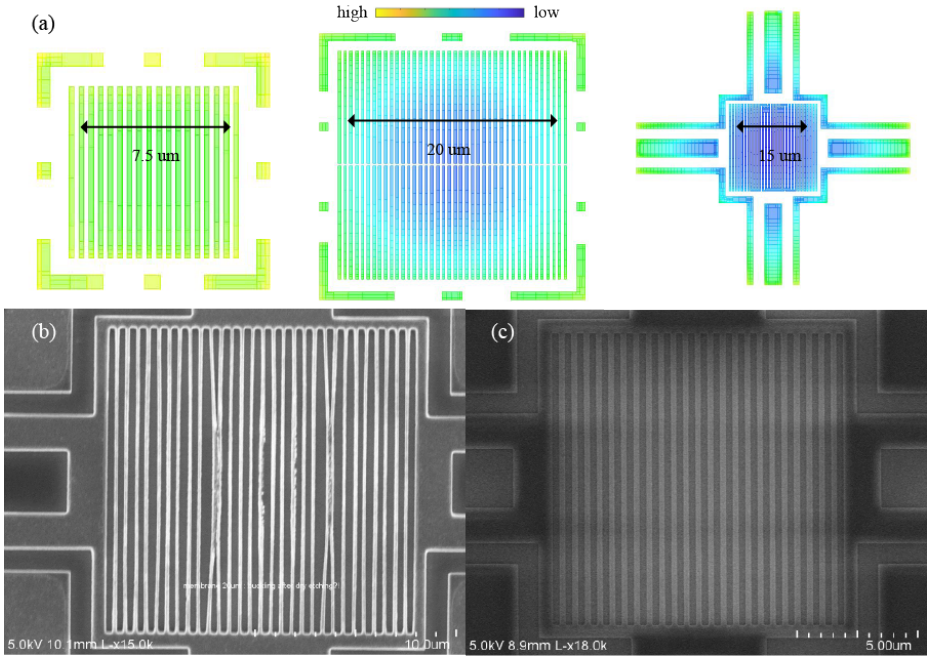

Figure 2.5: Proximity effect correction. (a) Three device examples of electron dose distribution after PEC. (b), (c) SEM top view of the fabricated device without PEC and with PEC, respectively.

Plasma etching process is developed in two different plasma etchers, Oxford plasma lab system 100 and LAM 9400. The main focus in this process is to achieve vertical etching profile of the grating layer. Etching depth is less of a concern as long as the first layer is completely etched through becuase the sacrificial layer will be removed in

later fabrication steps. The sidewall profile can be controlled by etching parameters such as compositions of etching gas, RF bias voltage, etc.

After plasma etching process, the resist is removed and the sample goes through wet etching process followed by critical point drying process. We chose $Al_{0.15}Ga_{0.85}As$ as the grating layer and $Al_{0.85}Ga_{0.15}As$ as the sacrificial layer so that the two layers have large difference in Aluminum (Al) concentration. This leads to very good selectivity between the two layers when concentrated HCl (37%) is used. During 40 seconds of etching process, the sacrificial layer is completely removed while the grating layer is mostly unaffected as shown in Fig. 2.6(a). The top view is shown in Fig. 2.6(b). Since the grating is air-suspended and very fragile, usual evaporative drying process under ambient condition can collapse the HCG due to surface tension between the grating and solvents (e.g. IPA). Therefore, it is important to use critical point drying process, which get rid of abrupt liquid-gas phase transition. For this, we used tousimis automegasamdri-915 which is a CO2-based critical point dryer.

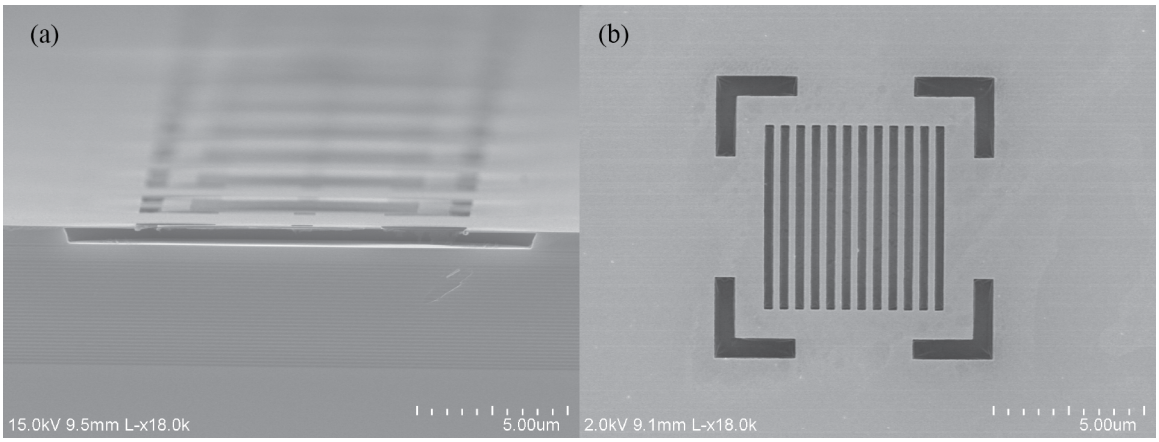

Figure 2.6: SEM side view and top view of HCG. (a) SEM side view of the fabricated HCG. The grating layer is approximately 80 nm and the sacrificial layer of about 600 nm is completely etched. (b) SEM top view of the HCG.

2.1.3 Optical Characterization of HCG Microcavities

For optical measurements, the sample is kept in a cryostat at 5K. We use off-resonant continuous wave (CW) laser for sample excitation. We use electro-optic modulator (EOM) to chop the laser to reduce the sample heating when needed. The first task is to find a signature of strong coupling between excitons and cavity photons. This can be done using momentum (K) space spectroscopy as shown in Fig. 2.7 for TE and TM polarizations. Due to low cavity quality factor, weakly coupled exciton emission is observed in TM. In TE, LP and UP dispersions are observed. This shows the expected polarization-selectivity of the designed HCG. The Rabi splitting and cavity resonance can be determined from these measured LP, UP, and exciton energies. The estimated Rabi splitting of the HCG microcavities is typically around 12 meV which is comparable to GaAs-based DBR microcavities. Discrete LP states appear because of the confinement of photonic modes, resulting from the finite size of the HCG (7.5 μm). This zero dimensional (0D) polariton device provides an opportunity to engineer nonlinear polariton-polariton interaction strength and couple multiple 0D devices for applications such as Josephson physics [33, 32], quantum simulators [43, 62], nonlinear photonic lattices [40, 41], and so on.

Figure 2.8 shows a excitation power dependent spectrum images, integrated intensity, linewidth, and blueshift of the lowest energy state. These sets of data show a nonlinear lasing action of the polariton state. Nonlinear increase of the ground state population accompanied by narrowing of the linewidth indicates coherence buildup which is expected for a laser. The steady blueshift of the lasing state is observed due to the polariton-polariotn interaction. It is important to note that the lasing state in this device is a single-mode in terms of energy as well as polarization unlike DBR based microcavities where two-spin polariton states inherently exist due to spin degeneracy of QW excitons. For laser applications, degenerate spin states introduce shot-to-shot and temporal variations of polarization state of emission [63] and can be

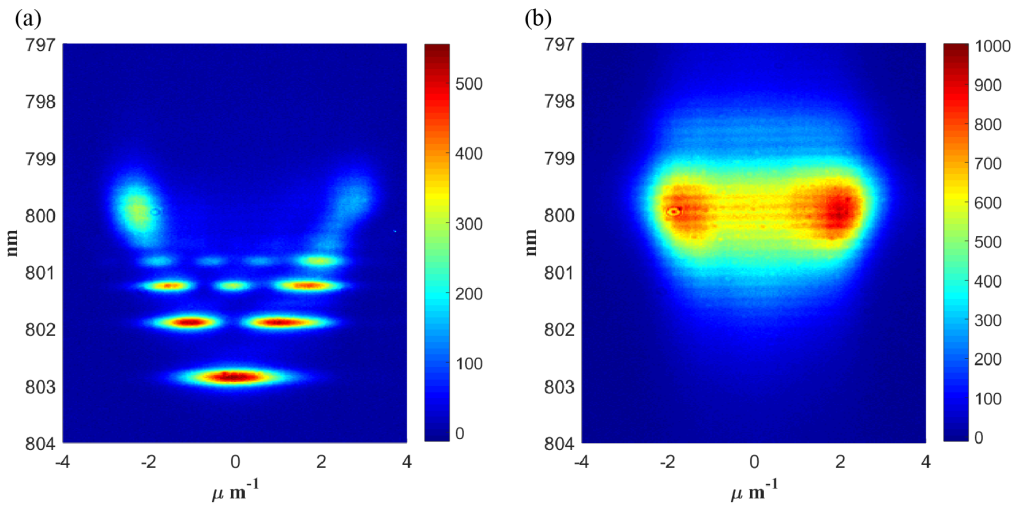

Figure 2.7: K-space spectrum (a) in TE and (b) TM polarizations. TE polarization shows discrete LP states while TM polarization shows uncoupled exciton states.

detrimental. Therefore, HCG microcavities are very promising for practical polariton lasers, which are important for low threshold coherent light sources.

2.2 Monolithic HCG-based microcavities

In this section, I will discuss monolithic HCG (MHCG)-based microcavities. The main difference between MHCG and HCG is that MHCG does not require any undercut process to remove the layer underneath the grating. In principle, we don't even need a second layer at all, which is why it is sometimes referred as zero-contrast grating. This method has a few advantages over conventional air-suspended HCGs. First, the fabrication process can be drastically simplified because we don't need wet etching and drying processes. This also leads to more robust and repeatable fabrication results since the most failure of HCGs occurs during wet etching and drying steps. It also supports arbitrarily large devices without any risk of device damage (mainly due to grating collapse in HCG mirrors) and can be used for making nonlinear photonic lattices. For practical VCSEL application, it might be possible to directly deposit metal layers for current injection on top of the gratings [64]. Finally,

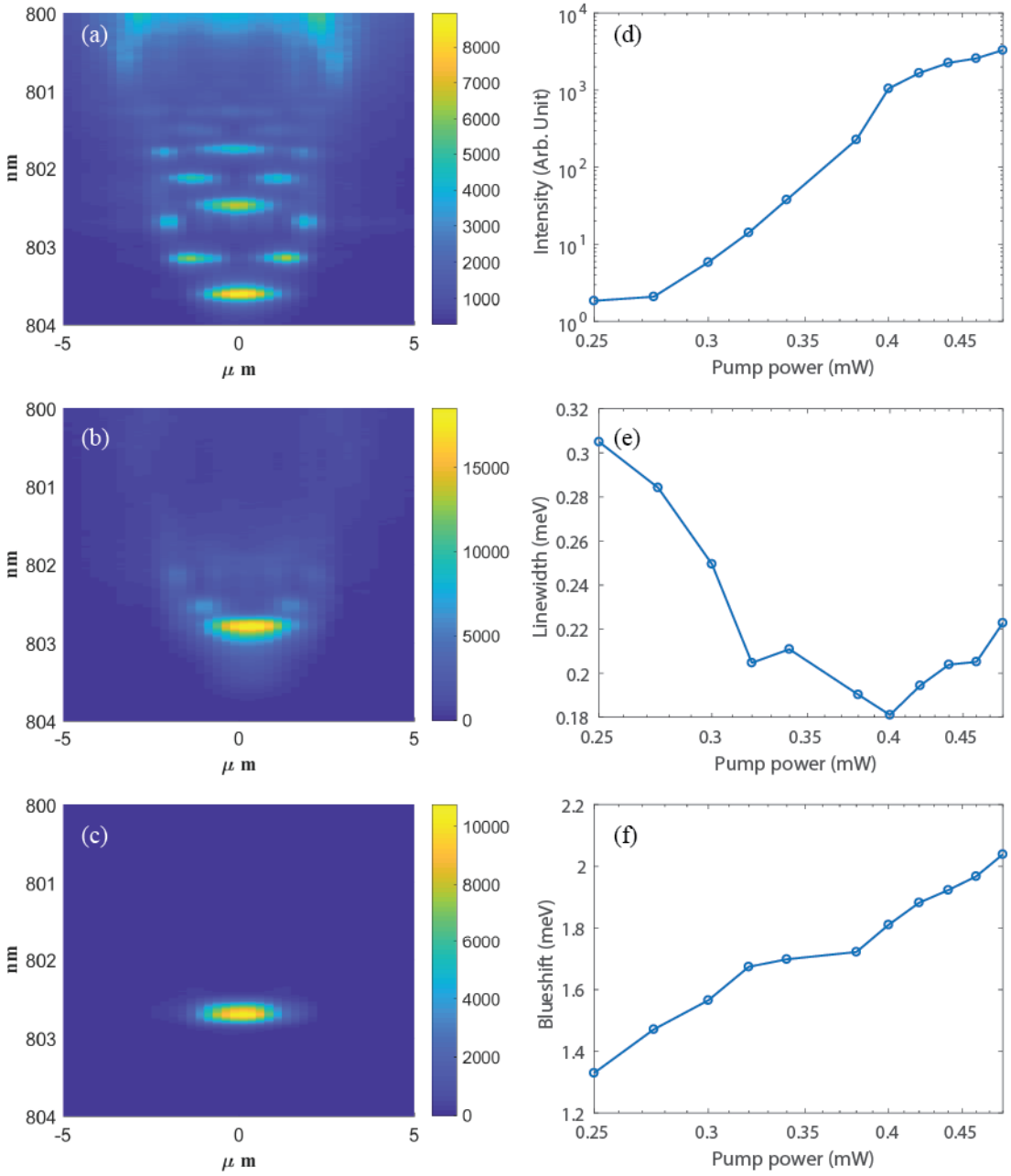

Figure 2.8: Power dependent spectrum, integrated intensity, linewidth, and blueshift of the polariton ground state. Spectrum (a) below, (b) at, (c) above the lasing threshold. (d) Integrated intensity, (e) linewdith, and (f) energy blueshift of the ground state as a function of pump power.

the cavity resonance can be controlled by grating parameters (Λ, η) which may be important for polariton applications such as periodic lateral chains [65].

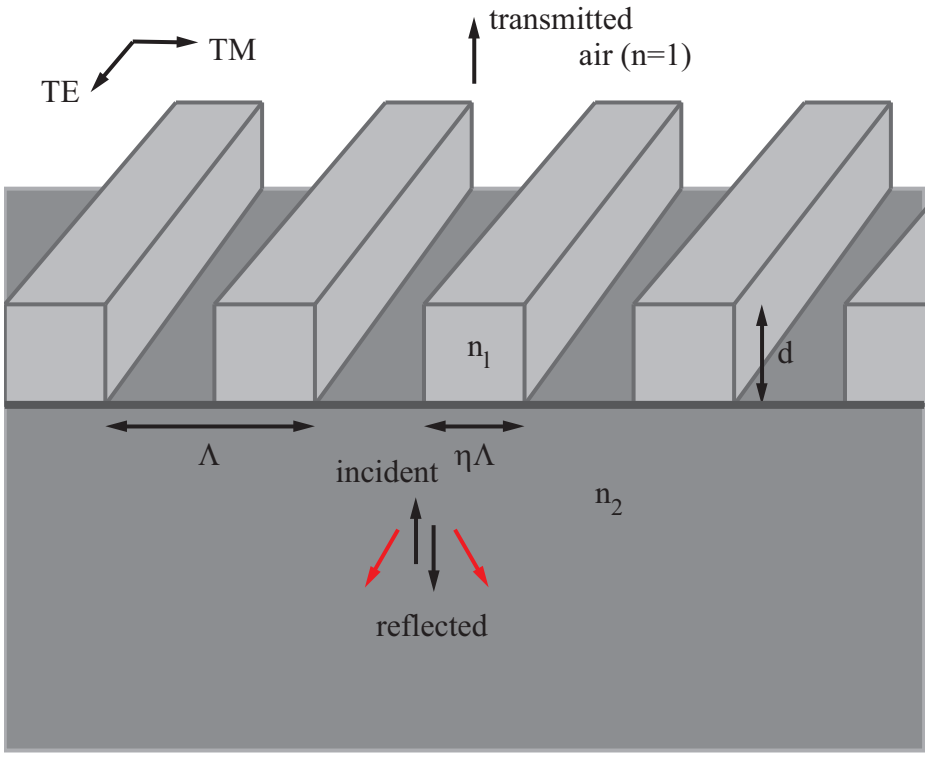

Figure 2.9: Schematic of monolithic HCG. period Λ is grating peiriod, η is duty cycle, d is thickness and n_l is refractive index of the grating layer, and n_2 is refractive index of the second layer. TE and TM denotes the direction of polarization of incident light. Red arrows indicate high-order diffraction orders that may be possible when refractive index difference between n_l and n_2 is small.

2.2.1 RCWA Simulation of MHCG Microcavities

The working principle of MHCG can be explained by the two-mode canceling theory same as HCG. However, compared to conventional HCGs, MHCGs have a higher index material on one side, which may support non-evanescent higher-order diffraction modes (red arrows in Fig. 2.9). In most applications, especially vertical cavities, only the zeroth order reflection is desirable. Therefore, the grating needs

to be carefully engineered to minimize the energy carried away by the higher-order diffractions. Through RCWA simulation, we were able to find the parameters to ensure high reflectance of the MHCGs for TM polarization, with the electric field vector perpendicular to the grating grooves. The MHCG remains low reflectance for TE-polarized light. The simulated reflectance for TM-polarized light in $d/\Lambda - \lambda/\Lambda$ parameter space is shown in Fig. 2.10(a) for $n_l = 3.58$ ($Al_{0.15}Ga_{0.85}As$) and $n_2 = 3.09$ ($Al_{0.85}Ga_{0.15}As$). Figure 2.10(b) shows an example broadband high-reflectance of the HCG mirror.

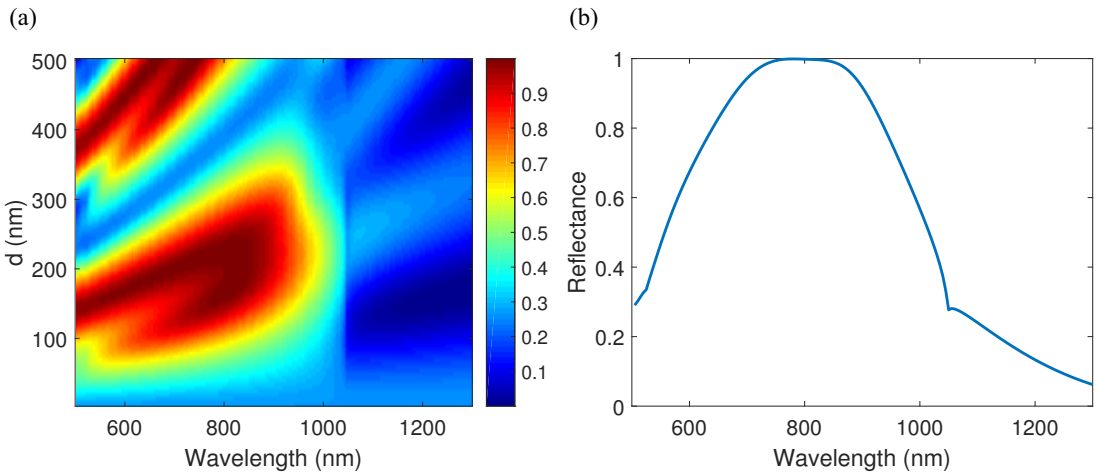

Figure 2.10: RCWA simulation of MHCG. (a) is reflectance map of $d - \lambda$ parameter space. (b) is the reflectance spectrum at $d = 200\ nm$ from (a).

The entire microcavity structure is shown in Fig. 2.11(a). The wafer is epitaxially grown on GaAs substrate with 30 pairs of bottom DBRs, 12 GaAs quantum wells in an AlAs $\lambda/2$ cavity layer, 2.5 pairs of top DBRs, an $Al_{0.85}Ga_{0.15}As$ second layer, and an $Al_{0.15}Ga_{0.85}As$ grating layer. The thickness of the grating layer is about 220 nm and the second layer is about 590 nm. The reflectance measurement of the unprocessed wafer and transfer matrix simulation is shown in Fig. 2.11(b). The simulated reflectance of the MHCG microcavity, without considering absorption of quantum wells is shown in Fig. 2.11(c),(d) for TM, TE polarization respectively.

For this MHCG design, one can control the cavity resonance wavelength through

periods and duty cycles. The RCWA simulation on this tuning capability is shown in Fig. 2.12. In theory, it is possible to tune the resonance by 25 nm while keeping the quality factor higher than 1,000.

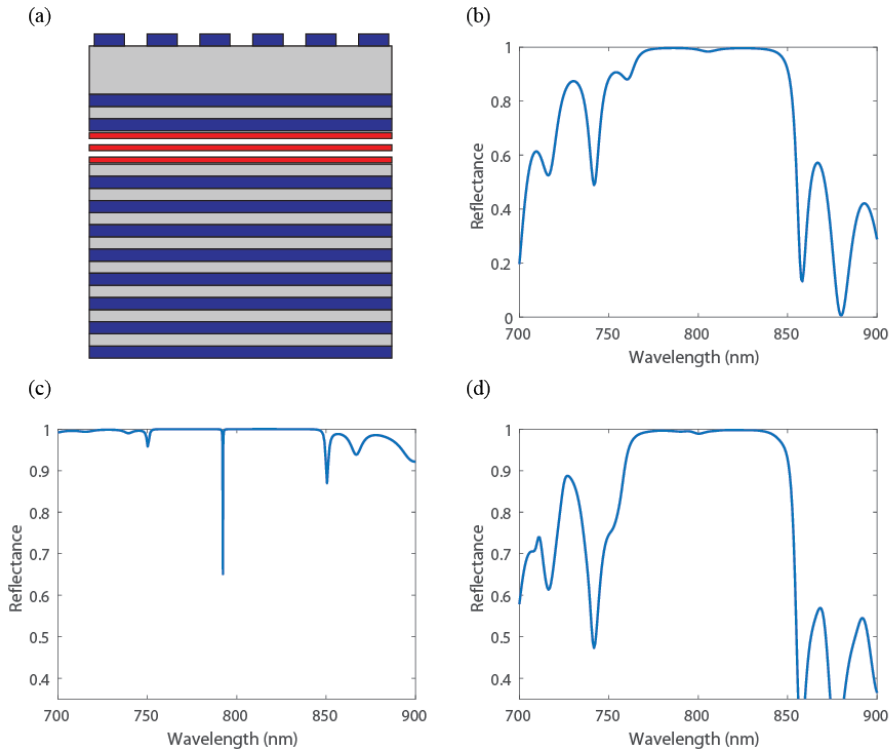

Figure 2.11: Schematic of MHCG microcavity and simulated reflectance of the cavity. (a) Schematic view of MHCG microcavity. (b) Simulated reflectance spectrum of the wafer before MHCG fabrication. (c), (d) Simulated reflectance spectrum of the fabricated cavity in TE and TM, respectively.

2.2.2 Fabrication Process of MHCG Microcavities

The fabrication process involves electron beam lithography (EBL), plasma etching. The schematic flow is shown in Fig. 2.13. Details on each process will be discussed in the following.

EBL process is exactly the same as HCG fabrication. However, fabrication challenge for MHCG is in plasma etching process. To get the perfect rectangular grating profile with well-defined grating height, the etch stop layer is desirable. Otherwise, different etching depth for different grating parameters and non-flat etched surface

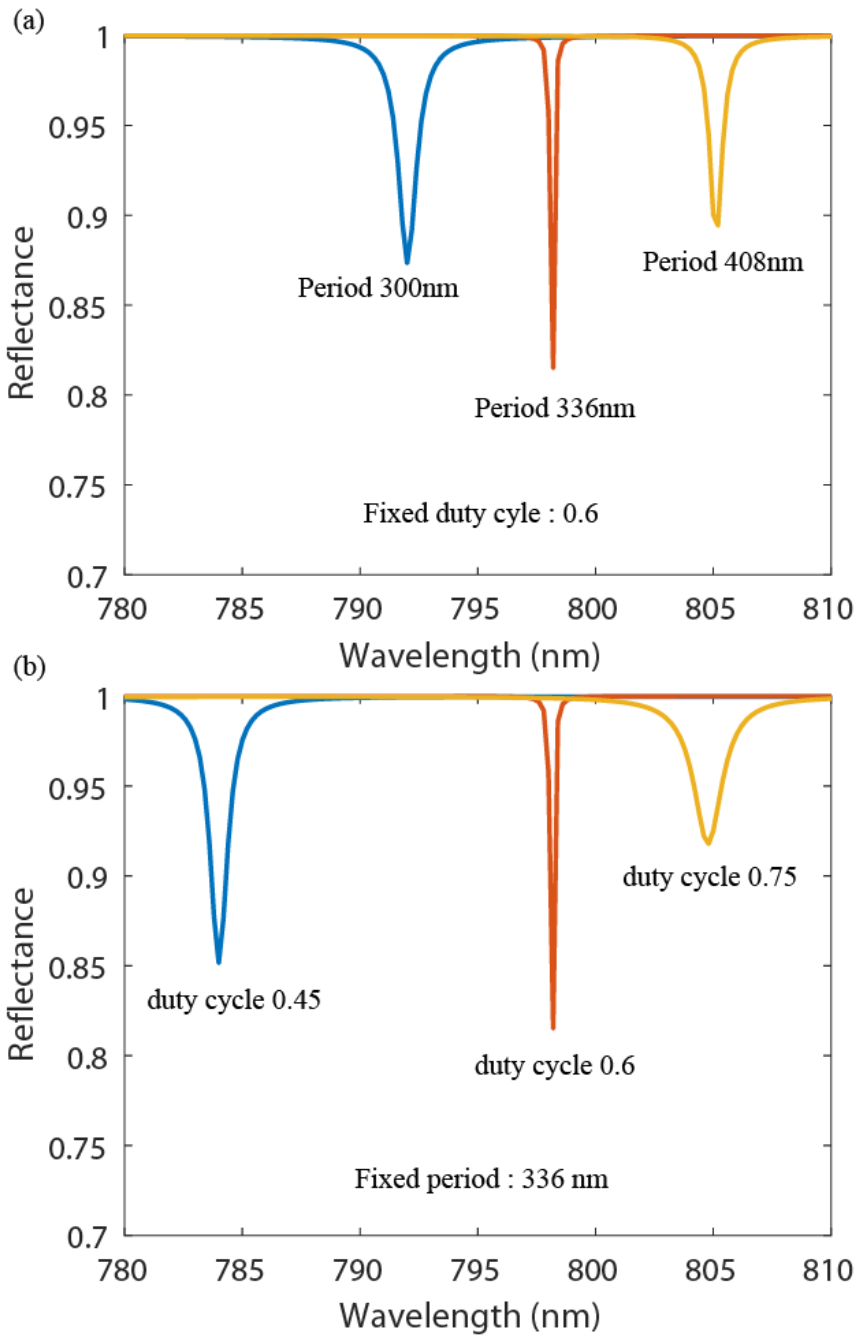

Figure 2.12: MHCG microcavity resonance tuning. (a) Spectrum near resonance for (a) three different periods and (b) three different duty cycle.

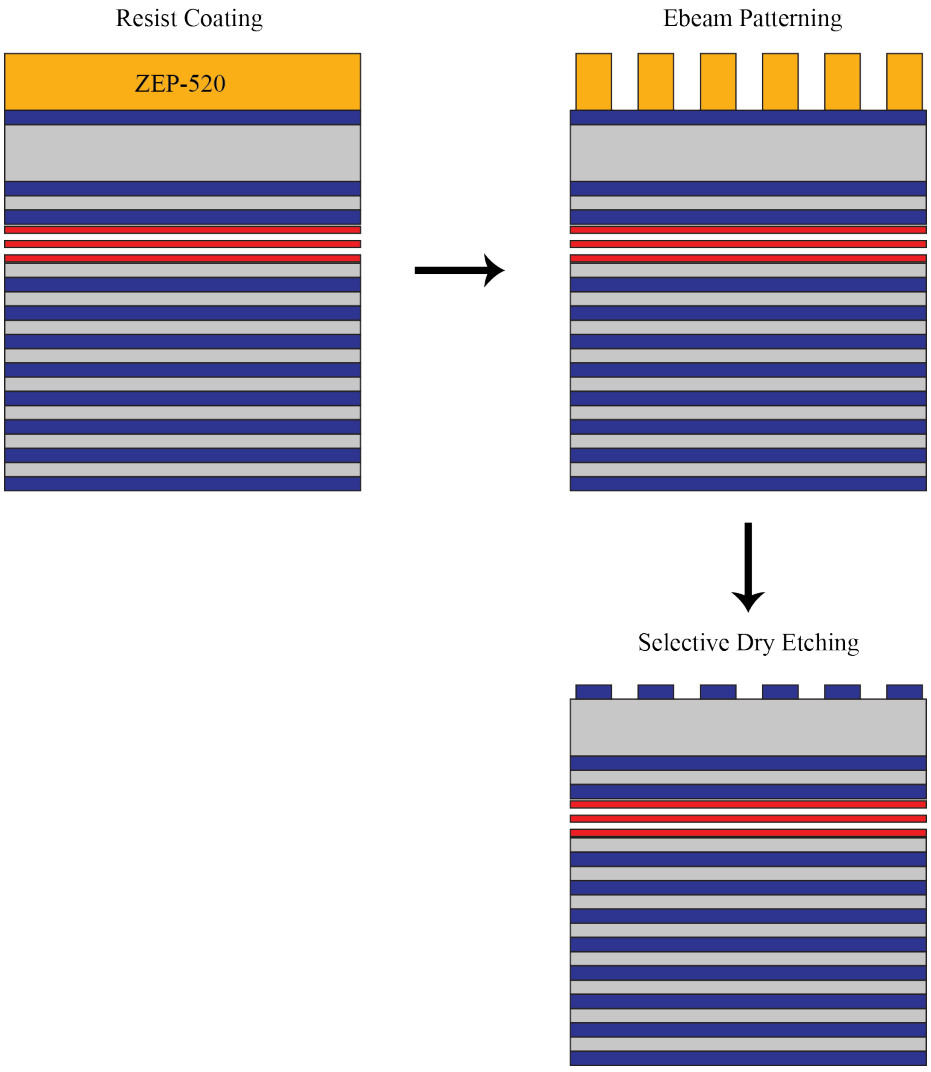

Figure 2.13: MHCG fabrication flow

may shift / degrade the cavity resonance. Fortunately, we have slightly different layers for the grating and the second layers. We can take advantage of different Al compositions and make a layer with high Al concentration (second layer) an etch stop layer. It is well-known that reacting Al with Flouride (F) results in AlF_x which is difficult to etch, giving high selectivity between layers with different Al concentrations. One thing to consider is that the grating layer also has 15% Al and reacts to F. When etching, AlF_x passivates the side-wall and make the side-wall profile angled (Fig. 2.14(a). To overcome this, we use two-step etching process, non-selective etching followed by selective etching. The result of this two-step etching is shown in 2.14(b). With this technique, nearly perfect gratings with vertical side-wall and well-defined grating height were possible.

2.2.3 Optical Characterization of MHCG Microcavities

Strong coupling is evident from the angle-resolved PL at low pump powers that shows dispersions of the lower polariton (LP) branch and upper polariton (UP) branch in TM polarization, centered in k-space at k=0 at 799.7 nm and 794.3 nm, respectively (Fig. 2.15(a), (b)). The TE-polarized PL shows emission from excitons at around 797.5 nm, which are not strongly coupled to the cavity modes as the reflectance of MHCG is low for TE. The existence of two exciton lines could be caused by interlayer variations of QWs [66]. The exciton mode around 796 nm shown in TM polarization is possibly from QWs that are not overlapped with electric field maxima inside the cavity and therefore are not coupled to the cavity. This is consistent with the simulated electric field distribution inside the cavity, where the field maxima is slightly off-centered from QWs. From the measured LP, UP, and TE exciton energies at k = 0, we obtain the normal mode splitting of 10.2 meV and exciton-photon detuning of 2.4 meV. Here, we use the exciton energy from the exciton emission appearing only at TE polarization. The calculated cavity resonance and exciton resonance from TE

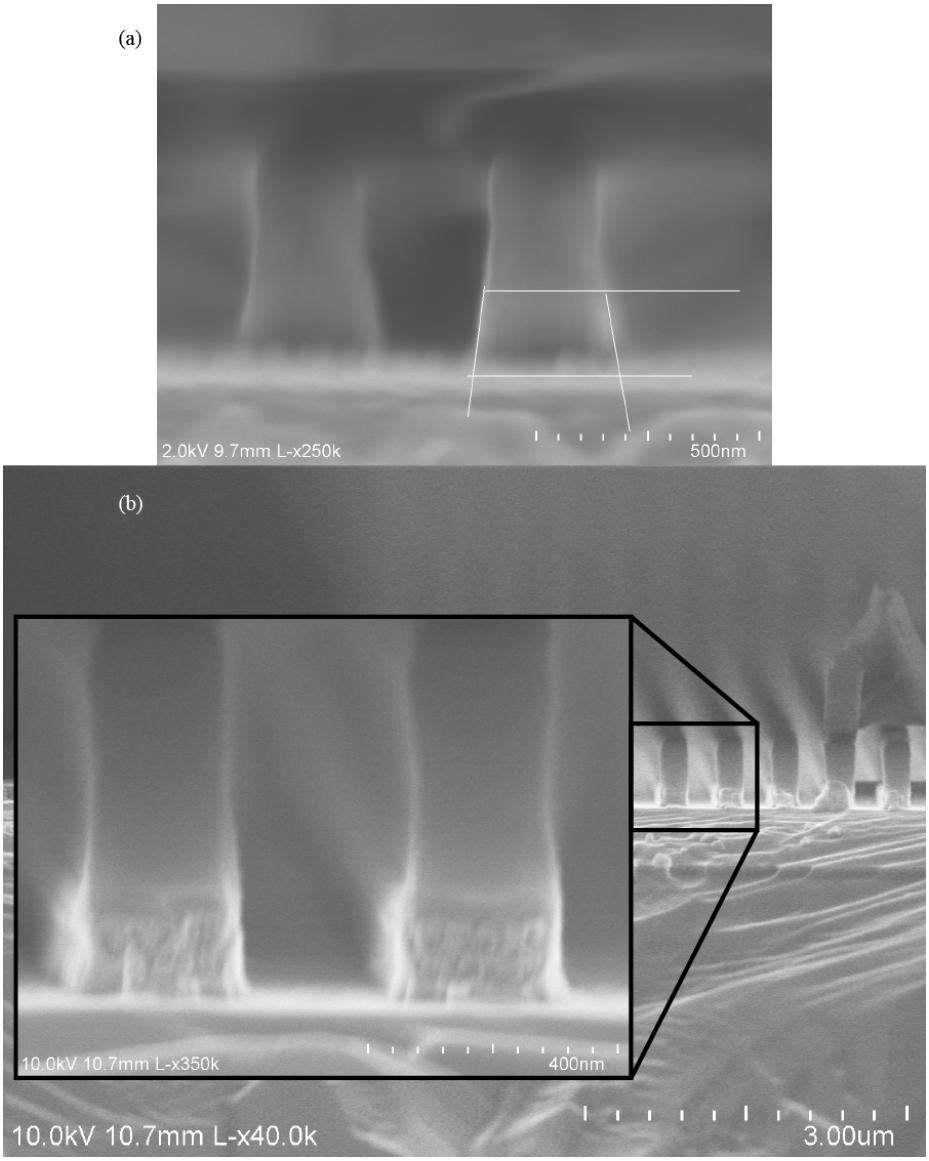

Figure 2.14: Selective dry etching development. (a) SEM side view after selective dry etching. The etching profile is slanted because of the passivation effect. (b) SEM side view after nonselective etching followed by selective etching. The results show vertical side wall profile and clean etched surface.

are indicated by red and white lines respectively in Fig. 2.15(a).

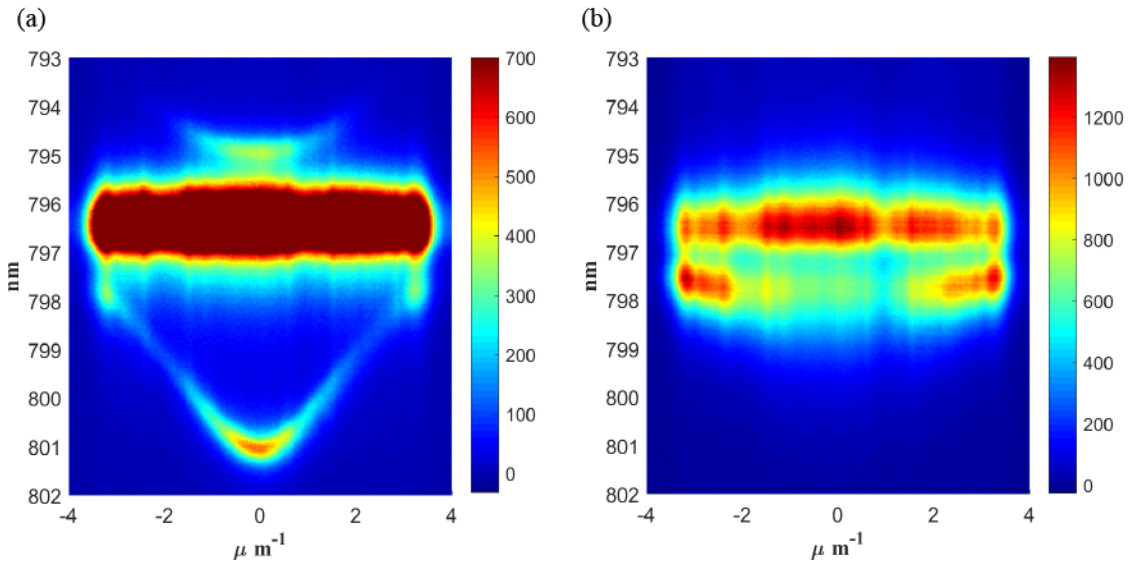

Figure 2.15: K-space spectrum (a) in TM and (b) TE polarizations. TM polarization shows dispersion of LP states while TE polarization shows uncoupled exciton states.

The power-dependent input-output relationship is shown in Fig. 2.16. We observe a nonlinear increase in the emission intensity at the threshold pump intensity of 2,000 W/cm^2, accompanied by the linewidth narrowing of the lasing mode at $k = 0$ (2.16(d)). The spectrum at the threshold is shown in Fig. 2.16(b), where the polaritons mostly relaxed into $k = 0$. The linewidth above the threshold approaches quickly to the resolution limit of about 0.03 nm, as shown in Fig. 2.16(e). The lasing mode blueshifts smoothly as the pump power increases (see Fig. 2.16(f)) due to the polariton-polariton interactions, while remaining well below both the exciton and cavity energies. These results clearly show polariton lasing characteristics of the microcavity. The threshold intensity is comparable to other polariton devices [67]. We observed similar lasing phenomena from MHCG devices with different cavity resonances which confirms the robustness of high quality MHCGs of varying parameters.

Finally, we demonstrate the tuning of the cavity resonances and polariton laser energy with respect to the grating period (Fig. 2.17). Unlike with DBRs, it is

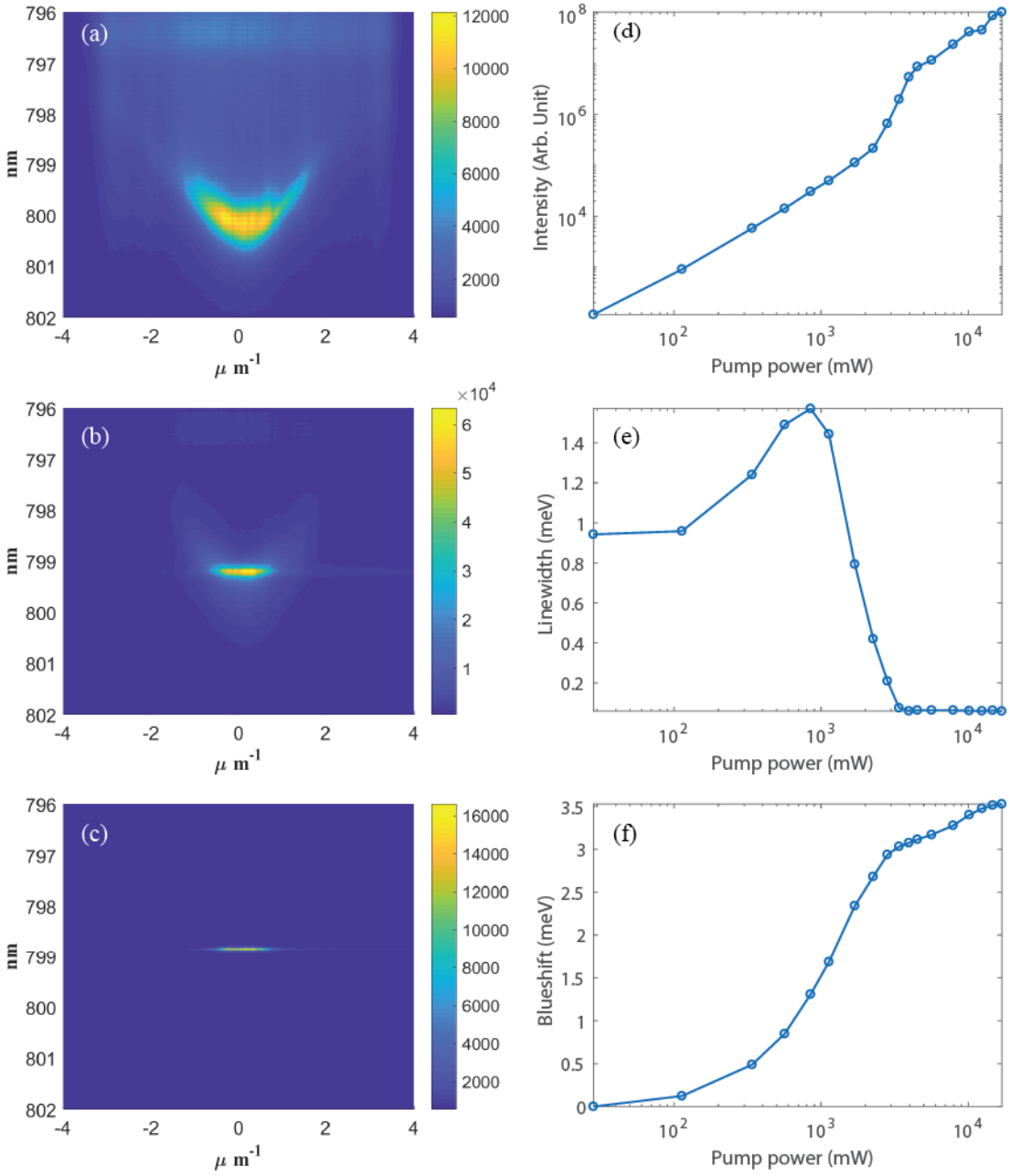

Figure 2.16: Power dependent spectrum, integrated intensity, linewidth, and blueshift of the polariton ground state. Spectrum (a) below, (b) at, (c) above the lasing threshold. (d) Integrated intensity, (e) linewdith, and (f) energy blueshift of the ground state as a function of pump power.

possible to engineer the reflection phase of the HCG by tuning grating parameters. The reflection phase of the mirror determines the phase matching condition for the cavity modes and therefore directly influences the cavity resonance. Here, we tune the reflection phase by changing the grating periods. As shown in Figure 2.17(a)-(b), the LP and UP resonances redshift as the grating period increases from 328 nm to 344 nm. Using the measured LP, UP and TE exciton energies, we calculate the corresponding cavity resonance energy, which changes approximately linearly with the period. A linear fit yields 1 nm of resonance shift per 10.12 nm of change in the grating period. This result is in excellent agreement with the RCWA simulation indicated by the cross marks in Fig. 2.17(a). Here we fixed the duty cycle at 0.7 as measured by SEM.

Polariton lasing is achieved in all the gratings across the tuning range. The lasing wavelength for different periods are shown in Fig 4(c). We use the same pump intensities for different devices to make sure that the lasing wavelengths are not affected by the blueshift caused by the exciton reservoir. Above the threshold, the linewidths become narrower and emission from the different MHCGs become well separated spectrally. This would be important for applications such as on-chip multiwavelength laser arrays for wavelength division multiplexing [68].

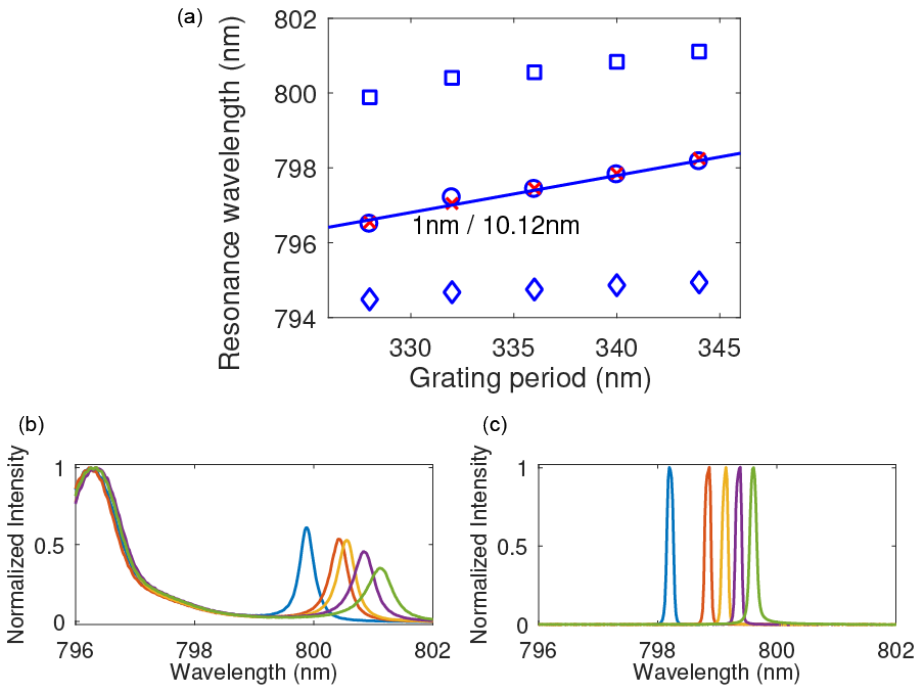

Figure 2.17: Tuning of the emission wavelength by the grating period. (a) Measured LP and UP resonances (open diamonds and squares, respectively) at low pump powers and the corresponding cavity resonances as a function of the grating period. The cavity resonances obtained from the measured LP, UP, and exciton resonances are marked by the open circles, while the cavity resonances calculated by the RCWA are marked by the red crosses. The solid line is a linear fit to the experimental cavity resonance vs period, showing tuning of the cavity resonance with the grating period at 1 nm/10.12 nm. (b) Emission spectrum at low pump powers as the grating period of the MHCG is varied from 328 to 344 nm with 4 nm increment. The LP resonance shifts toward longer wavelengths as the period increases. The exciton resonance remains the same in all the spectra. (c) Emission spectra of the lasing state at high pump powers for the corresponding MHCGs as in (b).

CHAPTER III

Coherent Polariton Lasing

Quantum coherence is one of the most defining features of lasers. It is usually characterized by field correlation functions for distinct space coordinates or time coordinate. For lasers, it is critical to have narrow linewidth and small intensity noise, which are defined by temporal first and second-order coherence functions. Naturally, as a coherent light emitted from a coherent condensate, polariton lasers have been the subject of detailed investigation of their quantum coherence properties [25, 69, 26]. However, the measured coherence properties of early experiments indicate a distinct deviation from the usual photon lasers. These experiments have led to detailed theoretical works taking into account the key feature that polaritons are interacting unlike photons [70, 71, 72, 73]. Due to repulsive polariton-polariton interactions, much larger intensity noise than shot-noise limit has bean measured in 2D polariton systems where the condensed polaritons can scatter into non-condensed state mediated by polariton-polariton interactions. Also, degenerate spin states lead to poorly defined polarization state of polariton lasers due to intensity and phase fluctuations between two spin states [63]. The intensity fluctuation in 2D systems, in turn, lead to phase decoherence of the lasing state [69]. This can be understood in spectral domain or time domain. In time domain, one can think of quantum scattering process between two particles with repulsive potential. As one particle scatters with

the other, the change of its phase is determined by the path integral of repulsive potential. This scattering process randomized phase relationship between particles (in this case polaritons) and induces phase decoherence. In spectral domain, one can look at the energy of the lasing state. Because of the repulsive interactions, when the polariton population is large the polariton energy goes up and vice versa. Therefore, population fluctuation leads to energy fluctuation of the lasing state, equivalent to the broadened linewidth or phase decoherence.

HCG-based microcavities are good candidate to overcome all the aforementioned problems that degrade quantum coherence of polariton lasing. First, the ground state can be well separated energetically from the next excited state due to spatial confinement which suppresses the scattering to the non-condensed state from condensed state. Second, the polarization is well defined in either TE or TM by HCG design which get rid of scattering between different spin states. In this chapter, I'll present detailed experimental and theoretical studies of HCG-microcavity polariton lasers. I'll present the single-mode lasing scenario as well as multi-mode lasing scenario which shows the importance of single-mode state lasing in coherence properties. Then, I'll discuss about optimization of the coherence properties of polariton lasers via modifying interaction strengths and our efforts toward developing highly coherent polariton lasers with 300-fold increase of coherence time compared to the lifetime.

3.1 Theory of Quantum Coherence

The quantum theory of optical coherence is formulated on quantum correlation between electric field operators [74]. For convenience, we can define the field operator by Fourier integral with positive and negative frequency components.

$$\boldsymbol{E}(\boldsymbol{r},t) = \int_0^\infty (\boldsymbol{e}(\boldsymbol{r},\omega) + \boldsymbol{e}^\dagger(\boldsymbol{r},\omega))e^{-i\omega t}d\omega = \boldsymbol{E}^{(+)}(\boldsymbol{r},t) + \boldsymbol{E}^{(-)}(\boldsymbol{r},t) \tag{3.1}$$

It is shown that $\boldsymbol{E}^{(+)}$ and $\boldsymbol{E}^{(-)}$ are photon annihilation and creation operators, respectively. If we consider a single polarization state, we can define the a field correlation function and a second-order correlation functions as,

$$G^{(1)}(\boldsymbol{r}_1 t_1, \boldsymbol{r}_2 t_2) = Tr\{\rho E^{(-)}(\boldsymbol{r}_1, t_1) E^{(+)}(\boldsymbol{r}_2, t_2)\} \tag{3.2a}$$

$$G^{(2)}(\boldsymbol{r}_1 t_1, \boldsymbol{r}_2 t_2, \boldsymbol{r}_3 t_3, \boldsymbol{r}_4 t_4) = Tr\{\rho E^{(-)}(\boldsymbol{r}_1, t) E^{(-)}(\boldsymbol{r}_2, t_2) E^{(+)}(\boldsymbol{r}_3, t_3) E^{(+)}(\boldsymbol{r}_4, t_4)\}. \tag{3.2b}$$

An nth-order correlation function may be constructed in a straightforward way.

Now, let me discuss how an nth-order field correlation function helps understand coherence of light. I'll focus on first- and second-order coherence functions which characterize phase and intensity coherence of the light source. For example, let's assume we have N number of random emitters with Gaussian distribution of emission frequency centered at ω_0. This can be written as, $E(t) = E_0 \sum_{i=1}^{N} \exp(-\omega_i t + i\phi_i)$. Then, the first-order correlation function for this light source becomes,

$$\langle E^*(t) E(t+\tau) \rangle = E_0^2 \sum_{i,j=1}^{N} \langle \exp(i\omega_i t - i\phi_i - i\omega_j (t+\tau) + i\phi_j) \rangle \tag{3.3}$$

If we convert the sum into an integral and ignore $i \neq j$,

$$\langle E^*(t) E(t+\tau) \rangle = N E_0^2 (2\pi \Delta\omega^2)^{-1/2} \int_0^\infty d\omega \{\exp(-i\omega_i \tau) \exp(-(\omega_0 - \omega)^2 / 2\Delta\omega^2)\} \tag{3.4}$$

Therefore, the normalized first-order correlation function is

$$g^{(1)}(\tau) = \exp(-i\omega_0 \tau - \frac{1}{2}\Delta\omega^2 \tau^2) = \exp(-i\omega_0 \tau - \frac{\pi}{2}(\tau/\tau_c)^2) \tag{3.5}$$

The decay time of the first-order correlation function is directly related to the width of the spectrum. This also means the phase of the light source at time $t + \tau_c$ is

no longer significantly correlated with the phase at time t. The relationship between spectrum and first-order correlation function for arbitrary stationary light is called Wiener-Khinchin theorem,

$$F(\omega) = \frac{1}{\pi}\mathrm{Re}\int_0^\infty d\tau\{g^{(1)}(\tau)e^{i\omega\tau}\} \tag{3.6}$$

The second-order correlation function characterizes intensity coherence of measured light sources. For classical light, the normalized second-order correlation function at $\tau = 0$ can be written as,

$$g^{(2)}(\tau = 0) = 1 + \frac{\langle \Delta I(t)^2 \rangle}{\langle I(t) \rangle^2} \tag{3.7}$$

where $\Delta I(t) = I(t) - \langle I(t) \rangle$. The minimum possible value of $g^{(2)}(0)$ for any classical light source is 1 which can be found from a coherent light with Poisson photon statistics. A single-mode thermal light, on the other hand, shows $g^{(2)}(0) = 2$ which means the intensity fluctuation can be as large as its average intensity.

3.2 Optical coherence of 0D microcavity

In this section, experimental measurements and theoretical analysis of coherence properties in a 0D HCG microcavity with discrete polariton energies are presented. First- and second-order temporal correlation functions, phase and intensity coherence, are measured to quantify the degree of coherence in polariton lasing states. Fully coherent, up to second-order, was measured from single-mode lasing state in stark contrast to earlier investigations in 2D polariton lasing. This is an important progress toward developing practical polariton lasers as HCG has no strict material restriction and can be incorporated into other polariton material systems operating at room temperature [21, 22].

3.2.1 Experimental Details and Setup

The schematic of experimental setup is shown in Fig. 3.1. The sample was kept at 5K in an optical cryostat. We used an objective lens with NA 0.5 for both excitation and collection of light. For excitation, we either use an intensity-stabilized Ti:Sapphire CW laser (Msquared SolsTiS) or a mode-locked Ti:Sapphire laser (Spectra-Physics Tsunami) with a 100 fs pulse width. For CW excitation, we used electro-optic modulator to reduce the sample heating. The presence of sample heating was mainly identified through energy shift of the polariton mode as the heating redshifts the polariton energies. The excitation light was off-resonant and orthogonally polarized compared to the emitted light. This excitation scheme makes sure that the coherence of polariton states is not inherited from the coherence of excitation lasers and also no reflected light from excitation lasers contaminates the coherence measurements as it is very easy to suppress the reflected light by means of spectral filters and polarizers. The emission from the sample is then sent to Michelson interferometer for first-order coherence, Hanbury Brown and Twiss (HBT) interferometer for second-order coherence, and grating-based spectrometer.

Time-delay between two arms of Michelson interferometer was given by the motorized linear stage with the resolution less than 10 fs. The thermoelectric-cooled camera was used for good signal-to-noise ratio. The $g^{(1)}(\tau)$ measurement was fully automized with LabVIEW for fast measurements, especially important for 0D device as it is sensitive to any drift of the pump position (mainly due to sample drift in a cryostat, but could be caused by any drift in control stages for the sample or optics).

Second-order correlation functions are measured by HBT interferometer. The signal was first sent to the grating-based spectrometer and split into two interferometer arms. Each arm has a mechanical slit and a monitoring CMOS camera to separate different lasing states when applicable. Therefore, auto-correlation as well as cross-correlation fuctions between polariton states were conveniently measured. Avalanche

photo diodes (APDs) have a time resolution of about 40 ps and a time interval analyzer (TIA, PicoQuant HydraHarp 400) was used to collect photon correlation data.

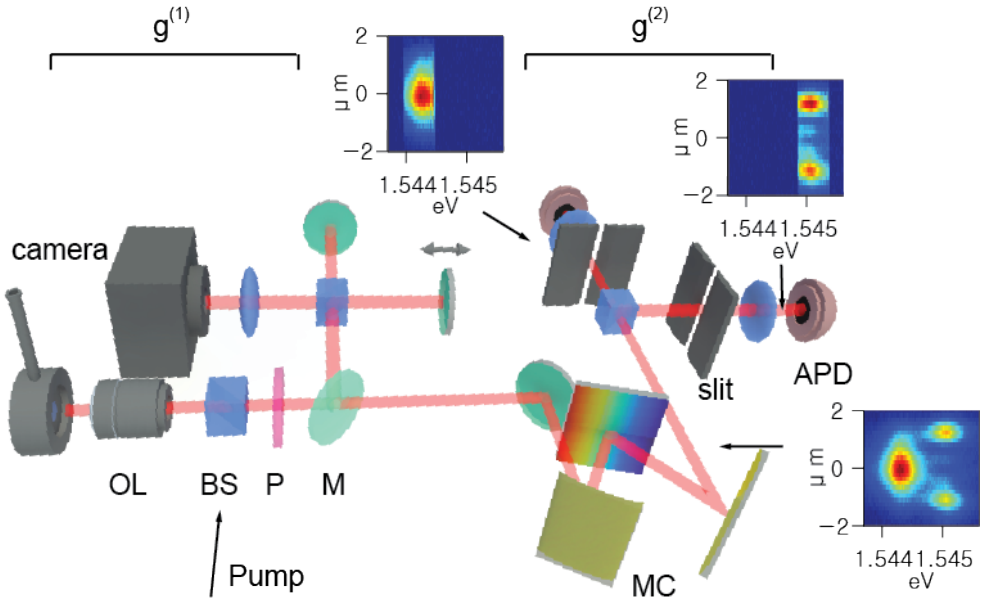

Figure 3.1: Schematic of the experimental setup. OL: Objective lens, BS: Beam splitter, P: Polarizer, M: Mirror, MC: Monochromator, and APD: Avalanche photodetector. For the $g^{(2)}$ measurements, a monochromator followed by two mechanical slits was used to spectrally filter the discrete polariton states. Examples are shown for the spectrally-resolved real space images of the lowest two LP states right after the monochromator (bottom), the spectrally filtered ground state (top left) and the spectrally filtered first excited state (top right). The resolution of the spectral filter was about 0.08 nm, determined by the monochrometer resolution.

3.2.2 Single-mode Polariton Lasing

For single-mode polariton lasing, we positioned an excitation laser at the center of the 0D device to maximize the spatial overlap between the pump spot and the ground state wavefunction and ensure ground-state lasing only as shown in Fig. 3.2.

The excitation power-dependent input-ouput relation is shown in Fig. 3.3 for both pulsed ((a),(b),(c)) and CW ((d),(e),(f)) excitations. For pulsed excitation, we observed a second threshold, one of many evidences of strong-coupling regime be-

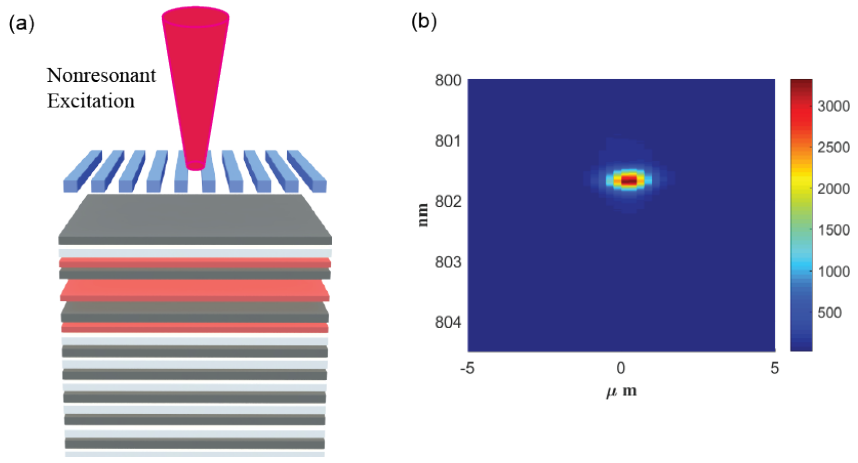

Figure 3.2: Pump position for single-mode lasing. (a) Pump spot is focused at the center of the device. (b) Spectrum above the lasing threshold.

fore this threshold. The presence of the second threshold only in pulsed excitation may be due to the peak exciton density can be much higher for pulsed than for CW excitation. Also, it is important to point out that the linewidth of polariton lasing state measured by grating-based spectrometer increases above the lasing threshold as the pump power increases for pulsed excitation. This effect should be distinguished from the intrinsic linewidth of the polariton lasing as this is absent in CW excitation and should be understood as transient effect due to transient change in population affecting the instantaneous energy and the linewidth looks broad when integrated in time. The intrinsic linewidth should be measured with CW excitation and was resolution limited in grating-based spectrometer. For higher spectral resolution, Michelson interferometer was used in this experiment.

We characterized the intensity noise of the polariton laser by measurements of $g^{(2)}(\tau)$ using HBT setup, under both pulsed and continuous-wave (CW) excitations.

The measured auto-correlation function, $\overline{g^{(2)}}(0)$, is an average of the actual $g^{(2)}(\tau)$ over the time resolution of the measurement. Hence when the time resolution is much longer than the intensity correlation time, the measured $\overline{g^{(2)}}(0)$ approaches 1 due to averaging. When the time resolution is shorter than the intensity correlation time,

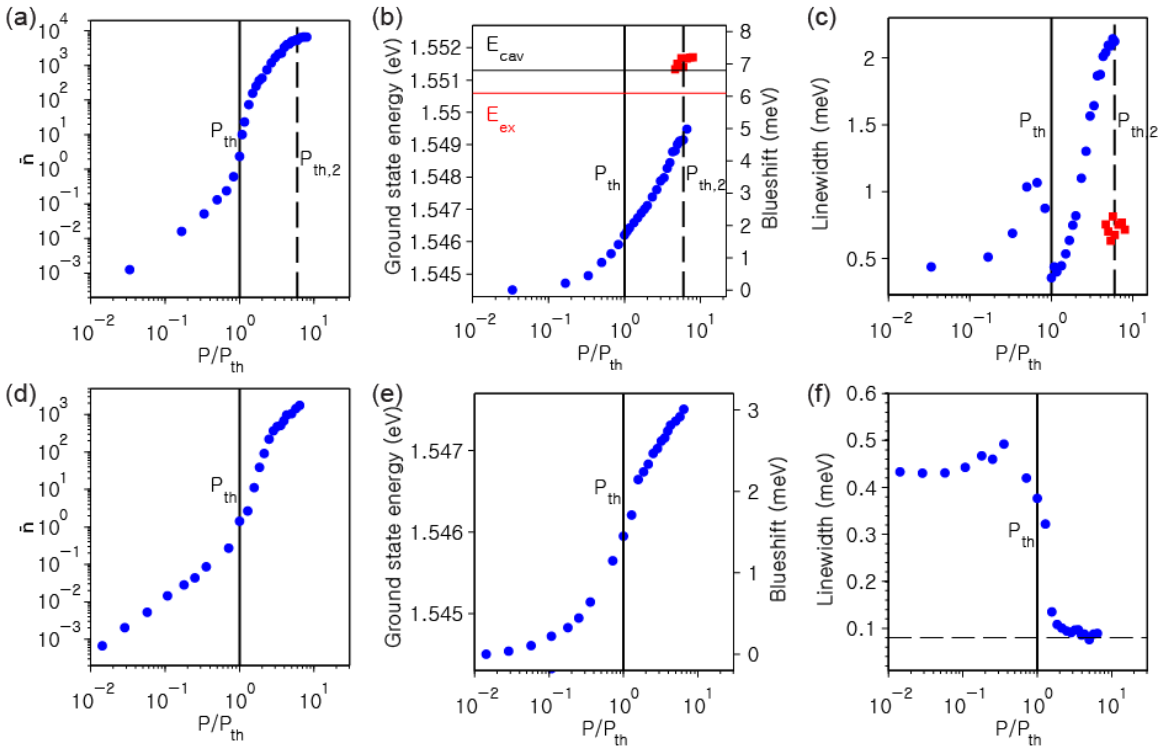

Figure 3.3: Intensity and spectral properties of the single-mode polariton laser. (a) The occupation number vs. P/P_{th} for pulsed excitation. P_{th} indicates the threshold for polariton lasing and $P_{th,2}$ indicates the threshold for photon lasing. $\bar{n}$ is estimated from the independently measured PL intensity from the ground state, collection and detection efficiencies of the setup, and the polariton lifetime [1, 2]. (b) Energy and blueshift of the polariton ground state (dots) and lasing photon mode (squares) vs. the normalized pump powers P/P_{th} for pulsed excitation. Here P_{th} is the pump power at the polariton lasing threshold. The solid vertical line marks the polariton lasing threshold and the dashed vertical line marks the photon lasing threshold. (c) The linewidth (full-width at half-maximum) of the polariton ground state vs. P/P_{th} for pulsed excitation. (d), (e), (f) The occupation number, blueshift, and linewidth of the polariton ground state vs. P/P_{th} for CW excitation. The dashed line in (F) represents the spectral resolution of the monochromator of about 0.08 nm.

$\overline{g^{(2)}}(0)$ approaches the actual $g^{(2)}(0)$. In CW measurements, the time resolution is determined by the response time of the photon counters, which was measured to be ~40 ps for both of our counters. In pulsed measurements, often $\overline{g^{(2)}}(0)$ is obtained by integration over the whole pulse and thus the time resolution is determined by the duration of the measured pulses, ΔT. In our experiments, the polariton emission pulse shortened rapidly from $\gg 40$ ps below threshold to <4 ps above threshold due to the stimulated scattering (Fig. 3.4). Correspondingly, an increase of $\overline{g^{(2)}}(0)$ near the threshold was observed (Fig. 3.5(a),(c)).

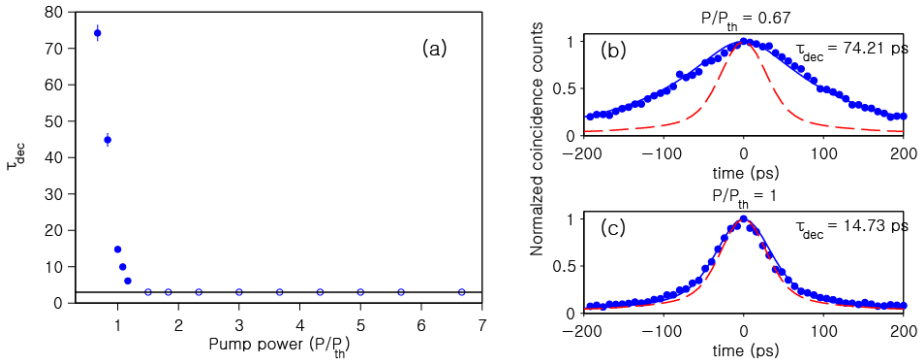

Figure 3.4: (a) The pulse duration of the ground state polariton emission ΔT vs. the normalized pump power P/P_{th}. ΔT are obtained by fitting $g^{(2)}(\tau)$ measured for two uncorrelated pulses, taking into account the measured IRFs of the photon counters. ΔT was well fitted at $P/P_{th} < 1.5$ (dots) and unresolvable at $P/P_{th} > 1.5$ (circles). The solid line is the intensity correlation time of 3.1 ps estimated from $g^{(2)}(0)$ below the threshold. (b), (c) Two examples of the least square fitting of $g^{(2)}(\tau)$ vs. τ of two uncorrelated pulses, at $P/P_{th} = 0.67$ and 1, respectively. The dots are data; the solid lines are the fits using the measured IRF; the dashed lines are the convolution of two IRFs of the photon counter.

To evaluate the actual $g^{(2)}(0)$ from $\overline{g^{(2)}}(0)$, we need to know the functional form of $g^{(2)}(\tau)$ and the time resolution. Note that, for pulsed experiment, since $\overline{g^{(2)}}(0)$ depends on the convolution of the pulse, it is also largely determined by time resolution, or the pulse duration ΔT, and is insensitive to the actual shape of the pulse. Below we will approximate the emission pulse by an exponentially decaying pulse. In this way, a single parameter, the 1/e decay time, capture the time duration ΔT,

and an analytical relation between $g^{(2)}(0)$ and $\overline{g^{(2)}}(0)$ can be obtained. We have also checked that assuming a Gaussian (rather than exponential) pulse shape would alter our estimates of ΔT and $|g^{(2)}(0)-1|$ by only a few percents below or near threshold and no difference for $P > 1.16P_{th}$.

For a single-mode polariton lasers, the functional form of $g^{(2)}(\tau)$ is the same as that of a standard laser [75, 73]:

$$g^{(2)}(\tau) = 1 + \frac{n_s}{\bar{n}^2}\exp\left(-\frac{\bar{n}}{n_s+\bar{n}}\gamma\tau\right).$$

For an exponential pulse with $1/e$ decay time of ΔT, we have [76]:

$$\begin{aligned}\overline{g^{(2)}}(0) &= 1 + (g^{(2)}(0)-1)\frac{1}{\Delta T^2}\int_0^\infty\int_0^\infty \exp\left(\frac{x+y}{\Delta T}\right)\exp\left(\frac{-|x-y|}{\Delta T}\right)dxdy \\ &= 1 + (g^{(2)}(0)-1)\left(\frac{\tau_c}{\Delta T+\tau_c}\right). \end{aligned} \tag{3.8}$$

Here $\tau_c = 1/\gamma$ below threshold and $\tau_c = (n_s+\bar{n})/(\bar{n}\gamma)$ above threshold. Hence for our single-mode polariton laser, $g^{(2)}(0)$ can be obtained from $\overline{g^{(2)}}(0)$ given ΔT, γ and n_s.

To obtain ΔT, we note that:

$$\overline{g^{(2)}}(\tau + nT) \propto \int_{-T/2}^{T/2} I(t)I(\tau+t+nT)dt, \tag{3.9}$$

where n is an integer, T is the laser repetition period and $I(t)$ is the convolution of the emission pulse with the instrument response function, IRF(t): $I(t) = \int_{-\infty}^{\infty}\exp(-t_1/\Delta T)\mathrm{IRF}(\mathrm{t}-\mathrm{t}_1)dt_1$. We measured the IRF using a pulsed Ti:S laser with a 100 fs pulse duration. Then ΔT was obtained by a least-square fit of the data with Eq. 3.9 for $\Delta T > 4$ ps. The results are shown in Fig. S1(a) and examples of the fit are shown in Fig. S1(b) and (c). At $P > 1.16P_{th}$, $\Delta T < 4$ ps, and $\overline{g^{(2)}}(\tau)$

becomes indistinguishable from the convolution of the IRFs. In this regime, we take the conservative limit of $\Delta T = 4.2$ ps. It gives the upper bound of $|g^{(2)}(0) - 1|$, the deviation from the shot-noise limit.

To obtain γ, we use the known value of $g^{(2)}(0) = 2$ at well below threshold and compare it with $\overline{g^{(2)}}(0)$. Assuming $g^{(2)}(0) = 2$ at $P = 0.67P_{th}$ and using $\Delta T = 74.21$ ps (Fig. S1B), we find $\gamma = 0.31$ ps^{-1} using Eq. 3.8. This value is consistent with $\gamma = 0.29 \pm 0.04$ ps^{-1} from the $g^{(1)}$ fitting as will be discussed later.

Examples of the measured $\overline{g^{(2)}}(\tau)$ vs. τ are shown in Fig. 3.5(a) and (b). For both pulsed and CW excitations, bunching was evident below threshold but absent above threshold, showing the transition to a coherent state above threshold. The variation of $\overline{g^{(2)}}(0)$ with the normalized excitation power P/P_{th} was shown in Fig. 3.5(c). Using Eq. 3.8 with $\tau_c = 3.23$ ps and ΔT obtained above, we obtain the corrected $g^{(2)}(0)$ values as shown in the inset of 3.5(c). At $P > 1.16P_{th}$, with $\tau_c = 3.23$ ps and the conservative estimate of $\Delta T \leq 4.2$ ps, we obtain the upper bound of $g^{(2)}(0) - 1 \leq 2(\overline{g^{(2)}}(0) - 1)$.

A rapid transition from a thermal to coherent state was evident. Near P_{th}, where the ground-state occupation number $\bar{n}$ was small, bunching was measured with $\overline{g^{(2)}}(0)$ as high as 1.248 ± 0.007 under pulsed excitations, corresponding to $g^{(2)}(0) \sim 2$ after correcting for the time average. With the onset of quantum degeneracy and sharp increase of $\bar{n}$ with P, the intensity noise rapidly decreased toward the coherent limit. Between $2P_{th}$ and $6P_{th}$, with condensate occupation number $\bar{n} = 10^2 - 10^3$, the measured and corrected values of intensity noise remained around unity, with $0.994 \pm 0.006 \leq \overline{g^{(2)}}(0) \leq 1.009 \pm 0.005$ ($0.988 \pm 0.012 \leq g^{(2)}(0) \leq 1.020 \pm 0.011$), and the average intensity noise in this range was $\overline{g^{(2)}}(0) = 1.002 \pm 0.002$ ($g^{(2)}(0) = 1.004 \pm 0.004$). These results demonstrate the rapid formation of a coherent state with Poisson intensity noise in a polariton laser.

The experimental data were very well described by an analytical model for single-

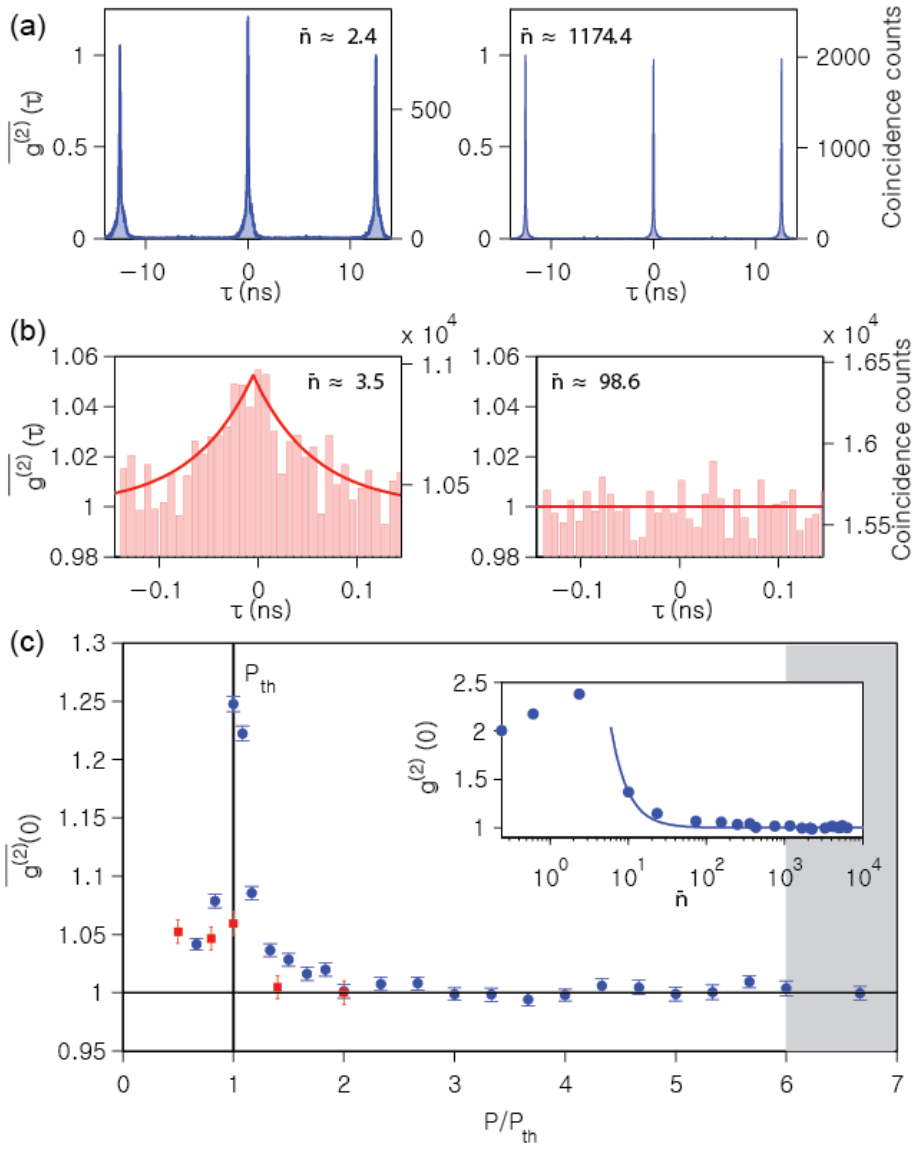

Figure 3.5: Second-order coherence properties of the single-mode polariton laser. (a) $\overline{g^{(2)}}(\tau)$ vs. τ below and above the threshold for pulsed excitation. (b) $\overline{g^{(2)}}(\tau)$ vs. τ below and above the threshold for CW excitation. (c) $\overline{g^{(2)}}(0)$ vs. P/P_{th} for pulsed (dots) and CW (rectangles) excitations. The error bars indicate statistical error of one standard deviation. The grey-shaded area shows where the polariton and photon lasing coexist. Inset: $g^{(2)}(0)$ vs. $\bar{n}$ of pulsed excitation corrected for the relaxation time of the ground state. The solid line shows a theoretical fit by Eq. (3.8), yielding $n_s = 37.3 \pm 0.9$.

mode matter-wave lasers [77, 78, 69, 73]. The model includes the interaction within the lasing mode, or in our system the self interaction among the condensed polaritons. It also includes other essential mechanisms of a laser: gain, gain saturation, and decay of the lasing mode. In the Bose-degenerate limit of $\bar{n} \gg 1$, $g^{(2)}(0)$ can be obtained as: [77, 73]:

$$g^{(2)}(0) = 1 + \frac{n_s}{\bar{n}^2} = 1 + \frac{\sigma_n^2 - \bar{n}}{\bar{n}^2}, \tag{3.10}$$

where n_s is the gain saturation number. Eq. (3.10) shows that the total number fluctuations in the condensate is $\sigma_n^2 = n_s + \bar{n}$; n_s represents fluctuations induced by the reservoir and other non-condensed modes, while $\bar{n}$ represents the intrinsic shot-noise of the condensate. The coherent limit is reached when $\bar{n} \gg \sqrt{n_s}$. Fitting our data with Eq. (3.10) gives $n_s = 37.3 \pm 0.9$, with $g^{(2)}(0) - 1 < 10^{-3}$ at $P > 2.5P_{th}$ (inset of Fig. 3.5(c)).

Our result is in sharp contrast to previous 2D polariton lasers. Previously, slow decrease of $g^{(2)}(0)$ with P toward a value above unity was commonly observed, suggesting large n_s. For example, in a 2D system featuring multiple localized lasing modes with long coherence times, $g^{(2)}(0) = 1.1$ was obtained for the selected lasing mode with $\bar{n} \sim 500$. Correspondingly, $n_s = 25,000 \gg \bar{n}$ dominates the intensity noise [69]. In other experiments, $g^{(2)}(0)$ was typically higher or could not be obtained accurately. Since a condensate population of $10^2 - 10^4$ was commonly reported when the transition to the weak-coupling regime takes place, a relatively small n_s as shown here is crucial for establishing intensity stability in a polariton laser.

The temporal phase coherence of a polariton laser is described by the first-order correlation function, $g^{(1)}(\tau)$. It is related to the power spectrum of the polariton emission by a Fourier transform. Using an intensity-stabilized CW laser for excitation, we measured $g^{(1)}(\tau)$ of the single-mode polariton laser using a Michelson interferometer. The visibility of the interference fringes gives $g^{(1)}(\tau)$ as the following. The intensity

distribution in Fig. 3.6(b) can be described by

$$I_{CCD}(x,\tau) = I_1(x) + I_2(x) + 2|g^{(1)}(\tau)| \times \sqrt{I_1(x)I_2(x)}cos(\frac{2\pi\theta}{\lambda_0}x + \phi), \quad (3.11)$$

where λ_0 is the wavelength of the lasing mode, ϕ, θ and τ are the phase difference, angle and time delay between the two interfering beams at given τ. $I_1(x)$ and $I_2(x)$ are the Gaussian intensity profile of the two beams, respectively, and are equal with $< 1\%$ difference in amplitude. Fitting the measured interference patterns with Eq. (3.11), we obtained $g^{(1)}(\tau)$ for each τ. Varying the excitation power, we obtained the power dependence of $g^{(1)}(\tau)$ vs. τ. $g^{(1)}(0) \geq 0.9$ was maintained throughout the experiments.

Examples of the interference fringes are shown in Fig. 3.6(a) and (b). We then obtain $g^{(1)}(\tau)$ vs. τ at different excitation powers by varying the delay time τ between the two arms of the interferometer.

Very different τ dependence of $g^{(1)}(\tau)$ was observed for the polariton laser as the condensate occupancy was increased. As show in Fig. 3.6(c), just above threshold, at a low condensate occupancy of $\bar{n} \sim 2.7$, $g^{(1)}(\tau)$ decays exponentially with τ (Fig. 3.6(c)), corresponding to a Lorentzian line shape. This confirms single-mode lasing and shows clearly that the intrinsic dephasing of the condensate dominates over external effects. As $\bar{n}$ increases, $g^{(1)}(\tau)$ changed to Gaussian decay, as is apparent in Fig. 3.6(d) for $\bar{n} = 968$. The coherence time also decreased. This can not be explained by multi-mode lasing or extrinsic effects, which were excluded by the exponential decay at small $\bar{n}$. It is also distinct from photon lasers, where exponential decay of $g^{(1)}(\tau)$ and Lorentzian spectrum persists in single-mode lasers.

The transition to a Gaussian decay of $g^{(1)}(\tau)$ can be described using the same single-mode matter-wave laser theory as used to describe the $g^{(2)}$ measurements. The

$g^{(1)}(\tau)$ of a matter-wave laser is given by [78, 73]:

$$
\begin{aligned}
|g^{(1)}(\tau)| =& \exp\Big(-\frac{4(n_s+\bar{n})u^2}{\bar{\gamma}^2}\big(\exp(-\bar{\gamma}\tau)+\bar{\gamma}\tau-1\big)\Big) \\
&\times \exp\Big(\frac{n_s+\bar{n}}{4\bar{n}^2}\big(\exp(-\bar{\gamma}\tau)-\bar{\gamma}\tau-1\big)\Big), \qquad (3.12)\\
\bar{\gamma} =& \frac{\bar{n}}{n_s+\bar{n}}\gamma.
\end{aligned}
$$

Here u is the polariton-polariton interaction constant and γ is the decay rate of the polariton ground state. This equation can be simplified in two limits corresponding to the weak and strong interaction regimes. To separate the two regimes, we define a total interaction strength $U = 4u\sqrt{\bar{n}}$. In the weak-interaction regime, $U \ll \gamma$, equation (3.12) is reduced to the Schawlow–Townes formula for a photon laser, $\exp(-\gamma\tau/2\bar{n})$, featuring an exponential decay (Fig. 3.6(c)). Correspondingly, the $1/e$ coherence time increases linearly with the occupation number of the lasing mode, $\tau_c = 2\bar{n}/\gamma$. In the strong-interaction regime, $U \gg \gamma$, equation (3.12) is approximated by $\exp(-2\bar{n}u^2\tau^2)$, featuring a Gaussian decay, as we observed (Fig. 3.6(d)). Correspondingly, $\tau_c \propto 1/U \propto 1/\sqrt{\bar{n}}$. Therefore polariton-polariton interactions and the shot noise of the condensate lead to a Gaussian broadening or dephasing of the polariton laser.

Using Eq. (3.12) to fit the $g^{(1)}(\tau)$ data at different $\bar{n}$, we can obtain the main parameters governing the dynamics of the polariton laser, n_s, γ and u. The best fit yields $n_s = 61 \pm 13$, $\gamma = 0.29 \pm 0.04$ ps^{-1} and $u = (2.2 \pm 0.2) \times 10^{-3}$ ps^{-1}. n_s is similar to the estimate obtained from pulsed $g^{(2)}$ measurements, 37.3. The difference may be due to different excitation conditions, CW vs. pulsed, which may lead to different densities and effective temperatures of the reservoir. γ is within a reasonable range. From u we estimated the system size-independent interaction constant $uA_{\text{cond}} = 4\ \mu\text{eV}\cdot\mu\text{m}^2$, which is in excellent agreement with the previously reported theoretical and experimental values [36]. Here $A_{\text{cond}} \sim 2.5\ \mu\text{m}^2$ is the size

of the condensate measured from spatial PL imaging (see the inset of Fig. 3.1 for an example). It was independent of the pump power as expected, since it was determined by the effective confinement potential in 0D systems. This confirms that strong polariton-polariton interaction u could be achieved in our system due to the tight lateral confinement or small A_{cond}.

Figure 3.6(e) compares τ_c from the fit with experimental values with respect to $\bar{n}$. For small $\bar{n}$, τ_c increases sharply with $\bar{n}$, as expected from the Schawlow-Townes formula. However, τ_c starts to decrease because polariton-polariton scattering leads to the phase decoherence of the lasing mode. The crossover between the weak and strong interaction regimes corresponds to where $U \sim \gamma$, as illustrated in the inset of Fig. 3.6(e).

We note that, although linewidth broadening has been observed in polariton lasers before, contribution by the condensate nonlinearity was negligible. Typically the linewidth broadening was accompanied by an increase in the intensity noise [79, 80], and thus could be understood as the effect of mode competition. When a single, localized mode was selected, the coherence time saturated above threshold and became independent of the ground state occupancy [69]; the coherence time was mainly limited by energy shift resulting from reservoir-induced thermal fluctuations represented by $n_s \gg \bar{n}$. Here, however, the intensity noise remained at the shot-noise limit and thus multi-mode lasing or reservoir induced fluctuations were both negligible. $g^{(1)}(\tau)$ showed strong dependence on the condensate population. Therefore, the Gaussian dephasing we observed directly resulted from interactions within the condensed polaritons.

We also note that dephasing in the condensate may also be induced by thermal fluctuations of the reservoir population [69, 81]. However, this effect would not explain the fast decrease of the coherence time above $2P_{th}$, and thus was expected to be much weaker compared to the condensates contribution. As shown in Fig. 2(e), the energy

shift vs. excitation density, $d\Delta E/dP$, between $2-12P_{th}$ was slowed down to 1/10 of that below threshold. Therefore the energy fluctuation due to reservoir population fluctuation would change by $\ll\sqrt{6}$ between $2-12P_{th}$, which is in direct contradiction to the observed 6-fold decrease of the coherence time in this range.

The reason the reservoir-induced fluctuation was weak could be many-fold. First of all, while the energy shift is proportional to the population N, the energy fluctuation is proportional to $\sqrt{N}/A$, where A is the system area. In our system, there was no lateral confinement in the QWs and the excitons can freely diffuse. A typical diffusion length [44] gives a spatial extend of about 100 μm^2. In contrast, the polaritons were tightly confined; their spatial extend was determined by the ground-state wavefunction and measured to be 2.5 μm^2 for all excitation densities. Hence, the energy fluctuation introduced by an unconfined exciton population is attenuated by 1600 times compared to a confined one. At an exciton density of $0.1n_{sat}$, for a saturation density $n_{sat}=4\times10^{10}$ cm^{-2} per QW [82], the exciton has a total population of about 4.8×10^4, which introduces an energy fluctuation equivalent to that by about 30 condensate polaritons near zero detuning, while the condensate population quickly built up to 10^2-10^3 above threshold. Moreover, it would be interesting to investigate if the coherent condensate interacts within itself more strongly than with the thermal reservoir, and if the reservoir fluctuation induced dephasing may become suppressed when the coherent condensate is formed [83]. These issues could be clarified in future investigations with more careful calibration of the exciton density or exciton interaction strength.

3.2.3 Multi-mode Polariton Lasing

For multi-mode polariton lasing, we positioned an excitation laser at the side of the 0D device to maximize the spatial overlap between the pump spot and the excited-state wavefunction until we find coexistence of ground-state and excited-state lasing

as shown in Fig. 3.7.

Multi-mode polariton lasing is common in 2D microcavities. The purpose of this experiment is to show the effect of mode competition on $g^{(2)}(0)$ in a multi-mode polariton laser. We established two-mode lasing in the same system under the same experimental conditions except for moving the excitation laser spot from the center of the device to slightly off-center, to increase its overlap with the first excited state of the polariton modes [2] as shown in Fig. 3.7. The input-output relationships of both lasing modes are shown in Fig. 3.8(a). Contrary to a single-mode laser, clear deviations of $g^{(2)}(0)$ from the unity were observed for both the ground and first-excited state, with $\overline{g_{00}^{(2)}}(0)$ ($g_{00}^{(2)}(0)$) = 1.023$\pm$0.009 (1.048$\pm$0.019) and $\overline{g_{11}^{(2)}}(0)$ ($g_{11}^{(2)}(0)$) = 1.027$\pm$0.009 (1.057$\pm$0.019), respectively (Fig. 3.8(b)). The increased intensity fluctuations can be explained by the stochastic relaxation of polaritons from a common reservoir into the lasing modes [84]. Consistent with this explanation, we measured strong anti-correlation between the two modes as shown by a cross-correlation function $\overline{g_{12}^{(2)}}(0) < 1$. Again, I'd like to emphasize that such mode competition is difficult to eliminate in 2D or quasi-2D systems, because the linewidth of the lasing mode is typically larger or comparable to the energy separation between LP modes of different polarizations, of different momenta, or in different localization potentials. Our results show that single-mode lasing, achieved by both tight lateral confinement and polarization selectivity in our system, is crucial for intensity stability of a polariton laser.

To further analyze the experimental results, Langevin equations in the presence of the ground state, first-excited state, and exciton reservoir were solved numerically. The equations for the numerical analysis are shown as below.

$$\frac{d\psi_1}{dt} = \frac{1}{2}(-\Gamma_1 - \gamma_1(|\psi_g|^2 + 1) + \gamma N_R) + \theta_1(t)$$
$$\frac{d\psi_g}{dt} = \frac{1}{2}(-\Gamma_g + \gamma_1|\psi_1|^2 + \gamma N_R) + \theta_{g,R}(t) + \theta_{g,1}(t)$$
$$\frac{dN_R}{dt} = P - \Gamma_R N_R - \gamma N_R(|\psi_g|^2 + 1) - \gamma N_R(|\psi_1|^2 + 1)$$

Here ψ_1, ψ_g are the order parameters of the condensate of first-excited state and ground state, respectively. N_R is the reservoir population. Γ describes decay rate of each state and γ describes stimulated scattering process. P is the pump strength. θ is Langevin noise during relaxation dynamics, reservoir to ground state, reservoir to first-excited state, and first-excited state to ground state.

Figure 3.9 shows simulation results for multi-mode lasing. Dashed lines in Fig. 3.9(b) indicate auto- and cross-correlation for single mode lasing for comparison with multi-mode case. It is clear that the intensity fluctuation of lasing modes increases compared to that of single-mode lasing and mode-competition is shown from cross-correlation.

3.3 Optimizing Coherence of Polariton Laser

Lastly, let me discuss how one can optimize coherence properties of polariton lasers. For $g^{(2)}(0)$, as we approach to the 2D limit, it would start degrading at a point where the energy difference between ground and first-excited states becomes small enough or multiple condensates coexists due to defects. For phase coherence, the coherence time, or linewidth, should increase initially as the device size increases because the polariton-polariton interaction strength decreases, which is determined by the material dependent interaction strength divided by the spatial size of polariton lasing mode. Upon approaching 2D limit, the coherence time should then start decreasing as the intensity noise increases. Therefore, there must be a polariton laser

with optimal coherence properties, which maintains high degree of intensity coherence and phase coherence time, as we vary the device size, or spatial size of the lasing mode. Not surprisingly, size-dependent $g^{(2)}(0)$ has recently been shown [85].

To realize this, one might simply think it will be very straightforward to make such devices with varying size. However, as it turned out, it is difficult to achieve in HCG based microcavities. This is because air-suspended HCG bends when the sacrificial layer is removed due to strain release which will be discussed later in details. This bending highly depends on the the length of the grating bars and significantly alter exciton-photon detunings for different sizes. To overcome this, we developed MHCGs, which are very robust and fully monolithic but at the same time keeps the same properties as HCGs such as single-polarization lasing. Therefore, MHCG microcavities were used for the experiment.

Figure 3.10 shows a few of the fabricated devices with different sizes taken by SEM. The PL measurements were performed in these devices. I used 30 um diameter pump spot size to cover all the different devices. Figure 3.11 shows the PL images of emission spectra of devices with different sizes near the lasing threshold. As the size increases, the discretization of the polariton states diminishes, which in theory would increase intensity fluctuation when the energy difference between ground and first-excited states becomes close to their linewidths.

We investigated device-size dependent $g^{(1)}(\tau)$ and $g^{(2)}(0)$ using the same technique used for 0D HCG microcavities. As the device sizes get larger, it was difficult to fully achieve spatially homogeneous lasing state and multi-mode lasing states sometimes occurred. I repeated multiple experiments and found the best results (based on the coherence time) for different device sizes. The results on the coherence time is shown in Fig. 3.12(a). For device size of 8 μm, close to 300-fold increase in the coherence time compared to its lifetime (estimated from the linewidth using low pump power). Fig. 3.12(b) shows size and power dependent $g^{(2)}(0)$. The values for different devices

were taken from the highest power used for $g^{(2)}(0)$ measurements. The measured $\overline{g^{(2)}}(0)$ stays relatively close to a coherent limit for most of the devices. However, one can see a trend of increase of $\overline{g^{(2)}}(0)$ as the device size increases.

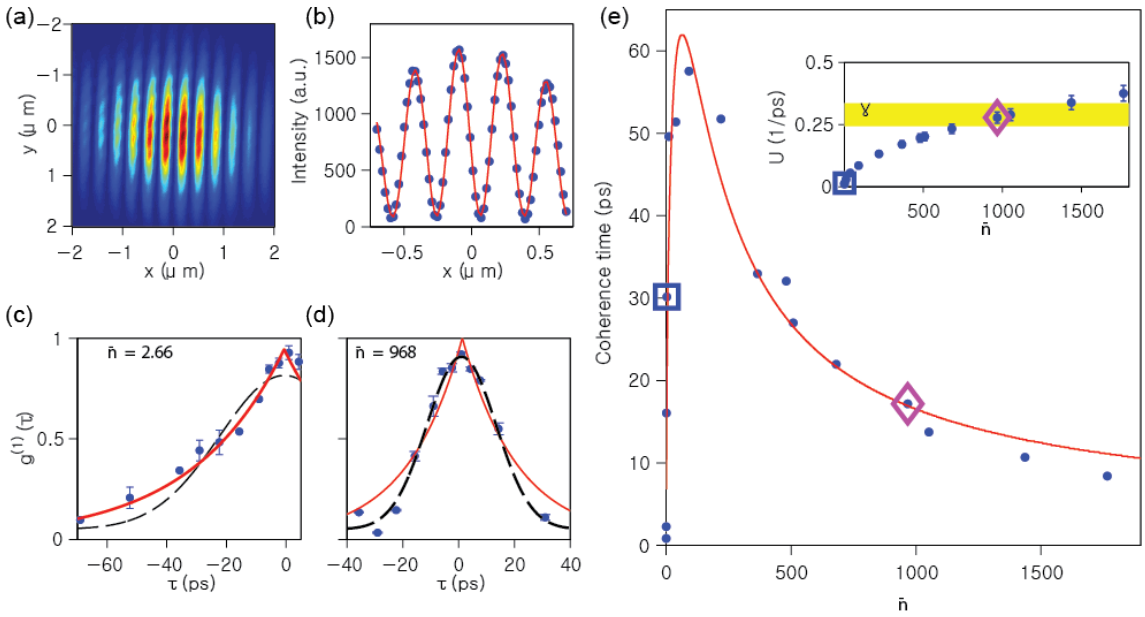

Figure 3.6: First-order coherence properties of the single-mode polariton laser. (a) A spatial interference image of the polariton laser at zero time delay. (b) The interference fringe along x-axis obtained from (a) by integration along the y-axis. The dots are data and the solid line is a fit by equation (3.11) with $g^{(1)}(0) = 0.94$. (c), (d) The measured $g^{(1)}(\tau)$ vs. τ (dots), exponential fits (red solid lines), and Gaussian fits (black dashed lines), for $\bar{n} = 2.66$ and 968, respectively. (e) The phase coherence time τ_c of the polariton laser vs. $\bar{n}$. The dots are taken from the measured $g^{(1)}(\tau)$ for each value of $\bar{n}$. The line is calculated from Eq. (3.12) using the fitted parameters. Inset: Comparison between the interaction energy U (dots) and decay rate γ (yellow shaded region) of the condensate vs. $\bar{n}$. The error bars and thickness of the shaded area are determined by fitting errors with a 95% confidence interval. The rectangle and diamond marks respresent $\bar{n} = 2.66$ and $\bar{n} = 968$, respectively.

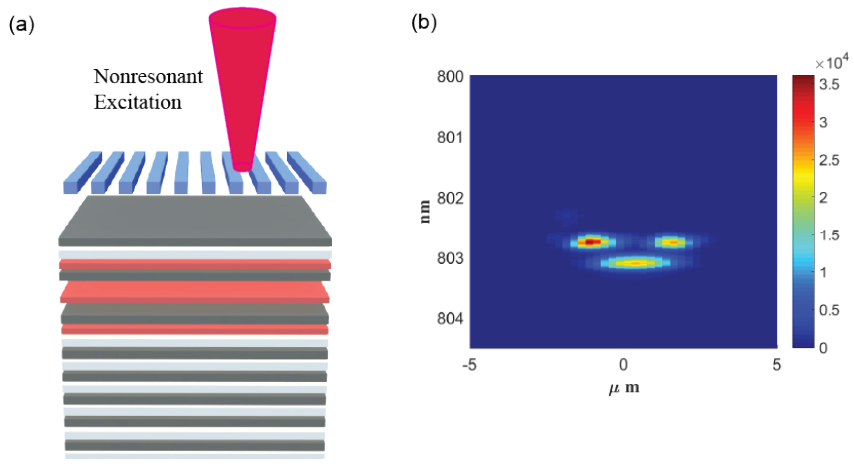

Figure 3.7: Pump position for multi-mode lasing. (a) Pump spot is focused at the side of the device. (b) Spectrum above the lasing threshold.

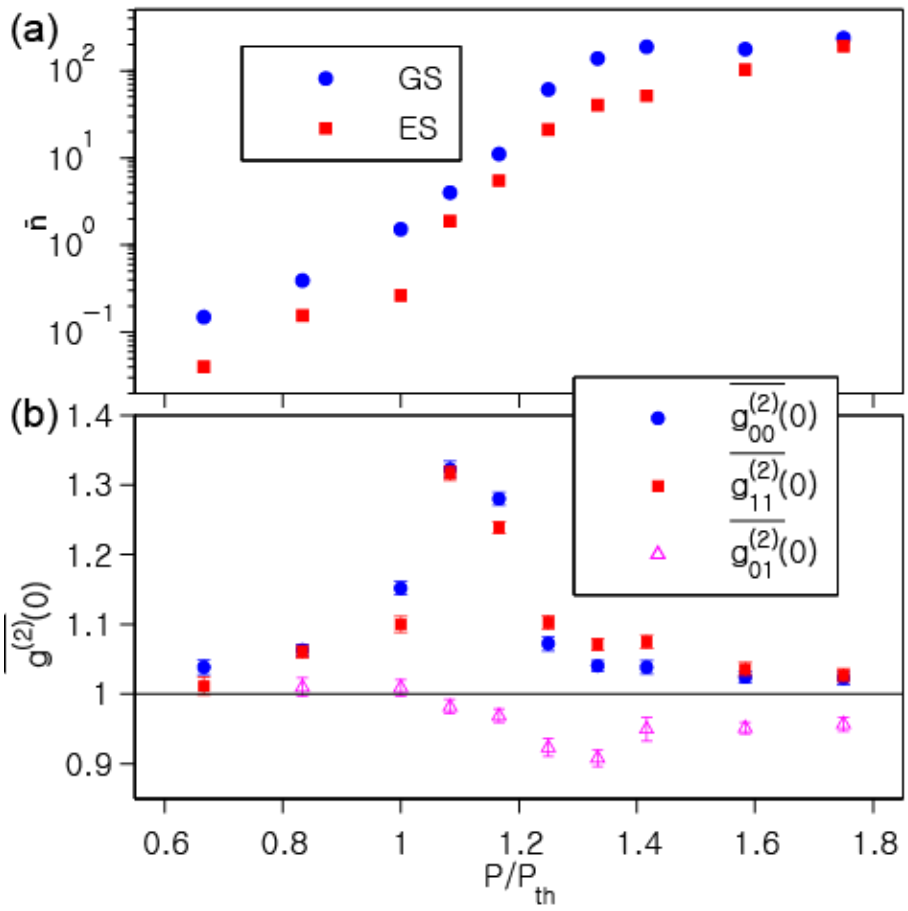

Figure 3.8: Second-order correlations of the two-mode polariton laser. (a) The occupation numbers of the ground state (dots) the excited state (squares) vs. P/P_{th}. GS: Ground state, ES: First excited state. (b) $\overline{g^{(2)}}(0)$ vs. P/P_{th}. $\overline{g_{00}^{(2)}}(0)$: auto-correlation of GS, $\overline{g_{11}^{(2)}}(0)$: auto-correlation of ES, and $\overline{g_{01}^{(2)}}(0)$: cross-correlation between GS and ES.

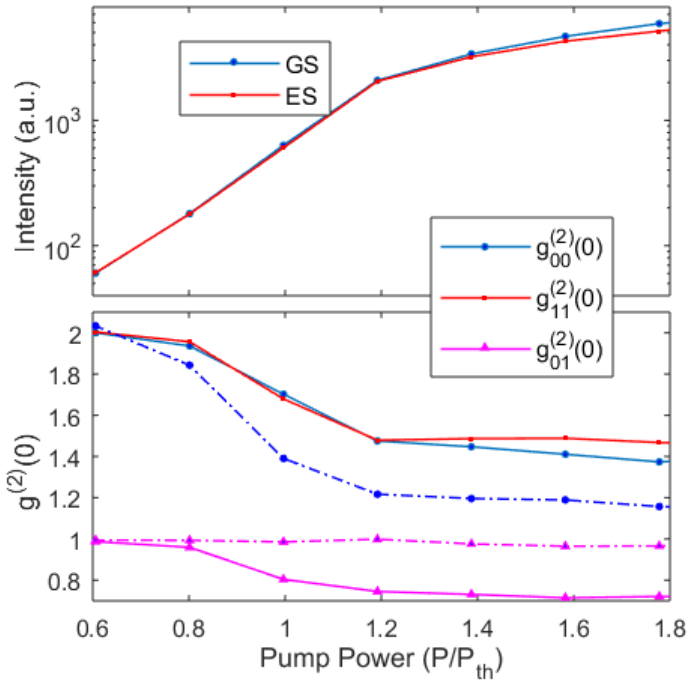

Figure 3.9: Numerical simulation of second-order correlations of the two-mode polariton laser. Dashed line is simulated second-order correlation of the single-mode laser which shows much faster decrease of $g^{(2)}(0)$.

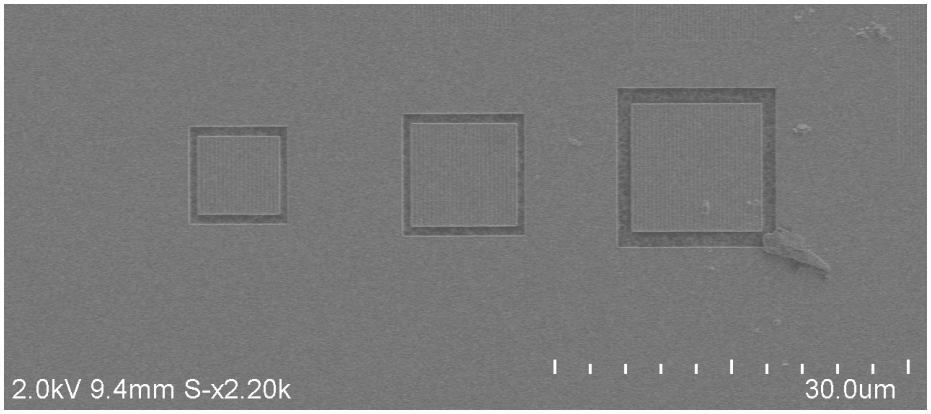

Figure 3.10: SEM top view of fabricated devices with different size

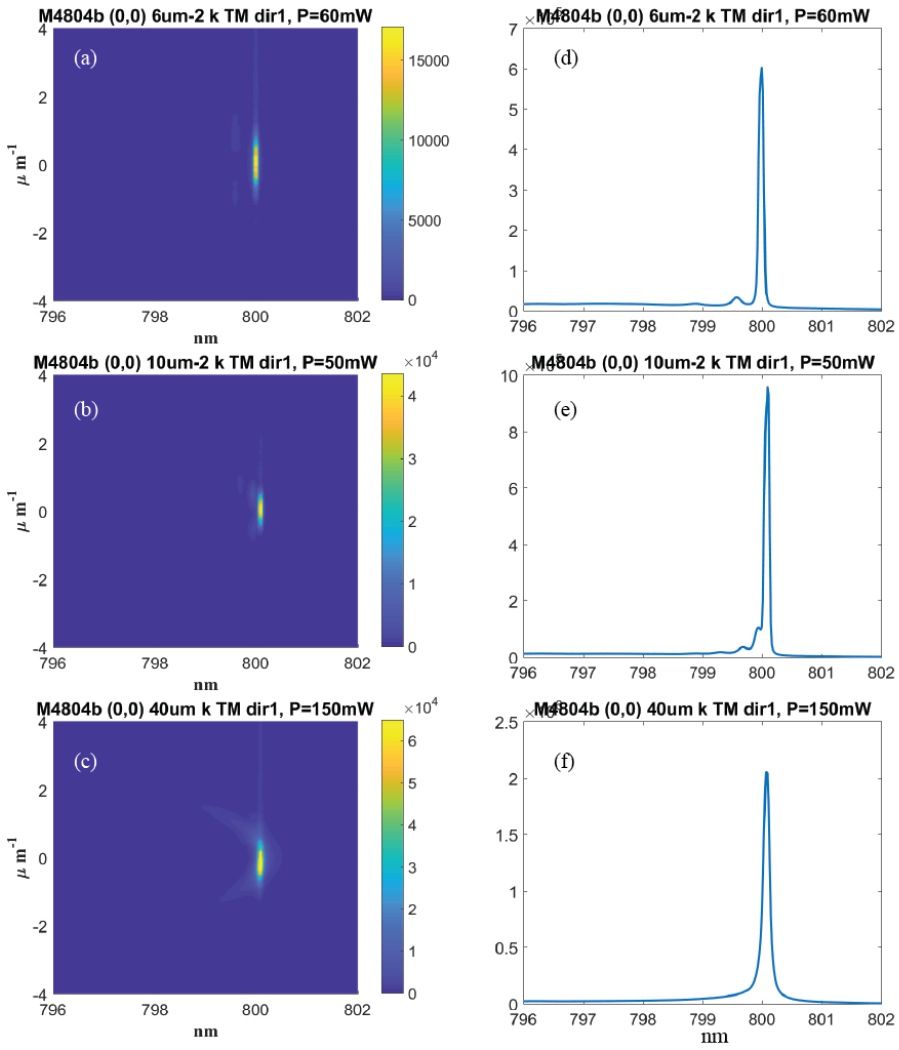

Figure 3.11: PL spectrum of fabricated devices near the lasing threshold. (a), (d) 6 μm. (b), (e) 10 μm. (c), (f) 40 μm

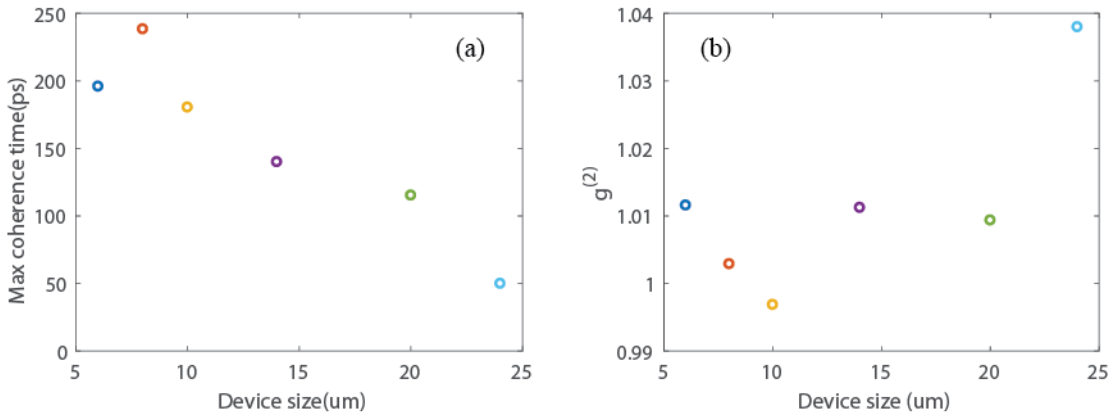

Figure 3.12: Size dependent coherence time and $g^{(2)}(0)$. (a) Measured maximum coherence time for different size of devices. (b) Measured $g^{(2)}(0)$ for different size of devices. The value for each device is taken at the highest laser intensity.

CHAPTER IV

Optical Frequency Comb Generation in Coupled Microcavities

Coupled nonlinear oscillators have been used to model a variety of systems ranging from biology to laser physics. They show rich dynamics of fixed state, stable limit-cycle oscillations, and chaos through bifurcations. When the uncoupled oscillator has frequency f, limit cycles with frequency Δf can lead to equidistant frequencies of $f + N\Delta f$, where N is an integer. This new possible mechanism for frequency comb generation has been discussed in exciton-polariton systems and lumped-element circuit QED systems [57, 86].

In this chapter, I'll present matter-wave frequency comb generation in coupled exciton-polariton condensates [57]. The interplay between the nonlinear polariton interaction and complex inter-cavity coupling leads to time-periodic modulation of the amplitudes and phases of the polariton condensates, forming a polariton frequency comb. Equidistant spectral lines are observed in photoluminescence and the first-order temporal coherence. The line spacing is determined by the interaction and coupling strengths, not by the cavity's free spectral range unlike toroidal microcavities or quantum cascade lasers. This new mechanism of comb generation allows non-resonant excitation with a power input much below the conventional semiconductor laser threshold. The comb line spacing is adjustable up to multi-terahertz frequency

for a chip-scale low power terahertz source. The work may open a door to new phenomena and device applications of strongly nonlinear, coupled cavities.

4.1 Driven-Dissipative Coupled Polariton Equation

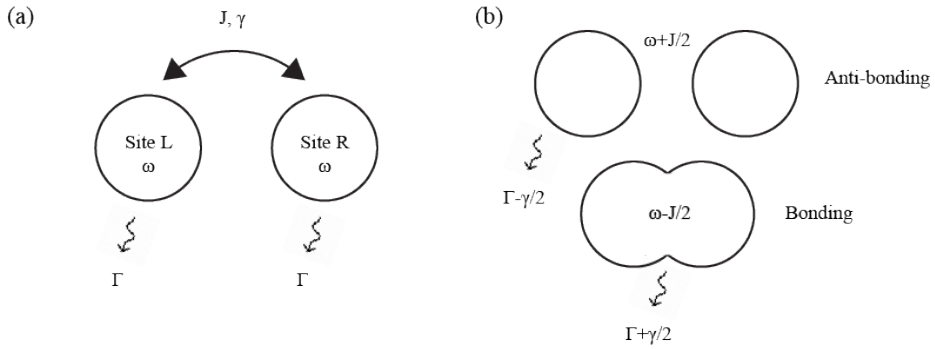

Figure 4.1: Two-coupled polariton condensates. (a) Two condensates with the same energy (ω) and decay rate (γ) coupled through coherent (J) and dissipative couplings (Γ). (b) Coupled states with energies splitted by coherent coupling strength and decay rates of $\Gamma - \gamma/2$ and $\Gamma + \gamma/2$.

In this section, I will discuss a system of coupled polariton condensates and parameter space which the stable limit cycles appear theoretically. Two-coupled condensate centers are considered as shown in Fig. 4.1.

When two polariton condensates are trapped close to each other, photon tunneling between them leads to Josephson coupling, resulting in the formation of bonding (B) and anti-bonding (A) states with split energies. Correspondingly, the radiation loss of the system is also modified, which can be described as dissipative coupling between the condensates, leading to different dissipation rates of the coupled states. The dissipation rate is higher (lower) when the two condensates are in-phase (out of phase) and emission from the condensates interfere constructively (destructively). Consequently, the total coupling becomes non-Hermitian.

The dynamics of such a coupled polariton system can be described by the driven-

dissipative coupled polariton equation [57, 87]:

$$\frac{d\psi_{L,R}}{dt} = \frac{1}{2}(p_{L,R}\psi_{L,R} - \gamma\psi_{R,L} - \mu|\psi_{L,R}|^2\psi_{L,R}) - \frac{i}{2}(2\omega_{L,R}\psi_{L,R} - J\psi_{R,L} + \alpha|\psi_{L,R}|^2\psi_{L,R}). \tag{4.1}$$

Here $\psi_{L,R}$ is the order parameter of the condensate in each site, $\omega_{L,R}$ are the frequencies of the uncoupled cavity modes, $p_{L,R} = P_{L,R} - \Gamma$ where $P_{L,R}$ is the incoherent pump strength acting on site L,R and Γ is the cavity decay rate, γ is the dissipative coupling strength, μ is the gain saturation parameter, J is the Josephson coupling strength, and α is the on-site interaction strength. With a relatively strong on-site interaction and weak Josephson coupling (Fig. 4.2(a)), as P is varied, stable fixed-point and limit-cycle solutions, or a comb state, can exist between weak lasing in the anti-symmetrically coupled state and lasing in the symmetrically coupled state.

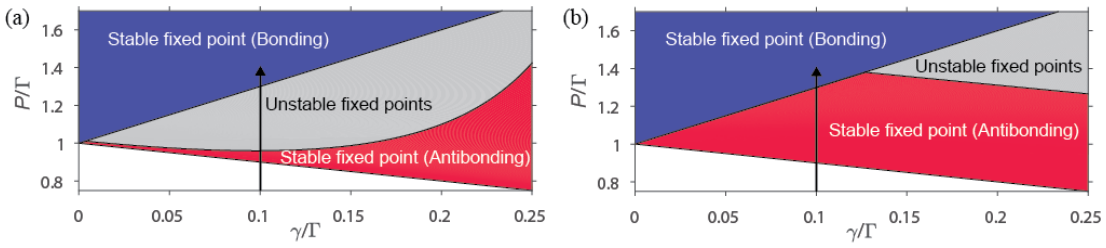

Figure 4.2: Bifurcation diagram for coupled polariton equation. (a), (b) Bifrucation diagram in $P-\gamma$ parameter space for $J/\Gamma = 0.07$, 2.5, respectively. Other parameters are $\alpha/\Gamma = 0.25$, $\mu/\Gamma = 0.05$ for both diagrams. A standard lasing threshold is when $P = \Gamma$ in the absence of dissipative coupling. For certain values of $\gamma > 0$, thresholds for stable and unstable fixed-point solutions emerge as P increases, indicated by arrows for $\gamma/\Gamma = 0.1$.

Bifurcation diagrams for two parameter spaces are illustrated in Fig. 4.2(a),(b). The steady lasing states become unstable in the vicinity of condensation threshold and a limit-cycle solution emerges by critical Hopf bifurcation from the unstable single-mode lasing states [57], manifested as a polariton frequency comb with equidistantly spaced spectral lines. For large J/Γ (Fig. 4.2(b)), the unstable fixed-point domain in the parameter space becomes small and requires large γ which may be difficult to

realize. To realize the polariton comb, therefore, it is not always desirable to have a very high cavity quality factor, which increases J/Γ.

To identify bifurcation thresholds, it is convenient to express the equation 4.1 based on a pseudospin vector defined as $\mathbf{S} = \frac{1}{2}(\mathbf{\Psi}^\dagger \cdot \boldsymbol{\sigma} \cdot \mathbf{\Psi})$, where $\mathbf{\Psi} = (\psi_1, \psi_2)^T$ and $\boldsymbol{\sigma}$ is the Pauli vector.

$$\begin{aligned}
\frac{dS_x}{dt} &= (p - \mu S)S_x - \gamma S - \alpha S_z S_y \\
\frac{dS_y}{dt} &= (p - \mu S)S_y + JS_z + \alpha S_z S_x \\
\frac{dS_z}{dt} &= (p - 2\mu S)S_z - JS_y \\
\frac{dS}{dt} &= (p - \mu S)S - \mu S_z^2 - \gamma S_x
\end{aligned}$$

where $S_x = \frac{1}{2}(\psi_2^*\psi_1 + \psi_1^*\psi_2)$, $S_y = \frac{i}{2}(\psi_2^*\psi_1 - \psi_1^*\psi_2)$, $S_z = \frac{1}{2}(|\psi_1|^2 - |\psi_2|^2)$, $S = \frac{1}{2}(|\psi_1|^2 + |\psi_2|^2)$. Then the nontrivial fixed point A state becomes stable when $p = -\gamma$ and $S_x = -S$, $S_y = S_z = 0$, $S = (\gamma + p)/\mu$. This becomes unstable by pitchfork bifurcation when $p = -\gamma + \frac{\eta(\gamma^2+J^2)}{\alpha J - \eta\gamma}$. From this threshold until the stable bonding threshold, stable limit-cycle solutions exist and both B and A states are unstable. The threshold for the stable fixed point B state is when $p = 3\gamma$ and $S_x = S$ by the Hopf bifurcation.

4.2 Realization of two-coupled condensates in HCG microcavities

In this section, an experimental realization of coupled condensates is presented. Polariton energy is determined by the exciton-photon detuning. If one can modulate spatial detuning landscape through either exciton energy or photon energy, it would be possible to manipulate, trap polariton through a potential created by detuning change. Air-suspended HCG bends, this directly changes the length of the microcavity

and thus photon energy.

The reason for this bending is because of built-in strain release when the second layer is removed. The initial strain is from the lattice mismatch between the grating layer and the sacrificial layer. By placing strain-release patterns surrounding the HCG structure, we were able to engineer the level of bending spatially by strain-release pattern design. This is confirmed by both experiment using atomic force microscopy (AFM), 3D optical microscopy and finite element simulation using COMSOL Multiphysics.

4.2.1 Experimental Measurements of HCG Bending

Experimental measurements of HCG bending were performed by AFM and laser scanning confocal microscopy (LSCM). Both methods have advantages and disadvantages. AFM has a very good resolution in every dimension. However, due to the fragile nature of our samples, limited AFM tips and modes were used and resolutions were limited as a result. AFM was measured with the 0D HCG devices in non-contact tapping mode (Fig. 4.3).

The bending was measured as large as about 100 nm which may result in a cavity resonance shift of about 10 nm. Another feature is that the bending is highest at the center of the device. Notice that the edge of the device, there are L-shaped strain-release patterns. It is also clear that in the tapping-mode the grating bars are not well resolved and also height measurements are quite noisy. Also, the measurements took too long to investigate many number of devices with different types of release patterns and study in a systematic way.

The optical technique using LSCM is fast and high-resolution. The problem was the grating is in deep subwavelength regime so the optical beam may not resolve the grating bars individually (which is the case under common lamp-based microscope). This is illustrated in Fig. 4.4 showing the discontinuity in height measurements. For

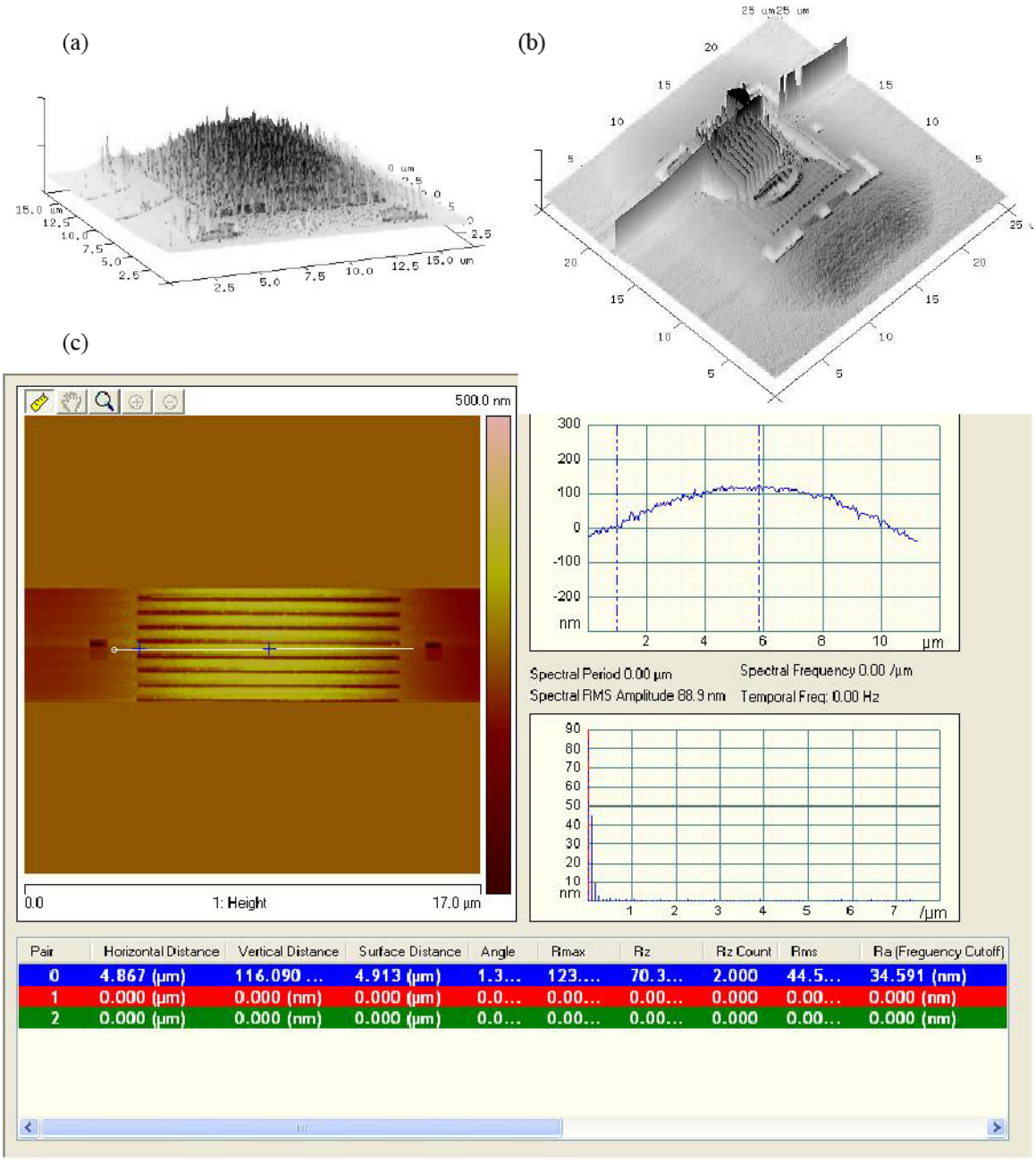

Figure 4.3: AFM images of square HCG. (a), (b) Side views of AFM images of the HCG showing upward bends of the suspended structure. (c) Top view of the HCG bending image. Line cut indicates that a grating bar bends more than 100 nm.

this reason, we designed and fabricated test samples with larger periods (1.4 μm, about three times larger than HCG for microcavities) for them to be easily resolved by LSCM. A few examples of the test devices are shown in Fig. 4.5(a). The main tests are (1) the bending with and without release patterns (2) the bending with release patterns on both sides and one side of the grating (3) the bending as the distance of the release pattern from the grating structure (4) the grating bar length dependent bending.

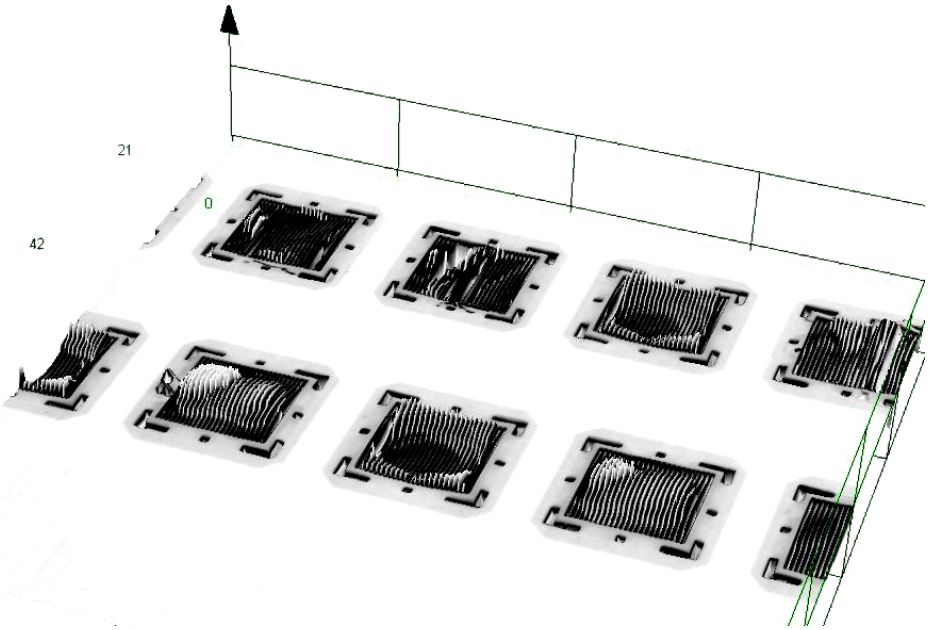

Figure 4.4: Discontinuity of LCSM measurements for sub-wavelength gratings.

The measured bending is shown in Fig. 4.5. Let me first compare the devices with and without release patterns (Fig. 4.5(b)). Without release patterns, the grating bar bends more toward the center. This makes sense since the strain can't be released to the bulk side but rather to the other side toward the bar center. When the release patters are present, the strain releases more regularly throughout the grating bar and the grating bar is measured to be more straight. When only single release pattern is used, the strain releases toward the bar with release pattern making it more bend and the bar height converges to the bulk height to the side where no release pattern

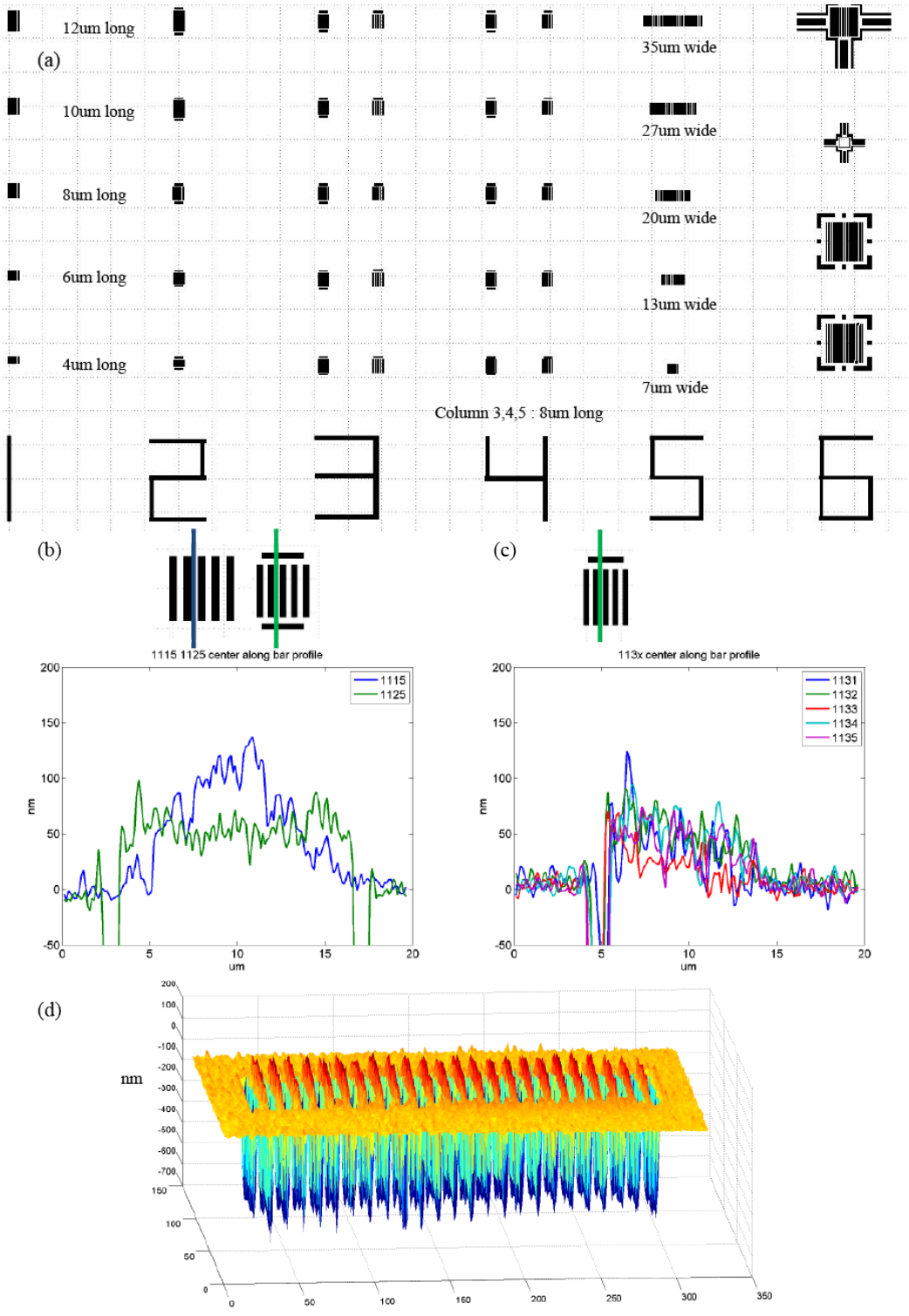

Figure 4.5: LCSM measurement results. (a) Test grating designs. (b) Test designs and results for the grating with and without strain release patterns on both sides. (c) Test design and result for the grating with strain release pattern on one side. (d) Bending measurements for one dimensional grating structure.

is (Fig. 4.5(c)). Also, bending with long lateral size is shown in Fig. 4.5(d) which shows less effect in the device dimension across the grating bar. It is shown that the lateral dimension (across the grating bar) has very small effect in grating bending.

4.2.2 HCG Bending Simulation

To understand the experiment with the test designs, the mechanical bending simulation was performed by COMSOL Multiphysics. 3D device structure is constructed by AutoCAD (Fig. 4.6) and imported to the COMSOL.

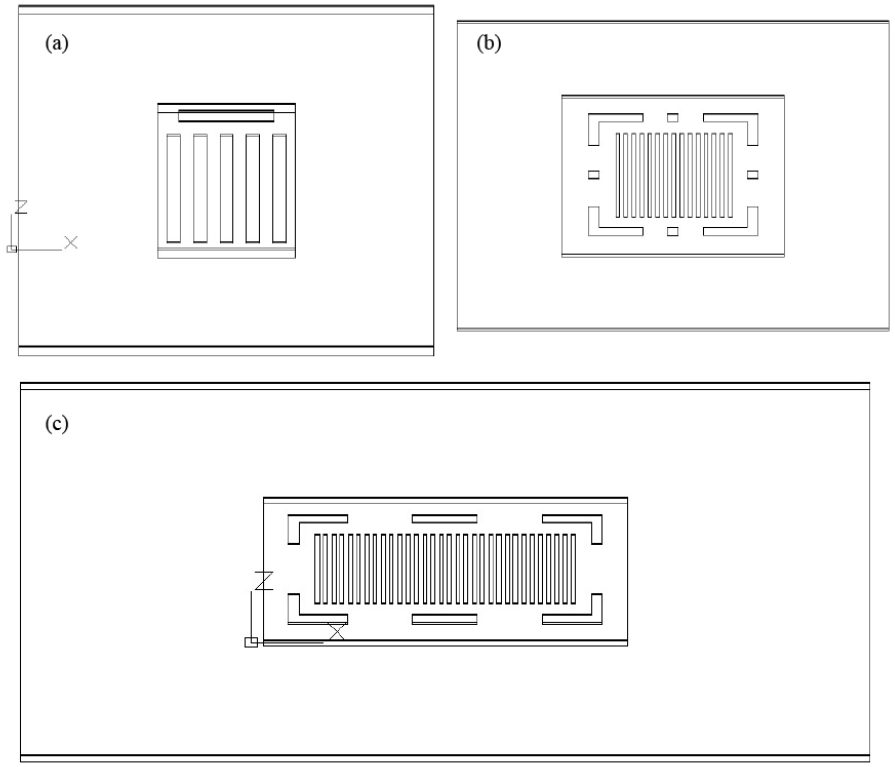

Figure 4.6: Drawing of HCG devices by AutoCAD. (a) Gratings with a single-side release pattern. (b) Square grating. (c) Two-coupled grating.

The initial strain is set considering the lattice mismatch between the grating and the sacrificial layers. The simulation results are in good agreement with the optical measurements of HCG test devices (Fig. 4.7).

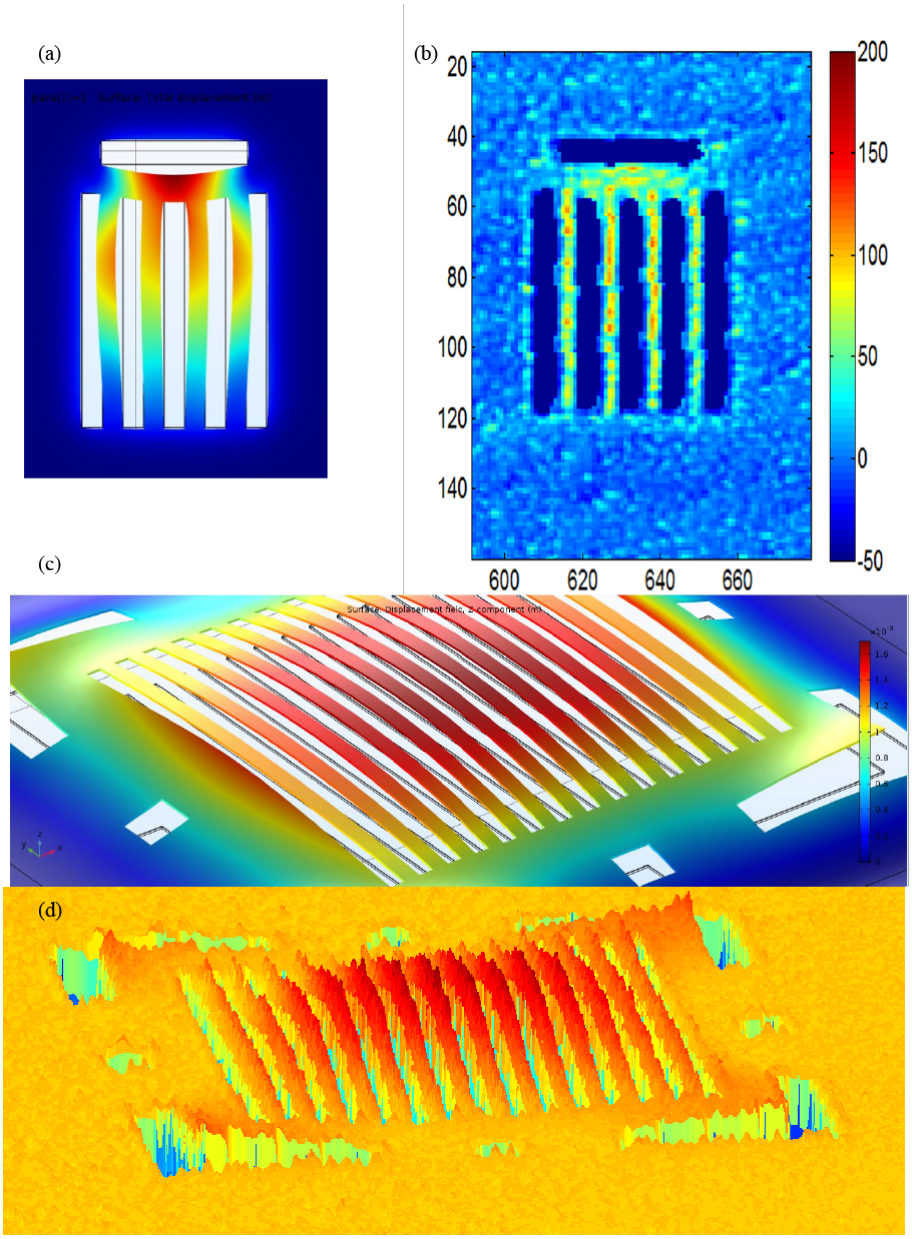

Figure 4.7: Comparison between COMSOL simulation and LCSM measurements. (a), (b) Simulated and measured results for single-side release pattern. (c), (d) Simulated and measured results for square grating structure.

4.2.3 Realization of two-coupled HCG microcavities

We now fabricated two-coupled microcavities via bending engineering. The design is shown in Fig. 4.8(a). Confinement and coupling of sites are controlled by both the lateral size and placements of the grating bars and the tethering pattern surrounding the HCG. The simulation results are shown in Fig. 4.8(a). Controlling the location and shape of the tethering patterns, as discussed earlier, controls both the height and width of the potential barrier between two sites. This tunability allows us to tune the three key cavity parameters that govern the many-body states of the system – the Josephson coupling strength J, dissipative coupling strength γ, and on-site interaction strength α.

Figure 4.8(b) and (c) show the R-space and K-space PL spectra of the polaritons at low pump powers. The states are discretized due to tight confinement, which also enhances the on-site interaction to on the order of 10 μeV due to increased polariton density [37]. Bonding (B) and anti-bonding (A) states are formed due to Josephson coupling. Their separation gives the coupling strength $J = 0.5$ meV. The Josephson coupling decreases as the pump power increases because the pump spot is located at the center of the device where the potential barrier is. The distance between the two minima of the effective potential is 6.4 μm, corresponding to the separation of the two cavity sites. The next lowest energy state, labeled as state E in Figure 4.8, is formed from the first excited state of each uncoupled site at 1.4 meV above state A.

4.3 Excitation power-dependent spectrum

The transitions through the limit-cycle regime, as expected from equation 4.1, are clearly observed in the power dependence of the real-space spectra (Fig. 4.9). The PL spectrum at the low power (Fig. 4.8(b),(c) shows that the bonding state B initially has a larger population than the state A, because the pump spot is placed at the

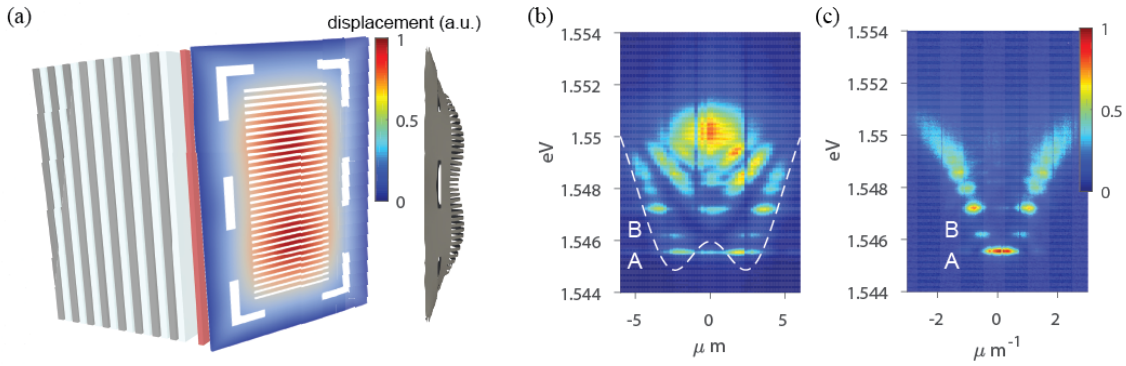

Figure 4.8: Sample properties at low excitation powers. (a) A schematic of the sample structure with a bent SWG mirror. Bending of the SWG is simulated by COMSOL and shown both by the color map in the schematic view and in the side view. The bending is less where there are open slots in the tethering pattern and vice versa. (b) The real-space photoluminescence (PL) spectrum of the coupled polariton system showing the discrete polariton states at low excitation powers. The ground state is formed by the bonding state (B state), while the first excited state is the anti-bonding state (A state). The white dashed line illustrates the potential due to the bending of the SWG shown in (a). (c) The corresponding Fourier space spectrum showing the B state at $k = 0$ and the A state at $k = \pm\pi/a$, where a is the distance between the two coupled sites.

center of the device and prefers the B state.

As the pump power increases, the anti-bonding state A becomes more populated than state B (Fig. 4.9a, b, f). This corresponds to the onset of a weak lasing state at $P = \Gamma - \gamma$, where the system favors the state with the lowest decay rate[88]. The apparent asymmetry between the two sites is due to the symmetry breaking in the weak lasing regime [88]. Increasing power, bifurcation takes place and limit-cycle oscillations appear, leading to the appearance of new frequency components (Fig. 4.9(b)-(e)). We fit the spectrum of each site to equidistant Lorentzian lines. Above the bifurcation threshold, the right site R (red) consists of up to four equidistant lines, and the left site L (blue) up to three. At high pump powers, the PL eventually switches back to state B and other frequency components become insignificant, showing the system is transitionary toward the single-mode B state lasing (Fig. 4.9(e), (i)). This second transition takes place at $P = \Gamma + 3\gamma$. This sequence of transitions confirms dissipative coupling modeled by equation 4.1 and allows us to estimate the dissipative coupling rate as following. The nontrivial fixed point A state becomes stable when $p = -\gamma$. This happened at the pump power of about 2 mW in the experiment (Fig 4.9(b)). The threshold for the stable fixed point B state is when $p = 3\gamma$. This corresponds to the pump power of about 3 mW when the system stabilized to the B state with weak satellite peaks (Fig 4.9(e)). Assuming $\Gamma = 0.5\ ps^{-1}$ and P is a linear function of pump power, the estimated dissipative coupling strength is about $0.055\ ps^{-1}$.

The power-dependent K-space spectra are shown in Fig. 4.10. K-space spectra also show peculiar features of the polariton comb states. As the pump power increases (from Fig. 4.10(a) to (g)), B and A states shifts from their original peak positions at $k = 0$ and $k = \pm\pi/a$ respectively, where a is the distance between two sites. E state remains symmetric around $k = 0$, which confirms that observed shifts in B and A states are not mere artifacts. This indicates the nontrivial phase relation, neither

in-phase nor out-of-phase, between two sites as will be discussed in detail later. The nontrivial relative phase should put the k-space peak between 0 and $\pm\pi/a$ as shown in Fig. 4.10. For the highest two pump powers, the transition to the single-mode lasing at B state is observed and k-space intensity peak is gradually returning back to $k = 0$ (Fig. 4.10(f),(g)).

Another important feature is the energy gap between B and A states decreases as the pump power increases. This is because the location of the pump spot is at the center of the device, in-between the two sites, and therefore increases the potential barrier between the two due to the reservoir-induced blueshift. For numerical simulation, we used Josephson coupling strength considering this effect that J values should be much lower than the value measured at low pump power.

4.4 Beating measurement of multi-frequency components

To verify the uniformity of the mode spacing, we measure the temporal first-order coherence $g^{(1)}(\tau)$, where multiple equidistant frequency lines would manifest as strong beating signals. On the R site, where four frequency components are present, more beating peaks are observed in $g^{(1)}(\tau)$ compared to the L site. At low power, the beating signal is not well resolved due to the low coherence time (Fig. 4.11a). However, there exists a strong revival peak at 40 ps for both sites, which confirms there are multiple and equidistant frequency lines. As the populations in the two sites grow, the coherence time becomes longer, and the beating signal becomes more apparent (Fig. 4.11(b)). At higher power (Fig. 4.11(c)), the number of beating peaks and the complexity in $g^{(1)}(\tau)$ decrease, suggesting the reduction of frequency components.

We numerically solved equation 4.1 using a fourth-order Adams-Bashforth-Moulton predictor-corrector method with small initial populations in both sites. Note that the initial condition does not affect the final state which converges to the limit-cycle solu-

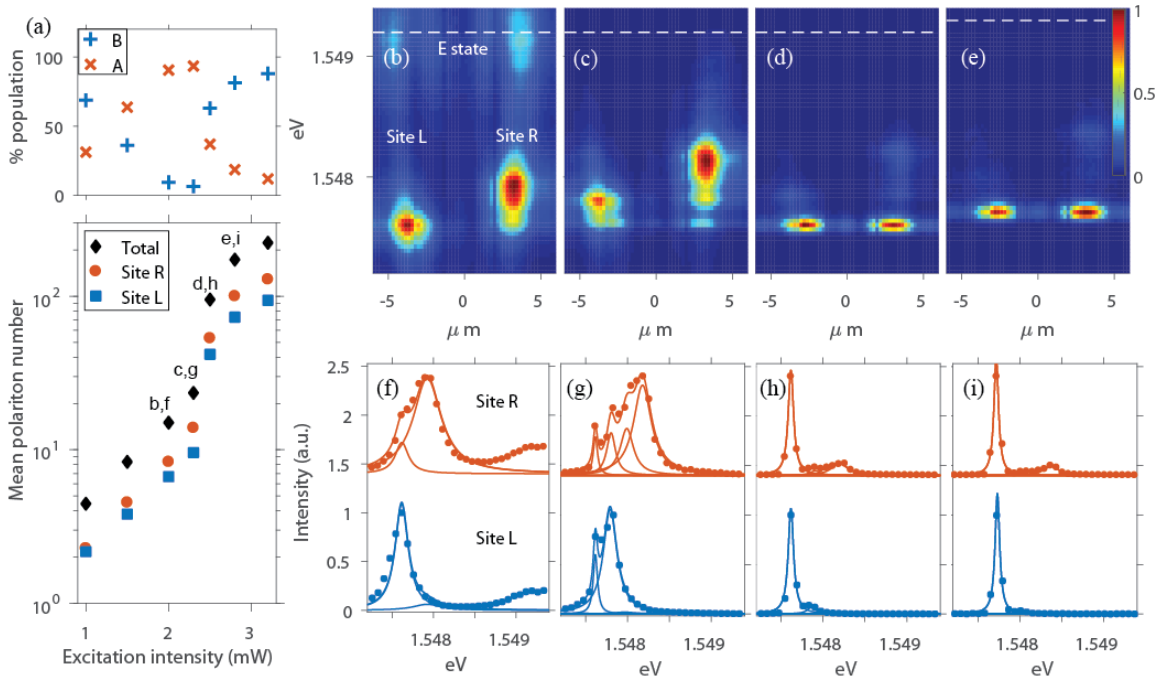

Figure 4.9: Excitation power dependence of the intensity and real-space spectra of the polariton PL near the A and B states. (a) Bottom: Mean polariton number of the A and B states vs. the excitation power for the L site (blue square), R site (red circle) and the sum of the L and R sites (black diamond). It shows clearly a threshold behavior and degenerate occupation at each site. Top: Relative fraction of the B state (blue plus) and A state (red cross) population vs. the excitation power, showing switching of the dominant state upon transitions to the A-state weak lasing and stable B-state lasing. (b)-(e), The real-space spectra at four different excitation powers, showing the transition from A state weak lasing, to limited cycles, toward B state lasing. The white dashed line marks the E state – the lowest energy state after B and A states. f-i, Spectrum of each site obtained from b-e respectively. The solid lines are fits by equidistant Lorentzians. More than two frequency components are apparent in (c), (d), (g) & (h).

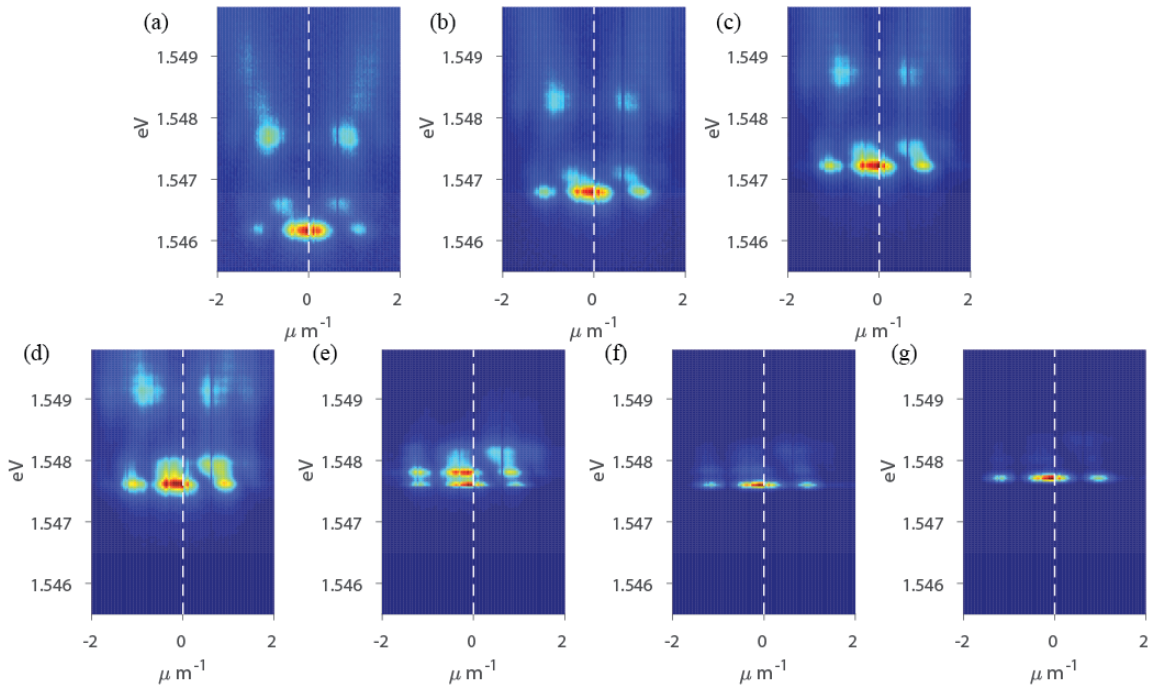

Figure 4.10: Excitation power dependent K-space spectrum. Power increases from (a) to (g). Three powers used in real-space spectra correspond to (e)-(g). White dashed line indicates $k = 0$. B and A state shift in K-space whereas the first exited states remain symmetric around $k = 0$ from a-d.

tion. To account for the effect of noise, we multiplied exponential decay functions to the simulated $g^{(1)}(\tau)$. The parameters used for Fig. 4.11(d),(e),(f) were $\Gamma = 0.5\ ps^{-1}$, $\gamma = 0.077\ ps^{-1}$, $\omega = 0$, $J = 0.077\ ps^{-1}$, $\alpha = 1.15\ ps^{-1}$, and $\mu = 0.015\ ps^{-1}$. It is important to note that α in the simulation is the polariton interaction strength multiplied by the polariton population. Considering the polariton population obtained experimentally, one requires polariton interaction strength to be an order of 10 μeV which is in agreement with previous reports in GaAs polariton systems. We change the pumping strength P to account for the strength of the excitation power assuming other parameters do not change significantly above the lasing threshold. We used $P = 0.524,\ 0.548,\ 0.627\ ps^{-1}$ respectively. We also gave 1% difference in pumping strength between two sites to account for the asymmetry in experiments.

We compare the experimental $g^{(1)}(\tau)$ with computed results based on equation 4.1, as shown in Fig. 4.11(d),(e),(f). The simulation qualitatively captures the main features in experiment and shows similar beating peaks as in the experiment.

4.5 Nontrivial phase coupling between two sites

Finally, a hallmark of the limit-cycle states is a nontrivial relative phase ϕ between the two sites. The reason for this nontrivial phase relation is the following. The dissipative coupling alone favors an out-of-phase relationship between the two sites with $\phi = \pi$. At the same time, on-site interaction changes the instantaneous frequency of each site. Interplay between these two interactions results in a nontrivial phase $\phi \neq 0$ or π between the two sites when stable limit-cycle oscillations are formed.

We measure the relative phase ϕ by interfering both sites simultaneously with a reference beam and fit the interference fringes to obtain their phases [89], illustrated in Fig. 4.12. We use the emission from one of the sites as a phase reference to determine the relative phase between the two sites, as the absolute phase of the polariton condensate is different for every experimental realization. We use a Mach-

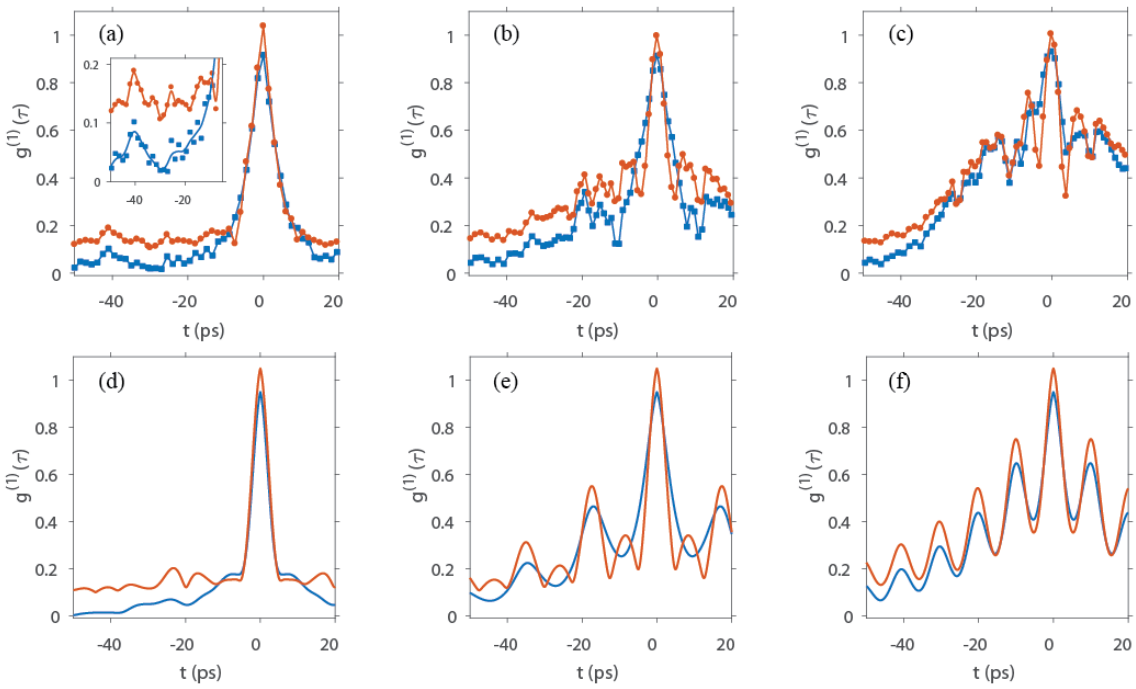

Figure 4.11: Experimental (a)-(c) and theoretical (d)-(f) $g^{(1)}(\tau)$ for three different excitation powers, corresponding to Fig. 4.9(c)-(e), respectively. Red dots are shifted vertically by 0.1 for better visibility. The inset shows a zoom in of the beating peaks in a (The lines are guides to the eye). The site with more frequency lines has more beating peaks and narrower $g^{(1)}(\tau)$ linewidths at t=0. The simulated $g^{(1)}(\tau)$ is multiplied by an exponential decay with decay times of 20, 25, 30 ps respectively.

Zehnder interferometer and magnify the image from one arm by a factor of 6 compared to the other arm. For two spatial modes of 2 μm in diameter separated by 7 μm, magnification of about 4.5 is needed in order for the single-site to interfere with the entire system. Our magnification ensures that the two sites overlap with the center of the single-site where the phase is uniform. We fit interference pattern in each site to $I_{L,R}(x) = I_{L,R}(x)(1 + |g^{(1)}_{L,R}|cos(k_x x + \phi_{L,R}))$, where $I(x)$ is the Gaussian intensity profile, k_x is the spatial frequency of the fringe pattern due to the angle between two interfering beams. The relative phase is then calculated as $|\phi_L - \phi_R|$.

As shown in figure 4.13, we obtain $\phi = 0.51 \pm 0.08\ \pi$ when the multiple frequency lines appear (Fig. 4.13a,d). When the B state brightens up at high powers, the relative phase changes to $\phi = 0.21 \pm 0.06\ \pi$ (Fig. 4.13(b),(e)) and $0.15 \pm 0.04\ \pi$ (Fig. 4.13(c),(f)), converging toward an in-phase relation for single-mode B state lasing. The above nontrivial phase relationship was also evidenced by the the shift of the $k = 0$ peak in the power-dependence of the k-space PL spectra as discussed earlier.

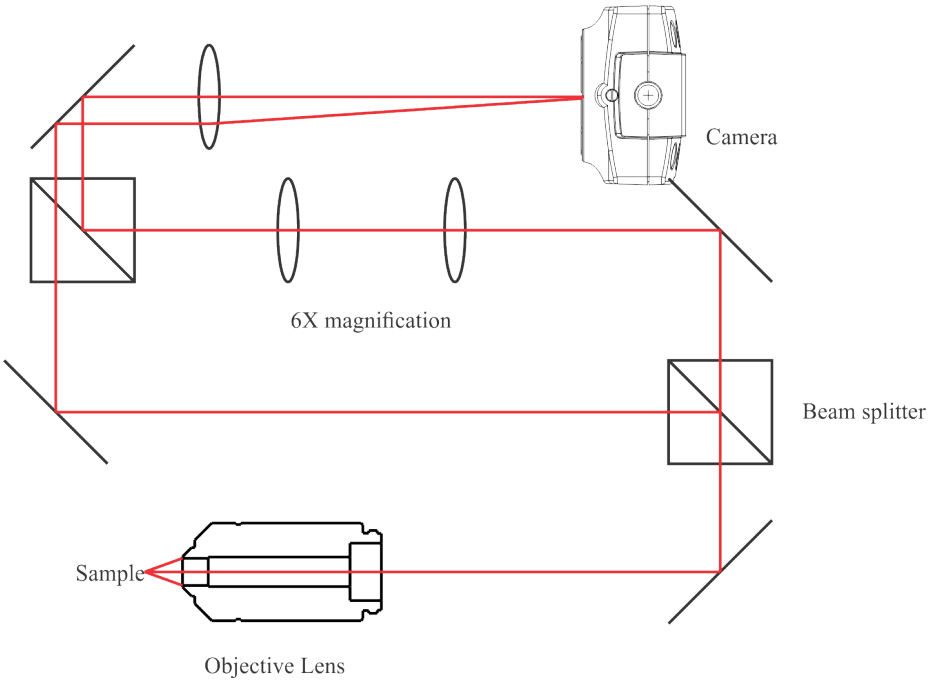

Figure 4.12: Magnified Mach-Zehnder interferometer. Magnified image provides phase reference for relative phase measurements between two sites.

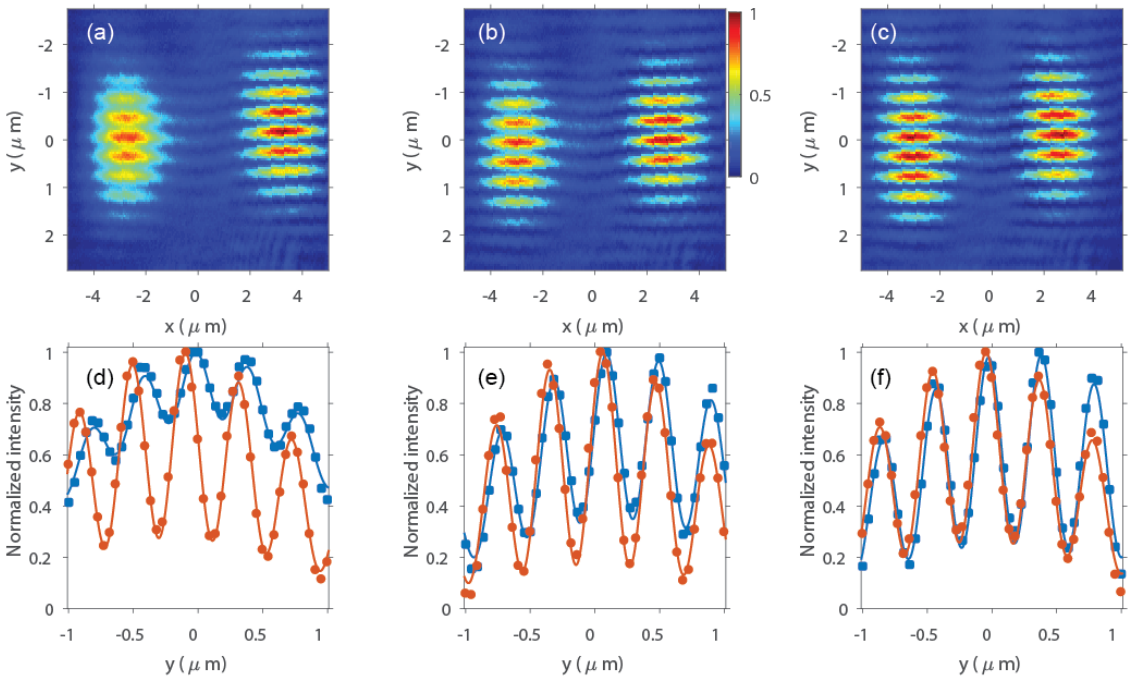

Figure 4.13: Relative phase measurement between L and R sites at excitation powers of 2 mW (a,d), 2.3 mW (b,e) and 2.5 mW (c,f). a-c, Interference images from interfering both sites to a magnified single site. d-f, Interference fringes for each site obtained from a-c along $x = \pm 3\ \mu m$ (dots). The solid lines are fits as described in Methods. From the fit, we obtain the relative phase difference of 0.51 π, 0.21 π, and 0.15 π respectively.

4.6 Conclusion

In this chapter, we have demonstrated a new mechanism of frequency comb generation, resulting from dissipative coupling and nonlinear interactions in a coupled pair of polariton condensates. The equidistant frequency lines are measured spectrally and leads to coherence revivals in $g^{(1)}(\tau)$. The relative phase between the condensates is extracted from $g^{(1)}(\tau)$ measurements; it decreases from π toward zero as the system transitions from unstable asymmetric lasing to limit-cycle to stable single-state lasing, which agrees very well with the theoretical prediction based on a model system of driven-dissipative equations for coupled polariton condensates (equation 4.1). This excitation dependence of the polariton frequency comb confirms dissipative coupling between the condensates and provides an estimate of the dissipative coupling rate of about one tenth of the decay rate. A polariton-based frequency comb may allow very low input power, as it takes place near the polariton lasing threshold without electronic population inversion. It is also compatible with on-chip electrical excitation [62]. Future work to modify the quality factor and interaction strength of the microcavities may result in narrower linewidth of individual comb lines and greater line spacing up to terahertz frequencies.

CHAPTER V

SWG-Microcavity Optomechanics

In this chapter, I'll present the experimental observation of optomechanical effect in HCG microcavities. Optomechanical coupling between mechanical modes and photon modes provides wide range of research interests such as radiation-pressure cooling of mechanical mode [90], optomechanical squeezing of light [91], and sensing applications [92, 54]. Recently, coupling mechanical mode with active cavity was realized in HCG-VCSEL structure [54]. Here, optical and mechanical modes are dispersively coupled since the mechanical motion of HCG directly modulates the cavity resonance. Unique to polariton systems, mechanical motion of cavity mirrors (in this case, HCG mirrors) is not only coupled to the optical resonance (LP resonance) but also to the dissipation rate of the LP resonance. This is because the position of the mirror changes the exciton-photon detuning, which in turn changes the decay rate of the polariton mode determined by exciton and photon fractions. Simply, exciton-like polairtons decay slower like excitons and photon-like polaritons decay faster following the cavity decay rate. The presence of both dispersive and dissipative couplings could lead to the unconventional bistability and Q-switching behavior of polariton lasers [93].

5.1 Mechanical mode of HCG mirrors

The mechanical resonance of the HCG structure was simulated by COMSOL (Fig. 5.1). The grating parameters are $L = 7.5\mu m, W = 200nm, T = 80nm, \Gamma = 500nm$. The fundamental mechanical mode is 2.8 MHz.

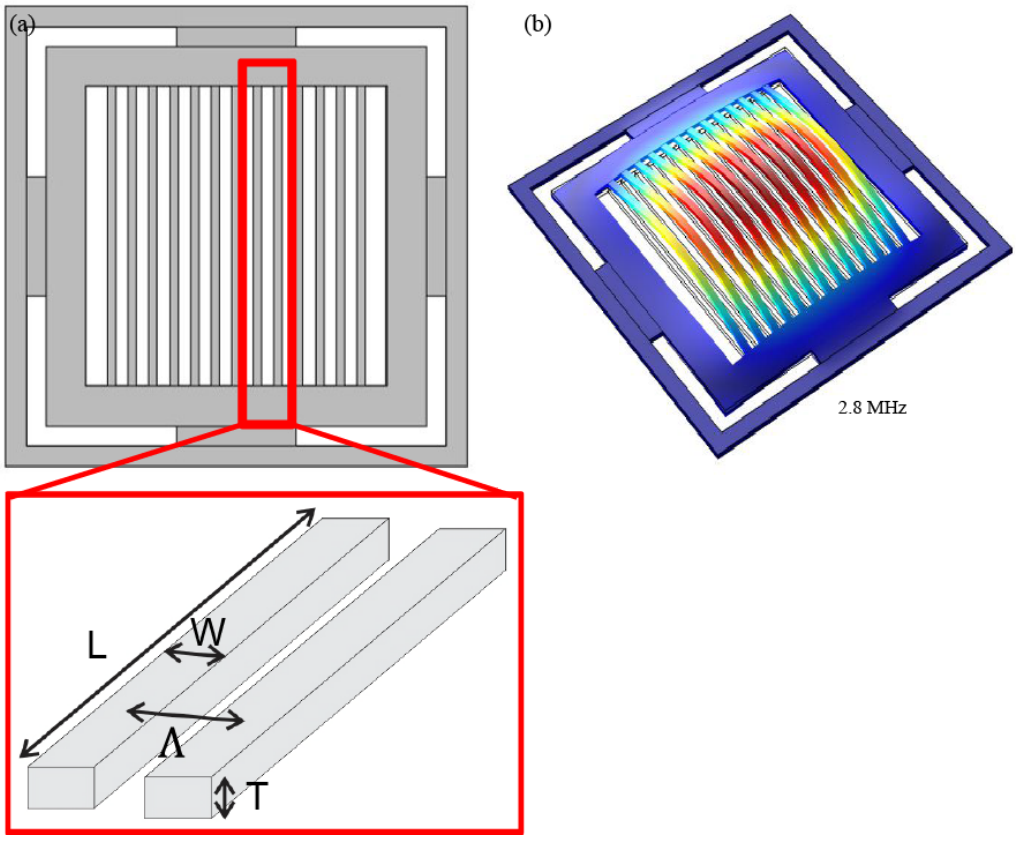

Figure 5.1: Simulated mechanical modes of HCG. (a) A drawing of HCG membrane. (b) Simulated fundamental mechanical mode of 2.8 MHz.

5.2 Experimental observation of polariton optomechanics

The evidence of optomechanical oscillations is first identified by the spectrum. Above a certain threshold, multiple spectrally discrete modes appeared as shown in Fig. 5.2(a). This discreteness seemed very different from what was observed in HCG-VCSEL. If we only consider dispersive coupling, the oscillation of mirrors should not

affect the lasing threshold for different mirror positions. In other words, the laser gain, which is determined by the pump strength and dissipation rate of the lasing mode, does not depend on the resonance of the lasing mode. Indeed, wavelength measurements in HCG-VCSEL shows continuously broad spectrum [54]. For polariton, the lasing threshold depends sensitively on the exciton-photon detuning, therefore when the mirrors move to the position where the lasing threshold is high, the emission can switch off. The simple harmonic oscillation of the HCG mirror accompanied by increase of oscillation amplitude is illustrated in Fig. 5.2(b). The bright emission only happens when the detuning is right, normally with negative detuning.

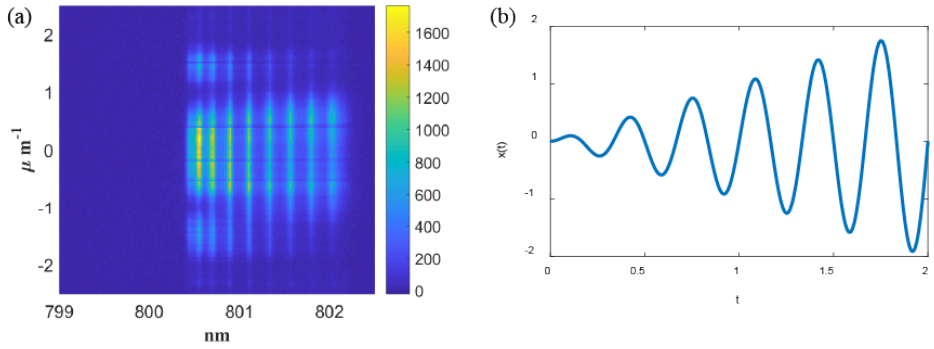

Figure 5.2: (a) Discrete spectral peaks above the mirror oscillation threshold. (b) Simple harmonic motion of the HCG mirror with a growing amplitude.

We further investigated in time-domain to see the optomechanical effect. We used quasi-CW laser modulated by EOM and the same RF signal provided a sync signal for the time interval analyzer (TIA) (Hydraharp 400). The PL emission was sent to the avalanche photodiode and then to the other input of TIA. We first analyze the emission timing of different wavelengths by spectral filtering (Fig. 5.3(a)). The longer wavelength components appear later than the shorter wavelength components, indicating that the oscillation amplitude keeps growing. To avoid damaging the HCG microcavity, we couldn't let the oscillation amplitude grow and had to limit the excitation pulse widths. The oscillation frequency of 2.86 MHz shown in Fig. 5.3(a) is consistent with the fundamental mechanical mode from COMSOL simulation.

Remarkably, repetitive short pulses were measured from some of the experiments (Fig. 5.3(c)). The measured pulse width is about 30 nsec which is much shorter than the mechanical frequency. Moreover, the peak intensity of this short pulse is much higher than that of the other wavelength components (Fig. 5.3(d)). This bright pulsing with asymmetric pulse shape might be explained by Q-switching behavior [93]. However, further analysis and systematic studies are required to support the claim. A simple model with dispersive and dissipative coupling can produce intensity oscillations depending on amplitudes of mechanical oscillations and excitation powers as shown in Fig. 5.4. This model includes a polariton mode, a mechanical mode, and an exciton reservoir. Below the lasing threshold where there's no lasing without mechanical oscillations (Fig. 5.4(a)), the lasing mode can reach threshold with the support of mechanical oscillations due to the modulation of the decay rate (Fig. 5.4(b)). In this case, the pulse width is much narrower than the mechanical oscillation period. Above the threshold, although mechanical ocillations still modulate the polariton lasing intensity, the pulse width becomes larger compared to the below threshold case. More realistic model would require multiple polariton modes which would turn on and off as the mirror oscillates. Another important thing to verify is what causes this ocillations since the radiation pressure is unlikely to cause the oscillations. More likely scenario would be heating of the HCG mirror due to optical excitation. It will be also interesting to incorporate metal contacts to modulate HCG electrically [53] and study the polariton output field.

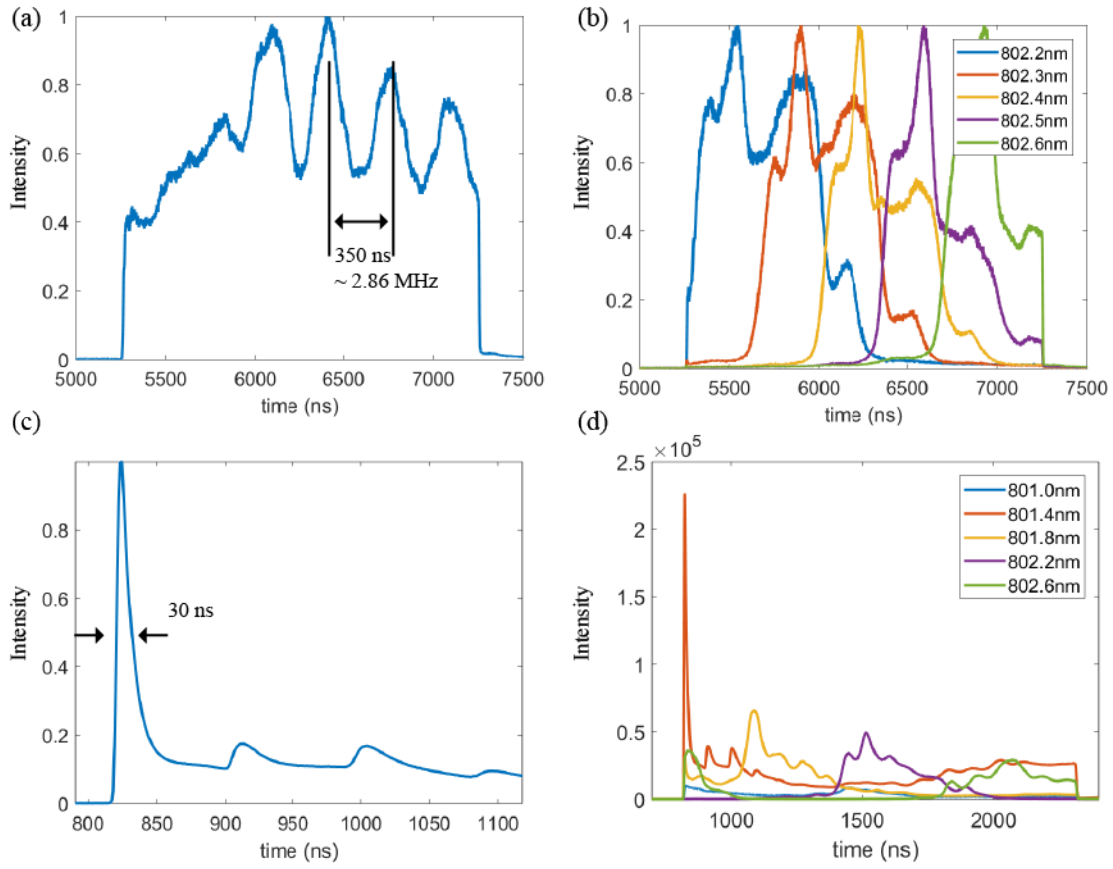

Figure 5.3: Time-domain measurements. (a) Time-resolved intensity showing a periodic oscillation at 2.86 MHz. (b) Spectrum- and time-resolved measurements. Different spectral components appear at different time. (c) Pulsing with much shorter width than the mechanical oscillation. (d) Relative amplitude of pulsing compared to other oscillating intensities with different spectral components.

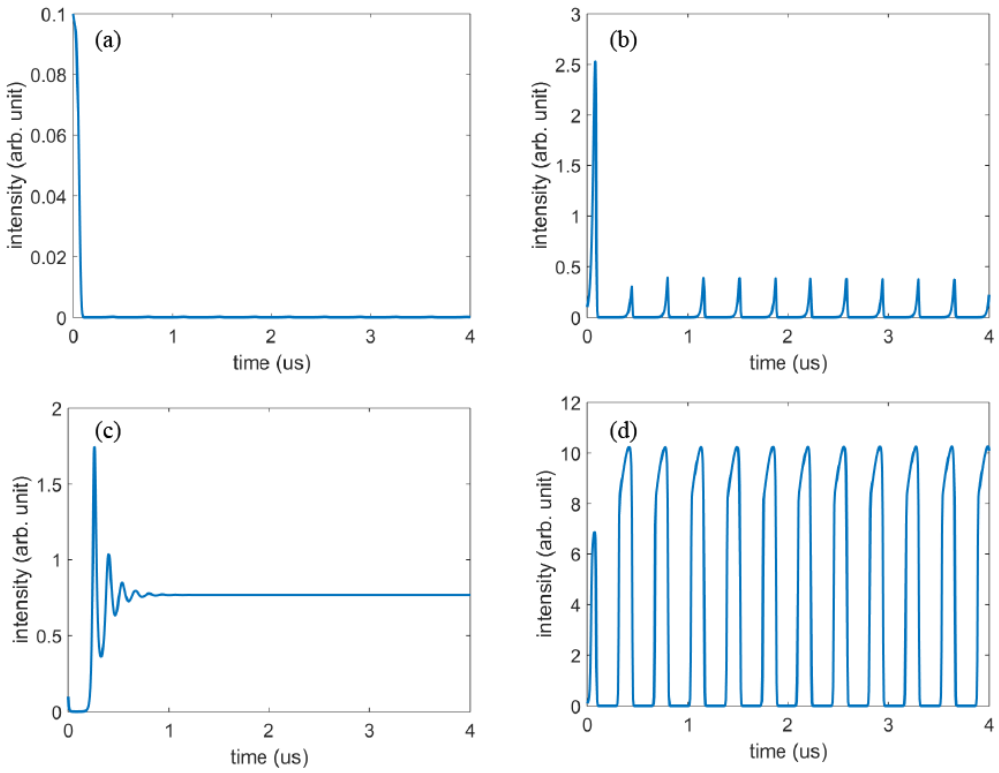

Figure 5.4: Simulation results. Below lasing threshold (a) without mirror oscillations and (b) with mirror oscillations. Above lasing threshold (c) without mirror oscillations and (d) with mirror oscillations

CHAPTER VI

Orbital Angular Momentum and Vector Beam Generation

Orbital angular momentum (OAM) of light offers an additional degree of freedom for carrying information in orthogonal basis. Entangling and superposition of OAM states can also be used for quantum information protocols [94, 95]. Quantized vortices in Bose-Einstein condensates have been investigated in many platforms in atomic [8] and polariton condensates [30, 96, 31]. Quantized vortices in polariton condensates in particular transfer into optical vortices when the condensates decay into photons. These optical vortices can be described by OAM states. Understanding and manipulating quantized vortices in polariton condensates, therefore, are of great interest to study vortex dynamics in driven-dissipative condensates as well as generating OAM microlasers. Many efforts to create polariton vortices have been made using natural defects in the microcavities [96] and optical means [31, 97, 98]. For systematic study of vortex-vortex interactions, resonant excitation with OAM states has been used [99]. With many techniques to manipulate microcavities, we can now create quantized vortices and OAM states at the region defined by nanofabrication, making defects by etching [100].

Here we create defect patterns on MHCG structures and show the formation of quantized vortices around the etched defects. By modifying the structure of the de-

fect, we were also able to obtain not only vortex-antivortex pairs, but also single vortex which can be used as OAM microlasers. Controllable polarization through HCG design also allows us to realize vector beams where the polarization states vary spatially. Furthermore, this method can be used to position quantized vortices deterministically and study vortex-vortex interactions by varying the distance between vortices.

6.1 Detection of quantized vortices in polariton condensates

Quantized vortices manifest themselves by phase singularity, $2\pi N$ phase change surrounding the singularity where N is an integer. Interfering optical vortices with the Gaussian reference beam yield unique interference patterns (fork patterns) at the phase singularity as shown in Fig. 6.1. For nonresonantly excited polariton condensates, the choice of reference beams is not obvious because the absolute phase of the condensate is unknown. What we can do is that we can magnify a small portion of a condensate and assume that the phase is uniform which should be a good assumption as long as a condensate is formed (due to long-rage order). Then we can use this as a reference and interfere with the part of a condensate where defects are located.

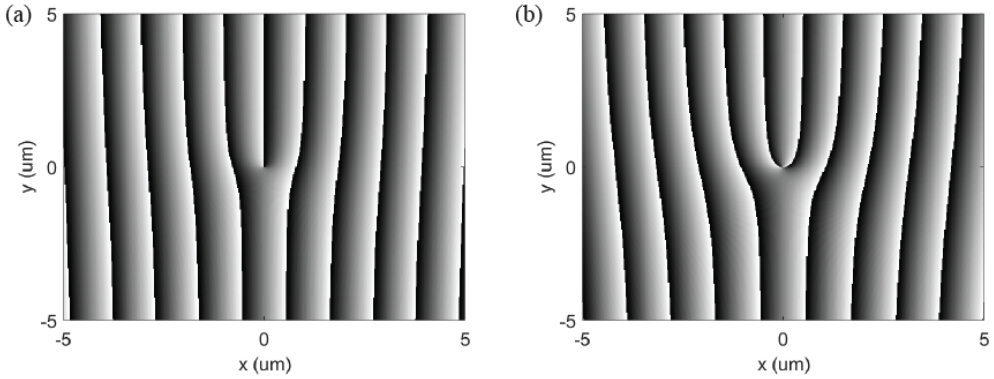

Figure 6.1: Simulated fork patterns from interfering OAM with flat phase reference with a finite angle. (a) 2π phase winding, $l = 1$ (b) 4π phase winding, $l = 2$.

To find out whether the vortices are present or not, we can inspect the interference images by eye and find fork patterns. However, this method becomes difficult when there are many vortices or high-order vortices ($N > 1$). Based on Fourier transform, it is possible to directly extract phase from the interference images (Fig. 6.2). We can describe signal and reference fields as $E_s = A_s e^{-i(\omega t - \boldsymbol{k}_s \cdot \boldsymbol{r} + \phi(\boldsymbol{r}))}$ and $E_r = A_r e^{-i(\omega t - \boldsymbol{k}_r \cdot \boldsymbol{r})}$ respectively, assuming the reference has a uniform phase distribution. $\boldsymbol{k}_s$ and $\boldsymbol{k}_r$ describe incident angles of signal and reference beams into the camera. Then the interference intensity is given by,

$$I(\boldsymbol{r}) = |A_s|^2 + |A_r|^2 + (A_s A_r^* e^{-i(\Delta \boldsymbol{k} \cdot \boldsymbol{r} + \phi(\boldsymbol{r}))} + c.c.) \tag{6.1}$$

where $\Delta \boldsymbol{k} = \boldsymbol{k}_r - \boldsymbol{k}_s$. Fourier transfrom of this equation will result in three different k components, one centered at $\boldsymbol{k} = 0$, one centered at $\boldsymbol{k} = \Delta \boldsymbol{k}$, and one centered at $\boldsymbol{k} = -\Delta \boldsymbol{k}$. We can filter out the one at either $\pm \Delta \boldsymbol{k}$ and get $\mathcal{F}[A_s A_r e^{\pm i\phi(\boldsymbol{r})}]$. Taking the argument of inverse Fourier transform produces $\pm i\phi(\boldsymbol{r})$ which is the phase profile of the signal beam.

6.2 Experimental observation of quantized vortices

To study defect-induced vortices, we fabricated many devices with different shapes, sizes, and number of defects. A few examples of fabricated devices are shown in Fig. 6.3 and Fig. 6.5. We used nonresonant CW excitation and expanded the beam to fully cover the devices. The emission was sent to the spectrometer and interferometer. For defects with circular symmetry, we observed vortex-antivortex pair that is formed around the defect location 6.4(a),(b). Other patterns without this symmetry tend to form a single vortex 6.4(c),(d). Obtaining pure orbital angular momentum state from polariton laser was challenging and required complex optical beam engineering [97, 98] or defect cavity with polarized excitation [100]. This simple method of defect

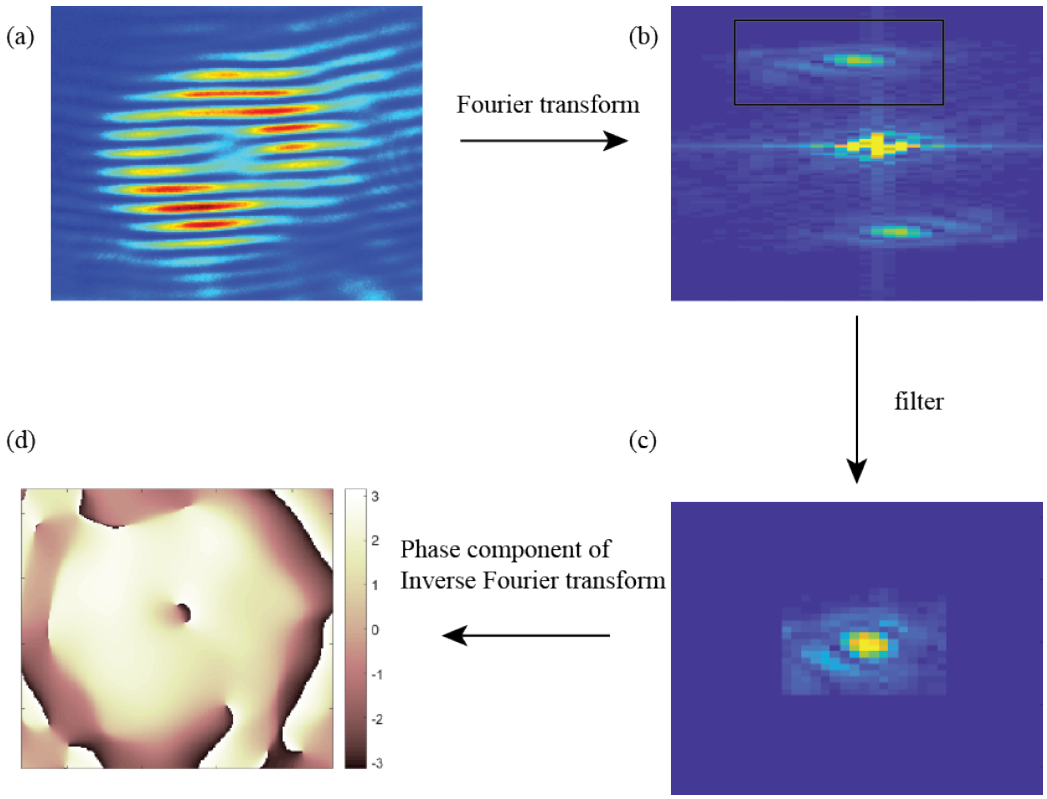

Figure 6.2: Fourier transform-based phase extraction technique. (a) Raw interference data. (b) Fourier transform image. Two side peaks are due to fringe pattern. (c) Filtering one of two side peaks. (d) Phase map after inverse Fourier transform of (c) showing a vortex-antivortex pair.

patterning does not require a specific excitation scheme and may enable electrical excitation. Further defect engineering through numerical simulation of Gross-Pitaevskii equation may result in controlled generation of OAM light from polariton lasers.

We also implanted multiple defects and measured quantized vortices. A few example of measured phase are shown in 6.6. As expected, there are multiple quantized vortices around defects. To further study their interactions, it may be necessary to employ time-resolved interferometry using a streak camera [99].

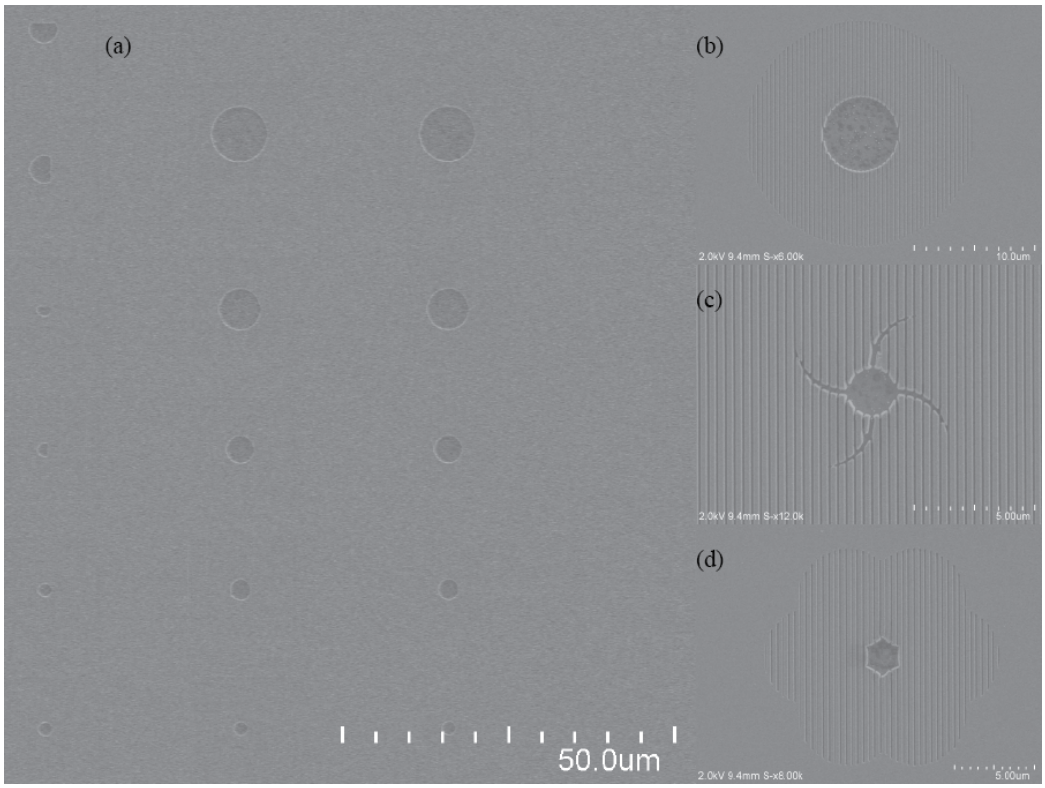

Figure 6.3: SEM images of single defect devices. (a) Rectangular devices with different shape and size of defects. (b) Circular device with circular defect. (c) Device without circular symmetry. (d) Photonic benzene.

6.3 OAM-carrying radially polarized vector beam generation

Vector beams, beams with spatially varying polarization, have drawn attention for their applications such as super-resolution imaging [101]. It has been shown theo-

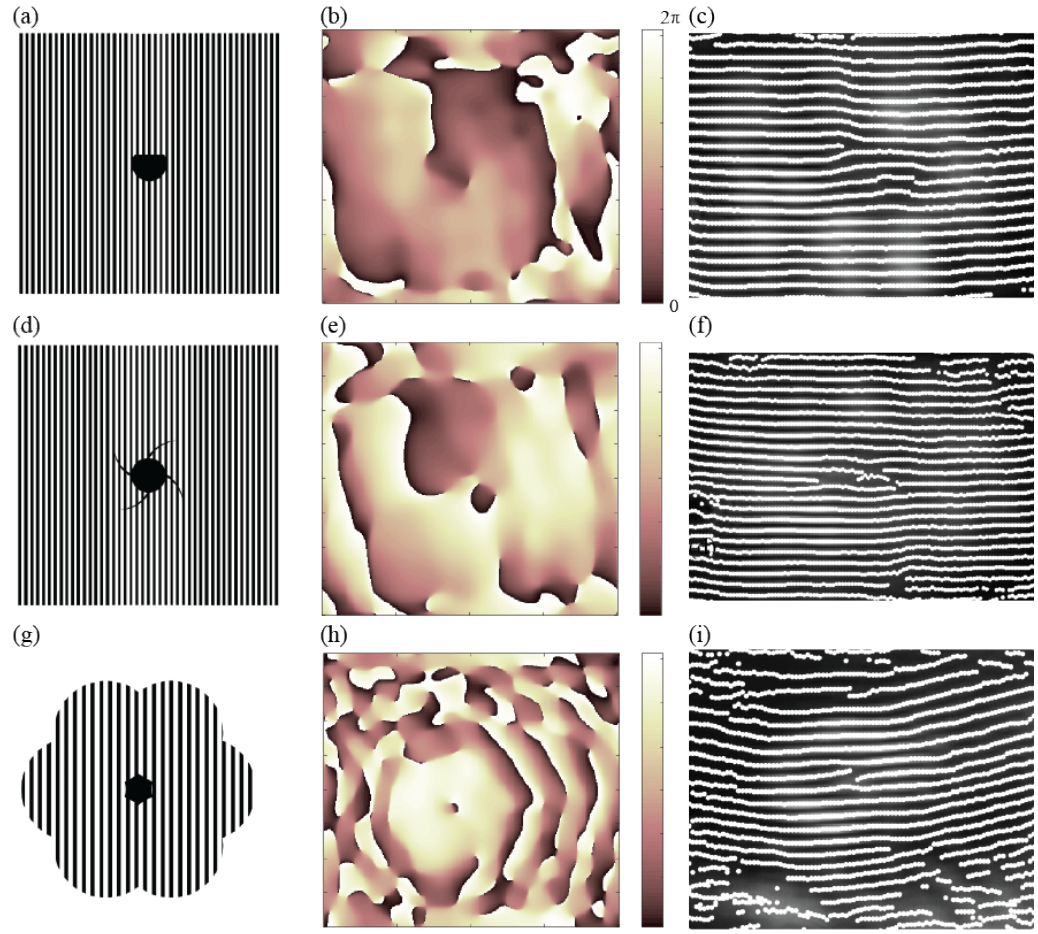

Figure 6.4: Retrieved phase of single-defect devices. (a), (d), (e) Device structures. (b), (e), (h) phase maps of (a), (d), (e). (c), (f), (i) interference fringe of (a), (d), (e).

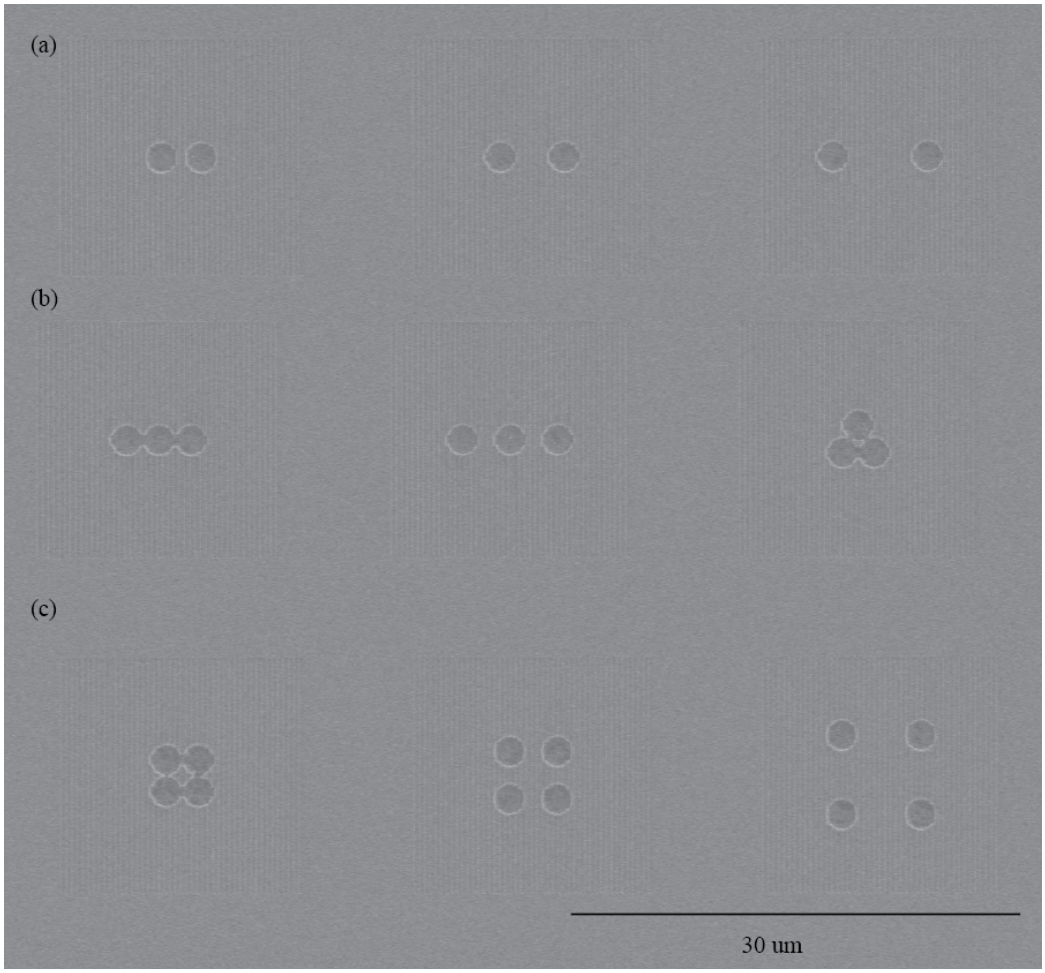

Figure 6.5: SEM images of multiple defect devices. (a) Devices with two defects. (b) Three defects. (c) Four defects.

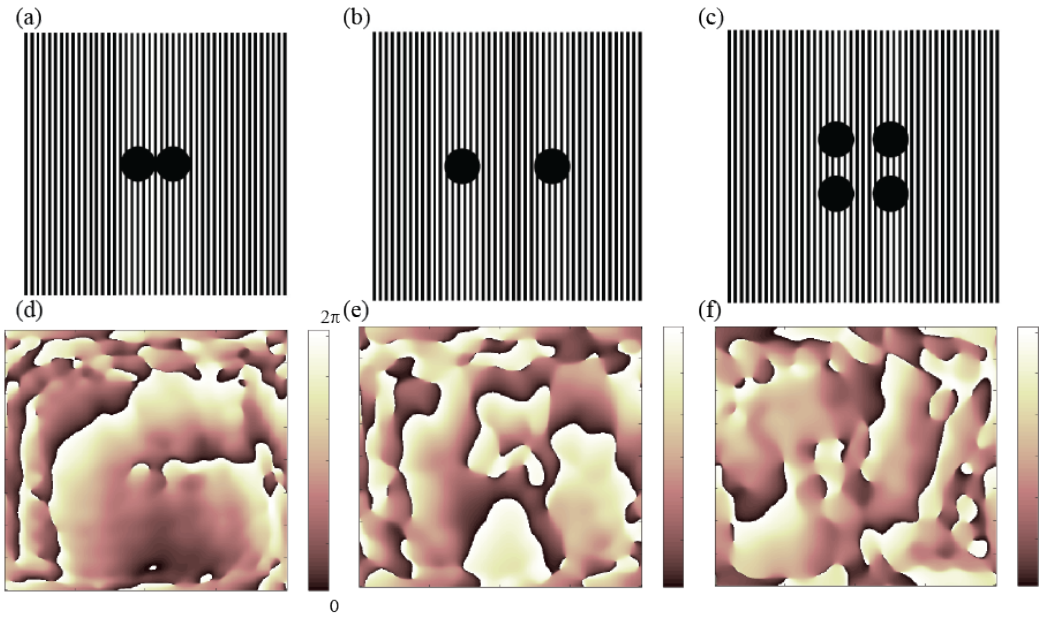

Figure 6.6: Retrieved phase of multiple defect devices. (a), (d), (e) Device structures. (b), (e), (h) phase maps of (a), (d), (e).

retically and experimentally that radially polarized vector beams can achieve tighter focus spots [102]. Moreover, additional control over polarization may provide more degrees of freedom for optical communications. Here, we realized radially polarized vector beams with OAM from MHCG-based polariton lasers. The polariton emission from MHCG microcavities is polarized perpendicular to the grating bar. Therefore, patterning circular gratings (Fig. 6.7) allows us to have radially polarized polariton emission. Azimuthally polarized emission should also be possible if we design MHCG polarization to be parallel to the grating bar. To experimentally confirm the emission polarization and existence of OAM, we put the analyzer at the emission path and measured the spatial profile of the polarization filtered emission as shown in Fig. 6.8(b), (c). The orientation of bright emission lobes are aligned with the axis of the linear polarizer as expected from radial polarization states. Without the polarizer, the emission pattern is circular (Fig. 6.8(a)). The detected OAM is shown in Fig. 6.8(d). Figure 6.8(e), (f) show spectrally resolved r- and k-space images of the polariton lasing states, respectively. OAM-carrying vector beams have been recently

reported in microring lasers utilizing non-Hermitian photonics at an exceptional point [103]. This approach requires complex patterning of metal layer to modulate gain/loss properties of the system for non-Hermitian photonics. Our approach utilized intrinsic polariton selectivity of HCG and patterning simple circular gratings is sufficient to achieve OAM-carrying radially polarized vector beams.

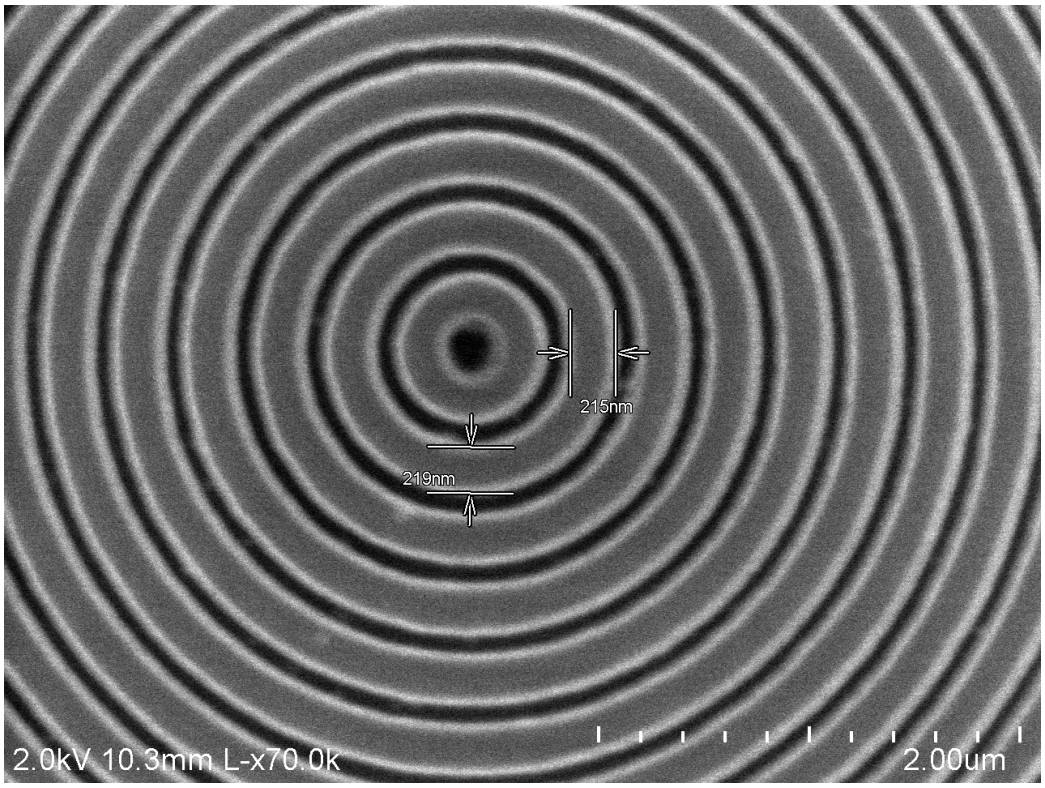

Figure 6.7: SEM image of circular gratings for a vector beam device.

The method presented in this chapter for vortex generation is very simple but yet shows some significant results. For conventional DBR microcavities, it would require deep etching to introduce substantial defect potential and may require very careful etching process. With MHCG, since the top mirror is only a single layer, it is enough to create defect potential by etching only a top layer of about 200 nm, taking about 1 min to etch. Also we can pattern small features to break defect symmetry and show a formation of a single vortex, which also may be difficult to implement in conventional DBR microcavities. Further simulation based on GrossPitaevskii

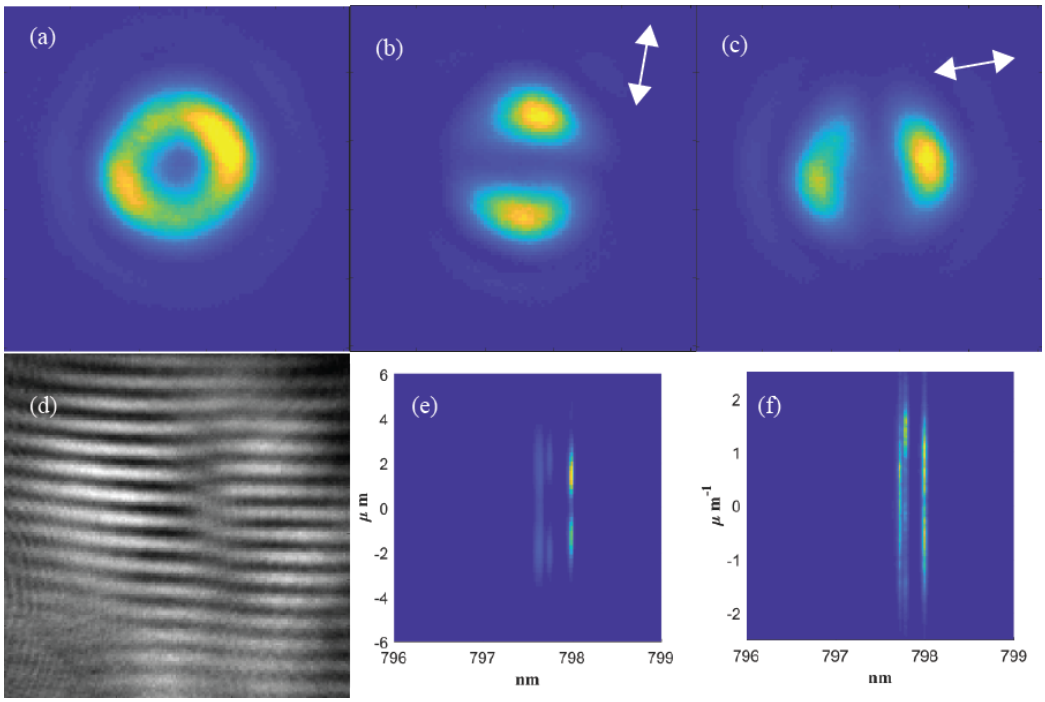

Figure 6.8: Experimental results of a vector beam generation. (a) Polarization dependent spatial emission pattern. (b) OAM detection (c), (d) r- and k-space spectrum of the polariton laser

equation would provide further insights on the observed phenomena and lead the future development of polariton OAM lasers. Lastly, straight forward control over polarization taking advantage of polarization selectivity of HCG is possible to create vector beams and provide additional degrees of freedom.

CHAPTER VII

Conclusions and Outlook

In this thesis, I have presented detailed process to realize HCG-based microcavities and their device applications. The main difference of HCG-based microcavities compared to the conventional DBR-based microcavities is its polarization selectivity making it possbile to realize a single-mode polariton condensate or laser. We achieved fully coherent polariton lasers, which the coherence properties were explained by the theory developed for atom lasers. By controlling polariton-polariton interactions, we showed 300-fold increase of the phase coherence from the decay time. This significant improvement and understanding of coherence properties would guide future developments toward practical low threshold coherent sources. Upon coupling two condensates by strain engineering, we realized coupled nonlinear polariton devices, which produced equidistant frequency components. The phenomenon was explained by considering strong on-site interaction strength and complex inter-site coupling coefficients. This novel way to create a optical frequency comb requires very low threshold and has potential to be electrically driven. The comb spacing can be adjusted up to THz frequencies, possible for applications such as low threshold THz sources. Finally, we presented the possibility for polariton optomechanics, controlled vortices and OAM generation, and vector beam generation from HCG-based microcavities.

Now we have a good understanding on polariton condensates in HCG-based micro-

cavities. Coupling condensate sites is possible through strain engineering and other grating parameters such as periods or duty cycles. Therefore, it would be interesting to study HCG-based polariton lattices and periodic chain which are mostly studied in etched micropillar structures. Understanding polariton optomechanics and vortex generation through numerical simulation would be another important direction to pursue.

BIBLIOGRAPHY

BIBLIOGRAPHY

[1] Hui Deng, Gregor Weihs, David Snoke, Jacqueline Bloch, and Yoshihisa Yamamoto. Polariton lasing vs. photon lasing in a semiconductor microcavity. *Proceedings of the National Academy of Sciences*, 100(26):15318–15323, December 2003.

[2] Daniele Bajoni, Pascale Senellart, Esther Wertz, Isabelle Sagnes, Audrey Miard, Aristide Lematre, and Jacqueline Bloch. Polariton Laser Using Single Micropillar GaAs-GaAlAs Semiconductor Cavities. *Physical Review Letters*, 100(4):047401, January 2008.

[3] M. H. Anderson, J. R. Ensher, M. R. Matthews, C. E. Wieman, and E. A. Cornell. Observation of Bose-Einstein Condensation in a Dilute Atomic Vapor. *Science*, 269(5221):198–201, July 1995.

[4] K. B. Davis, M. O. Mewes, M. R. Andrews, N. J. van Druten, D. S. Durfee, D. M. Kurn, and W. Ketterle. Bose-Einstein Condensation in a Gas of Sodium Atoms. *Physical Review Letters*, 75(22):3969–3973, November 1995.

[5] M. R. Andrews, C. G. Townsend, H.-J. Miesner, D. S. Durfee, D. M. Kurn, and W. Ketterle. Observation of Interference Between Two Bose Condensates. *Science*, 275(5300):637–641, January 1997.

[6] M. R. Matthews, B. P. Anderson, P. C. Haljan, D. S. Hall, C. E. Wieman, and E. A. Cornell. Vortices in a Bose-Einstein Condensate. *Physical Review Letters*, 83(13):2498–2501, September 1999.

[7] K. W. Madison, F. Chevy, W. Wohlleben, and J. Dalibard. Vortex Formation in a Stirred Bose-Einstein Condensate. *Physical Review Letters*, 84(5):806–809, January 2000.

[8] J. R. Abo-Shaeer, C. Raman, J. M. Vogels, and W. Ketterle. Observation of Vortex Lattices in Bose-Einstein Condensates. *Science*, 292(5516):476–479, April 2001.

[9] A. Smerzi, S. Fantoni, S. Giovanazzi, and S. R. Shenoy. Quantum Coherent Atomic Tunneling between Two Trapped Bose-Einstein Condensates. *Physical Review Letters*, 79(25):4950–4953, December 1997.

[10] F. S. Cataliotti, S. Burger, C. Fort, P. Maddaloni, F. Minardi, A. Trombettoni, A. Smerzi, and M. Inguscio. Josephson Junction Arrays with Bose-Einstein Condensates. *Science*, 293(5531):843–846, August 2001.

[11] Kevin E. Strecker, Guthrie B. Partridge, Andrew G. Truscott, and Randall G. Hulet. Formation and propagation of matter-wave soliton trains. *Nature*, 417(6885):150–153, May 2002.

[12] S. Inouye, M. R. Andrews, J. Stenger, H.-J. Miesner, D. M. Stamper-Kurn, and W. Ketterle. Observation of Feshbach resonances in a BoseEinstein condensate. *Nature*, 392(6672):151–154, March 1998.

[13] Cheng Chin, Rudolf Grimm, Paul Julienne, and Eite Tiesinga. Feshbach resonances in ultracold gases. *Reviews of Modern Physics*, 82(2):1225–1286, April 2010.

[14] Markus Greiner, Olaf Mandel, Tilman Esslinger, Theodor W. Hnsch, and Immanuel Bloch. Quantum phase transition from a superfluid to a Mott insulator in a gas of ultracold atoms. *Nature*, 415(6867):39–44, January 2002.

[15] Immanuel Bloch. Ultracold quantum gases in optical lattices. *Nature Physics*, 1(1):23–30, October 2005.

[16] L. V. Butov, A. Zrenner, G. Abstreiter, G. Bhm, and G. Weimann. Condensation of Indirect Excitons in Coupled AlAs/GaAs Quantum Wells. *Physical Review Letters*, 73(2):304–307, July 1994.

[17] A. A. High, J. R. Leonard, A. T. Hammack, M. M. Fogler, L. V. Butov, A. V. Kavokin, K. L. Campman, and A. C. Gossard. Spontaneous coherence in a cold exciton gas. *Nature*, 483(7391):584–588, March 2012.

[18] Alex A. High, Ekaterina E. Novitskaya, Leonid V. Butov, Micah Hanson, and Arthur C. Gossard. Control of Exciton Fluxes in an Excitonic Integrated Circuit. *Science*, 321(5886):229–231, July 2008.

[19] Hui Deng, Hartmut Haug, and Yoshihisa Yamamoto. Exciton-polariton Bose-Einstein condensation. *Reviews of Modern Physics*, 82(2):1489–1537, May 2010.

[20] Iacopo Carusotto and Cristiano Ciuti. Quantum fluids of light. *Reviews of Modern Physics*, 85(1):299–366, February 2013.

[21] S. Christopoulos, G. Baldassarri Hger von Hgersthal, A. J. D. Grundy, P. G. Lagoudakis, A. V. Kavokin, J. J. Baumberg, G. Christmann, R. Butt, E. Feltin, J.-F. Carlin, and N. Grandjean. Room-Temperature Polariton Lasing in Semiconductor Microcavities. *Physical Review Letters*, 98(12):126405, March 2007.

[22] S. Kna-Cohen and S. R. Forrest. Room-temperature polariton lasing in an organic single-crystal microcavity. *Nature Photonics*, 4(6):371–375, June 2010.

[23] Claude Weisbuch, M. Nishioka, A. Ishikawa, and Y. Arakawa. Observation of the coupled exciton-photon mode splitting in a semiconductor quantum microcavity. *Physical Review Letters*, 69(23):3314–3317, 1992.

[24] Yongbao Sun, Patrick Wen, Yoseob Yoon, Gangqiang Liu, Mark Steger, Loren N. Pfeiffer, Ken West, David W. Snoke, and Keith A. Nelson. Bose-Einstein Condensation of Long-Lifetime Polaritons in Thermal Equilibrium. *Physical Review Letters*, 118(1):016602, January 2017.

[25] Hui Deng, Gregor Weihs, Charles Santori, Jacqueline Bloch, and Yoshihisa Yamamoto. Condensation of Semiconductor Microcavity Exciton Polaritons. *Science*, 298(5591):199–202, October 2002.

[26] J. Kasprzak, M. Richard, S. Kundermann, A. Baas, P. Jeambrun, J. M. J. Keeling, F. M. Marchetti, M. H. Szymaska, R. Andr, J. L. Staehli, V. Savona, P. B. Littlewood, B. Deveaud, and Le Si Dang. BoseEinstein condensation of exciton polaritons. *Nature*, 443(7110):409–414, September 2006.

[27] R. Balili, V. Hartwell, D. Snoke, L. Pfeiffer, and K. West. Bose-Einstein Condensation of Microcavity Polaritons in a Trap. *Science*, 316(5827):1007–1010, May 2007.

[28] A. Amo, S. Pigeon, D. Sanvitto, V. G. Sala, R. Hivet, I. Carusotto, F. Pisanello, G. Lemnager, R. Houdr, E. Giacobino, C. Ciuti, and A. Bramati. Polariton Superfluids Reveal Quantum Hydrodynamic Solitons. *Science*, 332(6034):1167–1170, June 2011.

[29] C. W. Lai, N. Y. Kim, S. Utsunomiya, G. Roumpos, H. Deng, M. D. Fraser, T. Byrnes, P. Recher, N. Kumada, T. Fujisawa, and Y. Yamamoto. Coherent zero-state and -state in an excitonpolariton condensate array. *Nature*, 450(7169):529–532, November 2007.

[30] K. G. Lagoudakis, M. Wouters, M. Richard, A. Baas, I. Carusotto, R. Andr, Le Si Dang, and B. Deveaud-Pldran. Quantized vortices in an excitonpolariton condensate. *Nature Physics*, 4(9):706–710, September 2008.

[31] Georgios Roumpos, Michael D. Fraser, Andreas Lffler, Sven Hfling, Alfred Forchel, and Yoshihisa Yamamoto. Single vortex-antivortex pair in an exciton-polariton condensate. *Nature Physics*, 7(2):129–133, February 2011.

[32] K. G. Lagoudakis, B. Pietka, M. Wouters, R. Andr, and B. Deveaud-Pldran. Coherent Oscillations in an Exciton-Polariton Josephson Junction. *Physical Review Letters*, 105(12):120403, September 2010.

[33] M. Abbarchi, A. Amo, V. G. Sala, D. D. Solnyshkov, H. Flayac, L. Ferrier, I. Sagnes, E. Galopin, A. Lematre, G. Malpuech, and J. Bloch. Macroscopic quantum self-trapping and Josephson oscillations of exciton polaritons. *Nature Physics*, 9(5):275–279, May 2013.

[34] M. Sich, D. N. Krizhanovskii, M. S. Skolnick, A. V. Gorbach, R. Hartley, D. V. Skryabin, E. A. Cerda-Mndez, K. Biermann, R. Hey, and P. V. Santos. Observation of bright polariton solitons in a semiconductor microcavity. *Nature Photonics*, 6(1):50–55, January 2012.

[35] N. Takemura, S. Trebaol, M. Wouters, M. T. Portella-Oberli, and B. Deveaud. Polaritonic Feshbach resonance. *Nature Physics*, 10(7):500–504, July 2014.

[36] Lydie Ferrier, Esther Wertz, Robert Johne, Dmitry D. Solnyshkov, Pascale Senellart, Isabelle Sagnes, Aristide Lematre, Guillaume Malpuech, and Jacqueline Bloch. Interactions in Confined Polariton Condensates. *Physical Review Letters*, 106(12):126401, March 2011.

[37] Seonghoon Kim, Bo Zhang, Zhaorong Wang, Julian Fischer, Sebastian Brodbeck, Martin Kamp, Christian Schneider, Sven Hfling, and Hui Deng. Coherent Polariton Laser. *Physical Review X*, 6(1):011026, March 2016.

[38] Thomas Fink, Anne Schade, Sven Hfling, Christian Schneider, and Ata Imamoglu. Signatures of a dissipative phase transition in photon correlation measurements. *Nature Physics*, 14(4):365, April 2018.

[39] Na Young Kim, Kenichiro Kusudo, Congjun Wu, Naoyuki Masumoto, Andreas Lffler, Sven Hfling, Norio Kumada, Lukas Worschech, Alfred Forchel, and Yoshihisa Yamamoto. Dynamical d-wave condensation of exciton-polaritons in a two-dimensional square-lattice potential. *Nature Physics*, 7(9):681–686, September 2011.

[40] T. Jacqmin, I. Carusotto, I. Sagnes, M. Abbarchi, D.D. Solnyshkov, G. Malpuech, E. Galopin, A. Lematre, J. Bloch, and A. Amo. Direct Observation of Dirac Cones and a Flatband in a Honeycomb Lattice for Polaritons. *Physical Review Letters*, 112(11):116402, March 2014.

[41] P. St-Jean, V. Goblot, E. Galopin, A. Lematre, T. Ozawa, L. Le Gratiet, I. Sagnes, J. Bloch, and A. Amo. Lasing in topological edge states of a one-dimensional lattice. *Nature Photonics*, 11(10):651–656, October 2017.

[42] S. Klembt, T. H. Harder, O. A. Egorov, K. Winkler, R. Ge, M. A. Bandres, M. Emmerling, L. Worschech, T. C. H. Liew, M. Segev, C. Schneider, and S. Hfling. Exciton-polariton topological insulator. *Nature*, 562(7728):552, October 2018.

[43] Natalia G. Berloff, Matteo Silva, Kirill Kalinin, Alexis Askitopoulos, Julian D. Tpfer, Pasquale Cilibrizzi, Wolfgang Langbein, and Pavlos G. Lagoudakis. Realizing the classical XY Hamiltonian in polariton simulators. *Nature Materials*, 16(11):1120–1126, November 2017.

[44] G. Tosi, G. Christmann, N. G. Berloff, P. Tsotsis, T. Gao, Z. Hatzopoulos, P. G. Savvidis, and J. J. Baumberg. Sculpting oscillators with light within a nonlinear quantum fluid. *Nature Physics*, 8(3):190–194, March 2012.

[45] P. Cristofolini, A. Dreismann, G. Christmann, G. Franchetti, N. G. Berloff, P. Tsotsis, Z. Hatzopoulos, P. G. Savvidis, and J. J. Baumberg. Optical Superfluid Phase Transitions and Trapping of Polariton Condensates. *Physical Review Letters*, 110(18):186403, May 2013.

[46] H. Ohadi, R.L. Gregory, T. Freegarde, Y.G. Rubo, A.V. Kavokin, N.G. Berloff, and P.G. Lagoudakis. Nontrivial Phase Coupling in Polariton Multiplets. *Physical Review X*, 6(3), August 2016.

[47] Marta Galbiati, Lydie Ferrier, Dmitry D. Solnyshkov, Dimitrii Tanese, Esther Wertz, Alberto Amo, Marco Abbarchi, Pascale Senellart, Isabelle Sagnes, Aristide Lematre, Elisabeth Galopin, Guillaume Malpuech, and Jacqueline Bloch. Polariton Condensation in Photonic Molecules. *Physical Review Letters*, 108(12):126403, March 2012.

[48] Michael C. Y. Huang, Y. Zhou, and Connie J. Chang-Hasnain. A surface-emitting laser incorporating a high-index-contrast subwavelength grating. *Nature Photonics*, 1(2):119–122, February 2007.

[49] Michael C. Y. Huang, Ye Zhou, and Connie J. Chang-Hasnain. Single mode high-contrast subwavelength grating vertical cavity surface emitting lasers. *Applied Physics Letters*, 92(17):171108, April 2008.

[50] Connie J. Chang-Hasnain and Weijian Yang. High-contrast gratings for integrated optoelectronics. *Advances in Optics and Photonics*, 4(3):379, September 2012.

[51] Bo Zhang, Zhaorong Wang, Sebastian Brodbeck, Christian Schneider, Martin Kamp, Sven Hfling, and Hui Deng. Zero-dimensional polariton laser in a subwavelength grating-based vertical microcavity. *Light: Science & Applications*, 3(1):e135, January 2014.

[52] Zhaorong Wang, Bo Zhang, and Hui Deng. Dispersion Engineering for Vertical Microcavities Using Subwavelength Gratings. *Physical Review Letters*, 114(7):073601, February 2015.

[53] Michael C. Y. Huang, Ye Zhou, and Connie J. Chang-Hasnain. A nanoelectromechanical tunable laser. *Nature Photonics*, 2(3):180–184, March 2008.

[54] Weijian Yang, Stephen Adair Gerke, Kar Wei Ng, Yi Rao, Christopher Chase, and Connie J. Chang-Hasnain. Laser optomechanics. *Scientific Reports*, 5:13700, September 2015.

[55] Bo Zhang, Sebastian Brodbeck, Zhaorong Wang, Martin Kamp, Christian Schneider, Sven Hfling, and Hui Deng. Coupling polariton quantum boxes in sub-wavelength grating microcavities. *Applied Physics Letters*, 106(5):051104, February 2015.

[56] Albert F. Adiyatullin, Mitchell D. Anderson, Hugo Flayac, Marcia T. Portella-Oberli, Fauzia Jabeen, Claudric Ouellet-Plamondon, Gregory C. Sallen, and Benoit Deveaud. Periodic squeezing in a polariton Josephson junction. *Nature Communications*, 8(1):1329, November 2017.

[57] K. Rayanov, B.L. Altshuler, Y.G. Rubo, and S. Flach. Frequency Combs with Weakly Lasing Exciton-Polariton Condensates. *Physical Review Letters*, 114(19):193901, May 2015.

[58] K. G. Lagoudakis, F. Manni, B. Pietka, M. Wouters, T. C. H. Liew, V. Savona, A. V. Kavokin, R. Andr, and B. Deveaud-Pldran. Probing the Dynamics of Spontaneous Quantum Vortices in Polariton Superfluids. *Physical Review Letters*, 106(11):115301, March 2011.

[59] C. F R Mateus, M.C.Y. Huang, Yunfei Deng, Andrew R. Neureuther, and C.J. Chang-Hasnain. Ultrabroadband mirror using low-index cladded subwavelength grating. *IEEE Photonics Technology Letters*, 16(2):518–520, 2004.

[60] Robert Magnusson. Wideband reflectors with zero-contrast gratings. *Optics Letters*, 39(15):4337, August 2014.

[61] Vitor R. Manfrinato, Jianguo Wen, Lihua Zhang, Yujia Yang, Richard G. Hobbs, Bowen Baker, Dong Su, Dmitri Zakharov, Nestor J. Zaluzec, Dean J. Miller, Eric A. Stach, and Karl K. Berggren. Determining the Resolution Limits of Electron-Beam Lithography: Direct Measurement of the Point-Spread Function. *Nano Letters*, 14(8):4406–4412, August 2014.

[62] H. Suchomel, S. Klembt, T. H. Harder, M. Klaas, O. A. Egorov, K. Winkler, M. Emmerling, S. Hoefling, and C. Schneider. An electrically pumped polaritonic lattice simulator. *arXiv:1803.08306 [physics]*, March 2018. arXiv: 1803.08306.

[63] D. Read, T. C. H. Liew, Yuri G. Rubo, and A. V. Kavokin. Stochastic polarization formation in exciton-polariton Bose-Einstein condensates. *Physical Review B*, 80(19):195309, November 2009.

[64] Tomasz Czyszanowski, Marcin Gebski, Maciej Dems, Micha Wasiak, Robert Sarzaa, and Krassimir Panajotov. Subwavelength grating as both emission mirror and electrical contact for VCSELs in any material system. *Scientific Reports*, 7:srep40348, January 2017.

[65] A.V. Nalitov, T.C.H. Liew, A.V. Kavokin, B.L. Altshuler, and Y.G. Rubo. Spontaneous Polariton Currents in Periodic Lateral Chains. *Physical Review Letters*, 119(6), August 2017.

[66] T. C. Damen, Jagdeep Shah, D. Y. Oberli, D. S. Chemla, J. E. Cunningham, and J. M. Kuo. Dynamics of exciton formation and relaxation in GaAs quantum wells. *Physical Review B*, 42(12):7434–7438, October 1990.

[67] Mark Steger, Brian Fluegel, Kirstin Alberi, David W. Snoke, Loren N. Pfeiffer, Ken West, and Angelo Mascarenhas. Ultra-low threshold polariton condensation. *Optics Letters*, 42(6):1165–1168, March 2017.

[68] Vadim Karagodsky, Bala Pesala, Christopher Chase, Werner Hofmann, Fumio Koyama, and Connie J. Chang-Hasnain. Monolithically integrated multiwavelength VCSEL arrays using high-contrast gratings. *Optics Express*, 18(2):694–699, January 2010.

[69] A. P. D. Love, D. N. Krizhanovskii, D. M. Whittaker, R. Bouchekioua, D. Sanvitto, S. Al Rizeiqi, R. Bradley, M. S. Skolnick, P. R. Eastham, R. Andr, and Le Si Dang. Intrinsic Decoherence Mechanisms in the Microcavity Polariton Condensate. *Physical Review Letters*, 101(6):067404, August 2008.

[70] Fabrice P. Laussy, G. Malpuech, A. Kavokin, and P. Bigenwald. Spontaneous Coherence Buildup in a Polariton Laser. *Physical Review Letters*, 93(1):016402, June 2004.

[71] Paolo Schwendimann, Antonio Quattropani, and Davide Sarchi. Stationary and time-dependent correlations in polariton condensates. *Physical Review B*, 82(20):205329, November 2010.

[72] H. Haug, T. D. Doan, H. Thien Cao, and D. B. Tran Thoai. Temporal first- and second-order correlations in a polariton condensate. *Physical Review B*, 85(20):205310, May 2012.

[73] D. M. Whittaker and P. R. Eastham. Coherence properties of the microcavity polariton condensate. *EPL (Europhysics Letters)*, 87(2):27002, July 2009.

[74] Roy J. Glauber. The Quantum Theory of Optical Coherence. *Physical Review*, 130(6):2529–2539, June 1963.

[75] Marlan O. Scully. *Quantum Optics*. Cambridge University Press, September 1997.

[76] Rodney Loudon. *The Quantum Theory of Light*. Oxford University Press, September 2000.

[77] H. M. Wiseman. Defining the (atom) laser. *Physical Review A*, 56(3):2068–2084, September 1997.

[78] L. K. Thomsen and H. M. Wiseman. Atom-laser coherence and its control via feedback. *Physical Review A*, 65(6):063607, June 2002.

[79] J. Kasprzak, M. Richard, A. Baas, B. Deveaud, R. Andr, J.-Ph. Poizat, and Le Dang. Second-Order Time Correlations within a Polariton Bose-Einstein Condensate in a CdTe Microcavity. *Physical Review Letters*, 100(6):067402, February 2008.

[80] Jean-Sebastian Tempel, Franziska Veit, Marc Amann, Lars E. Kreilkamp, Arash Rahimi-Iman, Andreas Lffler, Sven Hfling, Stephan Reitzenstein, Lukas Worschech, Alfred Forchel, and Manfred Bayer. Characterization of two-threshold behavior of the emission from a GaAs microcavity. *Physical Review B*, 85(7):075318, February 2012.

[81] Alexey Kavokin, Jeremy J. Baumberg, Guillaume Malpuech, and Fabrice P. Laussy. *Microcavities*. Oxford University Press, December 2007.

[82] R. Houdr, J. L. Gibernon, P. Pellandini, R. P. Stanley, U. Oesterle, C. Weisbuch, J. OGorman, B. Roycroft, and M. Ilegems. Saturation of the strong-coupling regime in a semiconductor microcavity: Free-carrier bleaching of cavity polaritons. *Physical Review B*, 52(11):7810–7813, September 1995.

[83] H. Haug, H. Thien Cao, and D. B. Tran Thoai. Coherence and decoherence of a polariton condensate. *Physical Review B*, 81(24):245309, June 2010.

[84] Kenichiro Kusudo, Na Young Kim, Andreas Lffler, Sven Hfling, Alfred Forchel, and Yoshihisa Yamamoto. Stochastic formation of polariton condensates in two degenerate orbital states. *Physical Review B*, 87(21):214503, June 2013.

[85] M. Klaas, H. Flayac, M. Amthor, I.G. Savenko, S. Brodbeck, T. Ala-Nissila, S. Klembt, C. Schneider, and S. Hfling. Evolution of Temporal Coherence in Confined Exciton-Polariton Condensates. *Physical Review Letters*, 120(1), January 2018.

[86] Saeed Khan and Hakan E. Treci. Frequency Combs in a Lumped-Element Josephson-Junction Circuit. *Physical Review Letters*, 120(15), April 2018.

[87] H. Ohadi, A. Dreismann, Y.G. Rubo, F. Pinsker, Y. del Valle-Inclan Redondo, S.I. Tsintzos, Z. Hatzopoulos, P.G. Savvidis, and J.J. Baumberg. Spontaneous Spin Bifurcations and Ferromagnetic Phase Transitions in a Spinor Exciton-Polariton Condensate. *Physical Review X*, 5(3):031002, July 2015.

[88] I. L. Aleiner, B. L. Altshuler, and Y. G. Rubo. Radiative coupling and weak lasing of exciton-polariton condensates. *Physical Review B*, 85(12):121301, March 2012.

[89] F. Manni, K. G. Lagoudakis, T. C. H. Liew, R. Andr, and B. Deveaud-Pldran. Spontaneous Pattern Formation in a Polariton Condensate. *Physical Review Letters*, 107(10):106401, September 2011.

[90] O. Arcizet, P.-F. Cohadon, T. Briant, M. Pinard, and A. Heidmann. Radiation-pressure cooling and optomechanical instability of a micromirror. *Nature*, 444(7115):71–74, November 2006.

[91] T. P. Purdy, P.-L. Yu, R. W. Peterson, N. S. Kampel, and C. A. Regal. Strong Optomechanical Squeezing of Light. *Physical Review X*, 3(3):031012, September 2013.

[92] Matt Eichenfield, Jasper Chan, Ryan M. Camacho, Kerry J. Vahala, and Oskar Painter. Optomechanical crystals. *Nature*, 462(7269):78–82, November 2009.

[93] O. Kyriienko, T.C.H. Liew, and I.A. Shelykh. Optomechanics with Cavity Polaritons: Dissipative Coupling and Unconventional Bistability. *Physical Review Letters*, 112(7):076402, February 2014.

[94] Eleonora Nagali, Fabio Sciarrino, Francesco De Martini, Lorenzo Marrucci, Bruno Piccirillo, Ebrahim Karimi, and Enrico Santamato. Quantum Information Transfer from Spin to Orbital Angular Momentum of Photons. *Physical Review Letters*, 103(1):013601, June 2009.

[95] Graham Gibson, Johannes Courtial, Miles J. Padgett, Mikhail Vasnetsov, Valeriy Pasko, Stephen M. Barnett, and Sonja Franke-Arnold. Free-space information transfer using light beams carrying orbital angular momentum. *Optics Express*, 12(22):5448–5456, November 2004.

[96] K. G. Lagoudakis, T. Ostatnick, A. V. Kavokin, Y. G. Rubo, R. Andr, and B. Deveaud-Pldran. Observation of Half-Quantum Vortices in an Exciton-Polariton Condensate. *Science*, 326(5955):974–976, November 2009.

[97] Robert Dall, Michael D. Fraser, Anton S. Desyatnikov, Guangyao Li, Sebastian Brodbeck, Martin Kamp, Christian Schneider, Sven Hfling, and Elena A. Ostrovskaya. Creation of Orbital Angular Momentum States with Chiral Polaritonic Lenses. *Physical Review Letters*, 113(20):200404, November 2014.

[98] T. Boulier, E. Cancellieri, N.D. Sangouard, Q. Glorieux, A.V. Kavokin, D.M. Whittaker, E. Giacobino, and A. Bramati. Injection of Orbital Angular Momentum and Storage of Quantized Vortices in Polariton Superfluids. *Physical Review Letters*, 116(11):116402, March 2016.

[99] Lorenzo Dominici, Ricardo Carretero-Gonzlez, Antonio Gianfrate, Jess Cuevas-Maraver, Augusto S. Rodrigues, Dimitri J. Frantzeskakis, Giovanni Lerario, Dario Ballarini, Milena De Giorgi, Giuseppe Gigli, Panayotis G. Kevrekidis, and Daniele Sanvitto. Interactions and scattering of quantum vortices in a polariton fluid. *Nature Communications*, 9(1):1467, April 2018.

[100] Nicola Carlon Zambon, Philippe St-Jean, Marijana Milievi, Aristide Lematre, Abdelmounaim Harouri, Luc LeGratiet, Olivier Bleu, Dmitry Solnyshkov, Guillaume Malpuech, Isabelle Sagnes, Sylvain Ravets, Alberto Amo, and Jacqueline Bloch. Optically controlling the emission chirality of microlasers. *arXiv:1806.04590 [cond-mat, physics:physics]*, June 2018. arXiv: 1806.04590.

[101] Qiwen Zhan. Cylindrical vector beams: from mathematical concepts to applications. *Advances in Optics and Photonics*, 1(1):1–57, January 2009.

[102] R. Dorn, S. Quabis, and G. Leuchs. Sharper Focus for a Radially Polarized Light Beam. *Physical Review Letters*, 91(23):233901, December 2003.

[103] Pei Miao, Zhifeng Zhang, Jingbo Sun, Wiktor Walasik, Stefano Longhi, Natalia M. Litchinitser, and Liang Feng. Orbital angular momentum microlaser. *Science*, 353(6298):464–467, July 2016.